Mesospheric Clouds on Earth and Mars

Thomas Peter Mangan

Submitted in accordance with the requirements for the degree of Doctor of Philosophy

The University of Leeds
School of Chemistry

March 2017

The candidate confirms that the work submitted is his own, except where work which has formed part of jointly-authored publications has been included. The contribution of the candidate and the other authors to this work has been explicitly indicated below. The candidate confirms that appropriate credit has been given within the thesis where reference has been made to the work of others.

Please see the contributions section for full details of the contributions of the candidate and other authors.

Acknowledgements

Firstly I would like to thank my primary supervisor Prof John Plane, for giving me the opportunity to undertake a PhD in such an interesting and exciting field. The research environment created within the Plane group has been excellent and encompasses a wide understanding of different backgrounds which has always been useful during my study. I would also like to thank my second supervisor Prof Ben Murray, firstly for supervising my undergraduate project that got me interested in doing ice based experimental research. Ben and the Murray group have provided an alternate outlook on research ideas, which has been greatly beneficial for my PhD as a whole. I'd also like to thank NERC for funding the project and enabling me to talk about my research around the world.

Thanks are extended to all researchers who I have worked with and helped me at Leeds during my PhD: Vicki, Sandy, Tasha, Shane, Anna, JC, JD, Wuhu, James, Erin, David, Theo, Danny, Jim, Hannah, Mark, Mark, Tom, Fred and anyone else I have forgotten at this moment. Thanks also to Denis and Mario at KIT for their hospitality and knowledge and thanks to Christoph at UCL for his insights and interest in CO_2 crystals. I'd also like to thank Lesley, Tamsin and Matt for their technical support and any tech guys at companies who I have badgered about broken equipment.

I am grateful to Vicki for providing initial support in understanding the UHV system and in particular Sandy, for being a fellow PhD student throughout the whole process. I'd also like to thank Julie for being the world's most

supportive and understanding postgraduate tutor during the first two years of my PhD.

Special thanks go out to the lovely Charlotte, for keeping me sane and always being there to share a laugh after work. My Mum and Dad also deserve multiple thanks and only with their support throughout my life has reaching this stage been possible.

Contributions

My own contributions and those of other researchers, fully and explicitly indicated in the thesis and associated publications, have been:

In developing experimental methods (Chapter 2):

- Modification and maintenance of the UHV system for use in experiments in Chapter 3 and 4 (assisted initially by Dr Victoria Frankland).
- Modifications of the XRD system for CO_2 deposition, specifically construction of a new gas flow system.
- Design and installation of the UHV RAIRS system (purge boxes constructed by Matthew Broadbent).
- Undertaking of RAIRS experiments detailed for Benzene.
- The TRAPS system was developed and used primarily by Dr Denis Duft and Mario Nachbar at the Karlsruhe institute of technology (KIT).

In an investigation of CO_2 trapping in ice (chapter 3) and associated publication:

"*Thomas Mangan, Victoria Frankland & John Plane, (2015), CO2 trapping in amorphous H_2O ice: Relevance to polar mesospheric cloud particles. Journal of Atmospheric and Solar-Terrestrial Physics. 127, 92-96."*

- I performed all laboratory experiments for beam flux calibrations and for CO_2 trapping. I carried out data analysis and interpreted the data. I was initially assisted in experiments by Dr Victoria Frankland.

In the study of metal uptake on ice (chapter 4):

- I carried out all experiments and data analysis.
- Electronic structure calculations of Fe, Mg and K bound to an ice surface were carried out by Prof John Plane.

In the study of CO_2 ice nucleation on nanoparticles (chapter 5) and associated publication:

"Mario Nachbar, Denis Duft, Thomas Mangan, Juan Carlos Gomez Martin, John Plane, and Thomas Leisner (2016), Laboratory measurements of heterogeneous CO2 ice nucleation on nanoparticles under conditions relevant to the Martian mesosphere, Journal of Geophysical Research Planets, 121, 753–769."

- I assisted with initial experiments at the Karlsruhe Institute of Technology (KIT) on SiO_2 nanoparticles (Fe_xO_y experiments were carried out by Dr Denis Duft and Mario Nachbar) and provided information and interpretation regarding implications for CO_2 ice clouds on Mars and assistance with analysis.
- Raw data analysis was led by Dr Denis Duft and Mario Nachbar.

In the study of CO_2 crystal properties (Chapter 6) and associated publication:

"Thomas Mangan, Christoph Salzmann, John Plane & Ben Murray (2017), CO2 ice structure and density under Martian atmospheric conditions. Icarus. – In press."

- I performed all laboratory experiments, all data analysis and all calculations regarding atmospheric implications.

- Modelling of CO_2 crystal shape was initially undertaken by Dr Christoph Salzmann and then reproduced by me using Mercury 3.9 software.

Throughout the studies detailed here I was supervised, managed and directed by Profs John Plane and Ben Murray.

Abstract

This thesis comprises experimental investigations regarding the microphysical processes occurring within mesospheric clouds on Earth and Mars.

CO_2 trapping in amorphous ice was investigated with relevance to Earth's mesosphere as a possible temporary sink of gas phase CO_2. Experimental limits to the trapping process were evaluated and extrapolated to mesospheric conditions. This process was shown to be only plausible under extreme conditions. Metal deposition on low temperature ice was also investigated with relevance to PMCs. The reactivity of Mg and K was evaluated experimentally and with electronic structure calculations. A secondary Meteoric smoke Particle (MSP) formation process was hypothesised, with calculations suggesting this will impact the distribution of MSPs in the mesosphere during cloud season.

In regards to the Martian mesosphere, microphysical processes that influence CO_2 cloud formation have been investigated using a novel experimental system. Mass distributions of CO_2 nucleation on nanoparticles were used to determine variables critical to modelling CO_2 cloud formation. It is predicted here that lower temperatures than previously thought would be required to form CO_2 clouds in the mesosphere. The crystal structure of CO_2 ice under Martian conditions has also been experimentally investigated, with a cubic crystal structure determined (CO_2-I). Temperature dependent parameters of CO_2-I were applied to rates of nucleation and sedimentation for CO_2 ice particles.

Table of Contents

List of Tables

List of Figures

List of Abbreviations

ASW	Amorphous Solid Water
CABMOD	Chemical ABlation MODel
CNT	Classical Nucleation Theory
CSW	Crystalline Solid Water
FTIR	Fourier transform infrared spectroscopy
INP	Ice Nucleating Particle
ISM	InterStellar Medium
KIT	Karlsruhe Institute of Technology
MDP	Martian Dust Particle
MICE	Molecular Ice flow CEll
MSP	Meteoric Smoke Particle
NAT	Nucleation Activation Temperature
NLC	NoctiLucent Cloud
NPS	NanoParticle Source
PMC	Polar Mesospheric Cloud
PMSE	Polar mesospheric summer echoes
QMS	Quadrupole Mass Spectrometer
RAIRS	Reflectance Absorbance Infra-Red Spectroscopy
SCIAMACHY	Scanning Imaging Absorption Spectrometer for Atmospheric CHartographY
SOFIE	Solar Occultation For Ice Experiment
TOF-MS	Time-Of-Flight Mass Spectrometer
TPD	Temperature Programmed Desorption
TRAPS	Trapped Reactive Atmospheric Particle Spectrometer
UHV	Ultra-High Vacuum
XRD	X-ray Diffraction

1 Introduction to Mesospheric clouds on Earth and Mars

This chapter provides the current understanding in the literature regarding mesospheric clouds on Earth (section 1.1) and mesospheric CO_2 clouds on Mars (section 1.2). Scientific questions relating to the microphysical gas-phase and surface processes of ice particles occurring in these clouds are posed by highlighting gaps in the literature. These questions are summarised as research questions and project aims in section 1.4.

1.1 The Earth's mesosphere

The mesosphere of Earth lies between the stratosphere and the thermosphere covering an altitude range of approximately 50 – 100 km. The temperature of the mesosphere decreases with increasing altitude due primarily to reduced solar heating of the rarefied atmosphere and increased cooling by CO_2 emission. The mesopause is where the coldest temperatures on Earth are observed (as low as 90 K under extreme conditions) [*Lübken et al.*, 2009]. Extra-terrestrial input of meteoric material to this region of the atmosphere from above, and vertical mixing from below means the mesosphere, although rarefied, is home to a series of complex gas and surface chemistry processes (discussed in subsection 1.1.1). The mesosphere is also home to the highest altitude clouds on Earth, Polar Mesospheric Clouds (PMCs), which are the focus of this introduction section.

1.1.1 Metal layers

Meteoric material enters the upper atmosphere (total input of material 43 ± 14 t d^{-1}) at high speeds (12 – 70 km s^{-1}), leading to ablation of a fraction of the material due to frictional heating [*Carrillo-Sánchez et al.*, 2016]. The injection rates for a variety of metals, predicted by the Chemical ABlation MODel (CABMOD) [*Vondrak et al.*, 2008], for a 5 µg meteoroid entering the atmosphere at 20 km s^{-1}, are shown in the top panel of Figure 1.1. After release of the metals at altitudes relative to the characteristic temperature profile at which they ablate in relation to the velocity of the particle, the metals undergo ion and neutral chemistry, producing layers of metal atoms in the upper mesosphere. Subsequent gas-phase reactions of these metals leads to the formation of stable reservoirs (e.g. metal oxides and silicates), which polymerize into Meteoric Smoke Particles (MSPs) [*Plane*, 2003; *Saunders and Plane*, 2006]. Using Fe as an example, the most likely MSP constituents are: goethite (α-FeOOH); hematite (Fe_2O_3); pyroxene ($FeSiO_3$); and fayalite (Fe_2SiO_4) [*Plane*, 2012]. This loss of metals to form MSPs is replenished by constant ablation of fresh meteoric input (e.g. Fe has an injection rate of approximately 0.01 atom cm^{-3} s^{-1} at 80 km) [*Carrillo-Sánchez et al.*, 2016]. MSPs are a significant source of refractory nanoparticles (<15 nm radius) in the mesosphere of Earth [*Plane*, 2012], illustrated by a predicted MSP distribution shown in the bottom panel of Figure 1.1 [*Plane et al.*, 2014]. These MSPs are the likely source of ice nucleating particles (INPs) for PMCs, discussed in more detail in subsection 1.1.3 [*Hervig et al.*, 2012]. Metals can also be taken up on the surface of mesospheric ice particles due to the overlap in the altitude range of the metal layers with PMCs; this is discussed in detail in subsection 1.1.6 [*Plane et al.*, 2004].

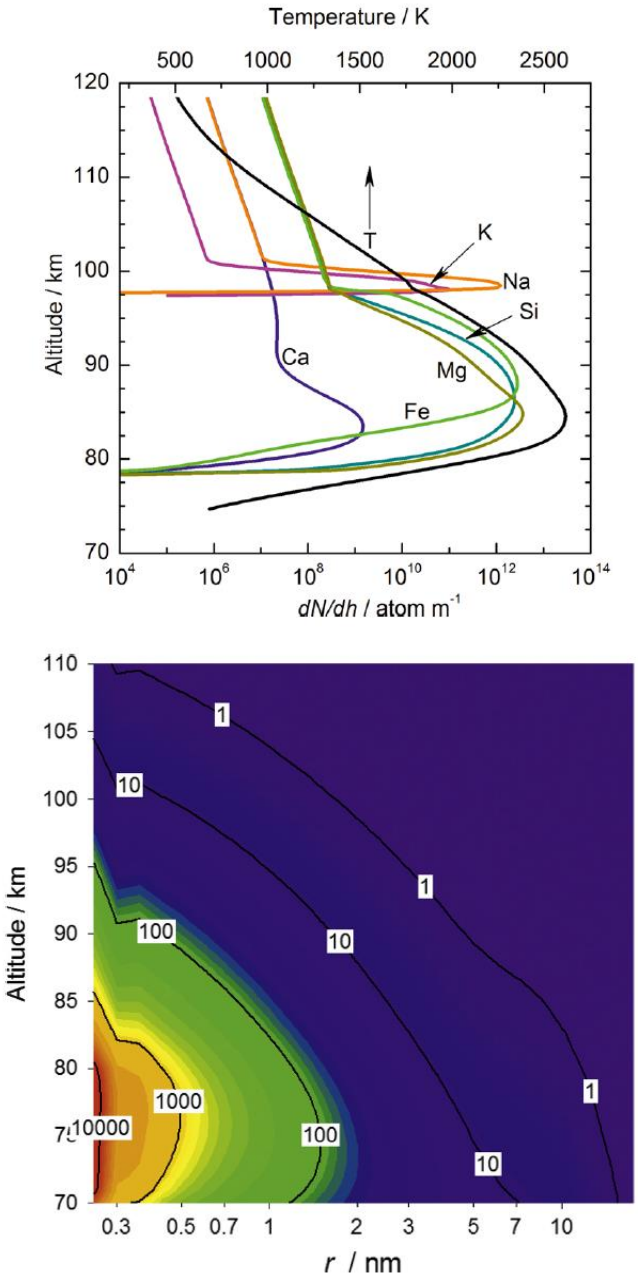

Figure 1.1: In the top panel an example of a modelled ablation profile for a 5 µg meteoroid is shown. Taken from [*Vondrak et al.*, 2008]. In the bottom panel an MSP size distribution for the mesosphere is shown, calculated using a 1-D microphysics model for an ablated meteoric input of 5 t d^{-1}. Adapted from *Plane et al.* [2014].

1.1.2 PMCs

PMCs (also known as noctilucent clouds (NLCs)) are in terms of cloud types on Earth, a relatively newly observed phenomenon, with the first observations made two years after the 1883 eruption of Krakatoa [*Gadsden and Schroder*, 1989]. For a review on the early research into PMCs, *Thomas* [1991] provides a comprehensive summary of pre-1991 investigations. These early studies lacked a lot of the quantitative capabilities of modern studies, with recent developments in satellite technology, radar and lidar leading to a greater understanding of the microphysical properties of PMCs that are discussed within section 1.1. PMCs have also been tentatively linked to climate variability, suggested as a sensitive indicator of climate change in the mesosphere due to changing temperature and water vapour [*Thomas and Olivero*, 2001]. Recent analysis of data from 1979 – 2013 highlighted long term trends, with cooling of 0.58 ± 0.32 K decade^{-1} at an altitude of 83 km [*Berger and Lübken*, 2015].

1.1.3 Microphysics of PMCs

PMCs typically form in the polar summer mesopause region, at temperatures below 145 K [*Rapp and Thomas*, 2006]. Weaker PMCs have also been observed at mid-latitudes [*Hervig et al.*, 2016b]. The temperatures in the 80 – 90 km region for PMC formation are typically 125 - 145 K but can reach temperatures as low as approximately 90 K [*Lübken et al.*, 2009]. Negative temperature perturbations caused by the propagation of gravity waves from the lower atmosphere can lead to favourable supersaturation conditions for PMC formation and are observed in the cloud morphology as wave structures [*Chandran et al.*, 2012; *Yue et al.*, 2014].

Wegener [1912] first suspected that mesospheric clouds, like other terrestrial clouds, were formed mainly of water ice. This was reinforced by observations of water ice supersaturations and temperature associated with PMCs. Using data from the HALogen Occultation Experiment (HALOE) instrument on the Upper Atmosphere Research Satellite (UARS), water ice was confirmed as the primary component of PMCs by *Hervig et al.* [2001]. Observed IR spectra of PMCs showed good agreement with model simulations of ice particle extinction.

Homogeneous nucleation, heterogeneous nucleation and ion-induced nucleation of water ice are the pathways for PMC formation in the mesosphere, with nucleation occurring in the deposition mode (condensed from the vapour phase) because of the low temperatures and pressures in this region of the atmosphere. It has been hypothesised that below 125 K ion-induced nucleation could produce populations of small ice particles in the mesosphere [*Arnold*, 1980; *Gumbel et al.*, 2003]. Similarly, homogeneous nucleation requires low temperatures to occur and, until recently, was thought to be of negligible importance in the mesosphere [*Gadsden and Schroder*, 1989]. However, it has been shown through a 1D model that, under certain mesospheric conditions (≤ 110 K and a H_2O mixing ratio of 1 ppmv), 10^4 - 10^5 cloud particles cm^{-3} can be produced homogeneously. This is most likely to occur during fast cooling rates (>0.5 K min^{-1}) where super-saturations can reach a homogeneous threshold before H_2O vapour is depleted by heterogeneous crystal growth [*Lübken et al.*, 2009; *Murray and Jensen*, 2010].

Heterogeneous ice nucleation is thought to be the most prominent pathway to nucleation of ice particles in the mesosphere, where a reduction in the energy barrier to nucleation is achieved in the presence of suitable ice INPs. This enables nucleation at more typically observed mesospheric conditions compared to ion-induced or homogeneous nucleation. [*Rapp and Thomas*, 2006].

MSPs are thought to be the major INP source in the mesosphere of Earth with their composition and formation discussed in subsection 1.1.1. Observational evidence of MSP inclusion in PMC ice was achieved using measurements from the Solar Occultation For Ice Experiment (SOFIE) spectrometer on the the Aeronomy of Ice in the Mesosphere (AIM) satellite, suggesting that 0.01 – 3% by volume of PMC ice particles were MSPs [*Hervig et al.*, 2012]. Observations of ice particle size by the Cloud Imaging and Particle Size (CIPS) instrument on AIM were reconciled with SOFIE data when a 0.5% volume inclusion of MSPs was assumed [*Bailey et al.*, 2015], in agreement with *in situ* rocket-borne dust probe measurements of ice fragments [*Havnes et al.*, 2014].

The phase of H_2O-ice in the mesosphere has been an area of some debate, as until recently it was assumed to form Crystalline Solid Water (CSW), regardless of the fact that Amorphous Solid Water (ASW) is known to exist under mesospheric conditions [*Rapp and Thomas*, 2006]. Experimentally it has been shown that at temperatures below 130 K ASW can form, predicted in the mesosphere to convert to CSW on a timescale of hours [*Kohl et al.*, 2005; *Murray and Jensen*, 2010]. Using observations from SOFIE and modelled extinctions for ASW, *Hervig and Gordley* [2010] concluded that

crystalline cubic ice was the primary phase in PMCs but could not rule out undetected ASW. This understanding is important due to the lower interfacial energy of ASW compared to the crystalline forms (cubic and hexagonal), which in turn leads to a lower energy barrier to nucleation.

With heterogeneous nucleation being the dominant process of ice formation, there is a great deal of interest in the types of ice-nucleating particle that are present in the mesosphere and how they interact with H_2O vapour. Investigations into mesospheric particles have been undertaken with a focus on their impact on ice formation. Comparisons of model studies of PMCs to lidar observations have shown that both an understanding of the mesospheric circulation processes and the nucleating efficiency of the INP is crucial for reproducing observed PMCs [*Asmus et al.*, 2014; *Wilms et al.*, 2016].

The ice-nucleation capabilities of MSP analogues have been investigated experimentally with relevance to the upper troposphere and stratosphere using the AIDA chamber [*Saunders et al.*, 2010]. Fe_2O_3, MgO and SiO_2 were found to be reasonably efficient INP when evaluated with Classical Nucleation Theory (CNT) above 180 K. These temperatures are still too high to apply to the mesosphere but under mesospheric conditions it is speculated that further reductions in efficiency would be observed. This is in line with measurements of H_2O nucleation on a silicon wafer at ≥ 150 K [*Trainer et al.*, 2009]. Currently the contact parameter and saturation ratios for heterogeneous nucleation on suitable INPs such as MSP analogues studied under mesospheric conditions are not yet known, but are currently under investigation [*Nachbar et al.*, 2016a].

1.1.4 Vertical structure of PMCs

Figure 1.2 provides a summary of the processes that are involved in the formation of a PMC. *Via* the nucleation pathways discussed in section 1.1.3, ice number density increases in the presence of sufficiently high H_2O vapour concentrations, ice nucleating particles and temperatures sufficiently below the H_2O frost point. Ice particles are present at altitudes of 82 – 88 km but the vertical structure of the layer varies [*Hervig et al.*, 2011]. The ice number density reduces with decreasing height, some particles sublimating at the expense of others who grow and sediment. This produces a smaller population of ice particles with increased radii at the base of the cloud [*Rapp and Thomas*, 2006]. These mesospheric ice particles are present at extremely small radii compared to tropospheric cloud formations (e.g. mean PMC ice particle radii of 30 - 80 nm [*Robert et al.*, 2009; *von Savigny and Burrows*, 2007] while mean cirrus radii are > 1 mm [*Tian et al.*, 2010]), with the largest particles at the base of the cloud scattering light to a great enough extent to become optically visible [*von Cossart et al.*, 1999]. These large particles sublimate at the base of the cloud layer due to sedimentation into an unsaturated/warmer region of the mesosphere. This sublimation is observed as an enhancement in H_2O vapour [*Hervig et al.*, 2015].

Polar mesospheric summer echoes (PMSE) are scattering of radar waves observed in the very high frequency (VHF) range, and in the mesosphere are caused by the interaction of electrons with ice particles [*Rapp and Lübken*, 2004]. PMSE provide a way to observe sub-visible ice particles above the PMC layer, due to charging of the ice particles. These ice

particles become charged due to the fact they are immersed in the plasma of the D-region of the ionosphere, which leads to sharp gradients of electron number densities and therefore irregularities in the radio refractive index.

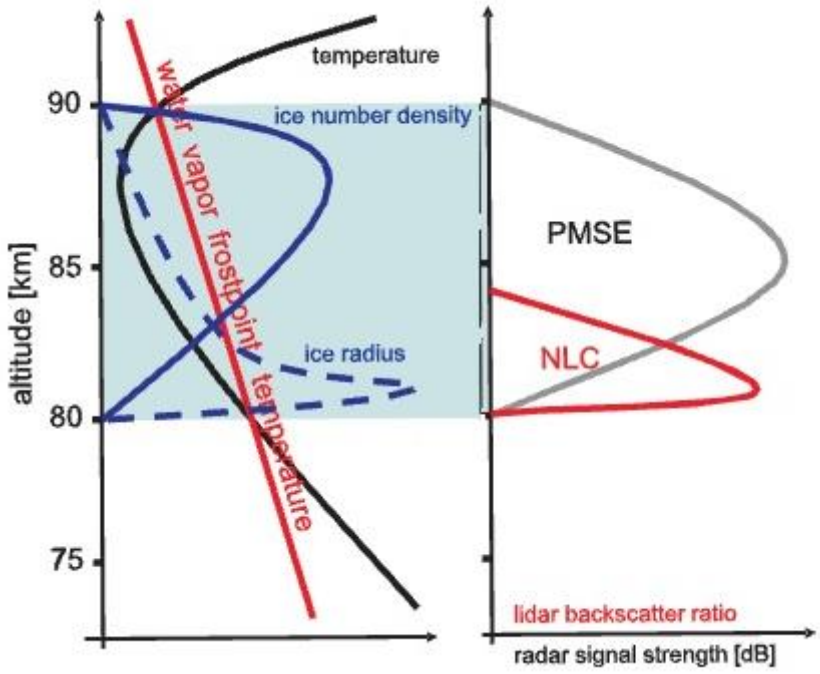

Figure 1.2: General summary of the evolution of ice particles within a mesospheric cloud (NLC/PMC) and the presence of PMSEs. Adapted from *Rapp and Thomas* [2006].

1.1.5 CO_2 and H_2O in the mesosphere

The relative composition of some gases in the mesosphere is markedly different compared to the lower atmosphere. This may have implications concerning the composition of mesospheric ice particles due to the ability of ice to trap and adsorb gases. Figure 1.3 shows data from satellite observations with model fits and clearly reveals that CO_2 is well mixed in the atmosphere up to approximately 80 km, above which ultraviolet (UV) photolysis of CO_2 to CO and diffusive separation become the dominant processes. This results in a rapid decline in CO_2 mixing ratios in the

thermosphere. Increases in anthropogenic carbon oxide (CO_x) emissions are leading to an increase in the overall upper atmospheric concentrations, with a global increase of ~20 ppm decade^{-1} at an altitude of 80 km [*Emmert et al.*, 2012; *Garcia et al.*, 2014]. At PMC altitudes the CO_2 concentration (using trends up to 2015) is above 360 ppm, which will continue to increase for the foreseeable future [*Yue et al.*, 2015].

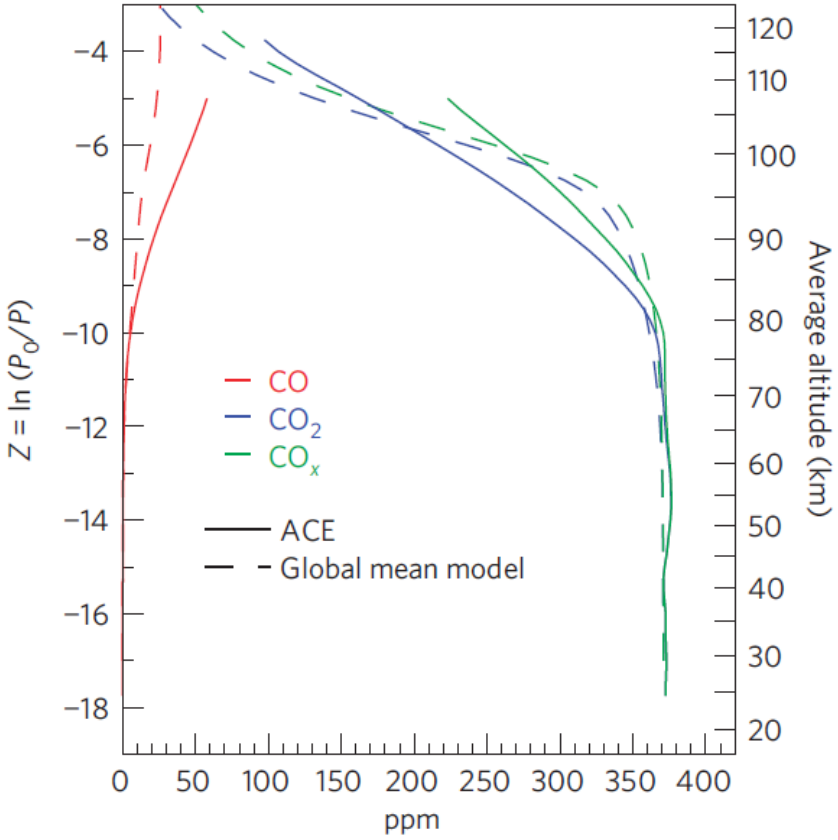

Figure 1.3: Average volume mixing ratios for CO, CO_2 and CO_x (2004 - 2012) in the Earth's mesosphere, from the Atmospheric Chemistry Experiment (ACE) and the National Centre for Atmospheric Research (NCAR) model. Reproduced from *Emmert et al.* [2012].

H_2O vapour is present in significantly lower concentrations than CO_2, even during the summer when concentrations are enhanced during the PMC season. Atmospheric upwelling and methane (CH_4) oxidation are thought to

be the main sources of mesospheric H_2O vapour [*Rong et al.*, 2012; *Thomas*, 1991]. Mesospheric H_2O concentrations in the northern hemisphere (77ºN) are increasing at a rate of 0.07 ± 0.03 ppm decade^{-1} [*Hervig et al.*, 2016a]. H_2O mixing ratios for the summers of 2007 and 2008 at mesospheric altitudes are shown in Figure 1.4 and are determined from Microwave Limb Sounder (MLS) retrievals [*Rong et al.*, 2010]. At PMC altitudes, H_2O mixing ratios can vary from 0 to 10 ppm at the height of the PMC cloud season. This leads to a large ratio of CO_2:H_2O in the mesosphere (>37:1) compared to the lower atmosphere (>0.01:1). This large ratio raises questions about the interactions of H_2O ice in PMCs and gas-phase CO_2 under these conditions.

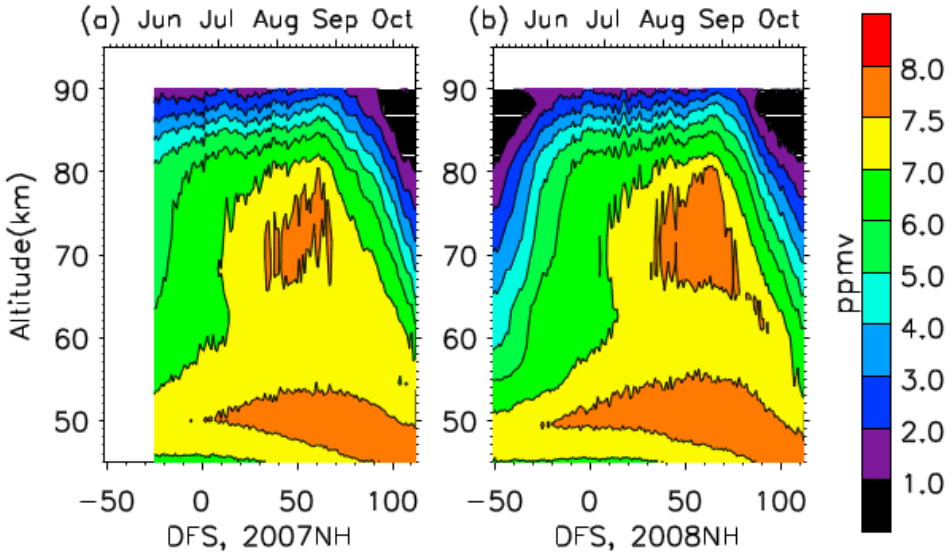

Figure 1.4: Profiles of altitude versus time for H_2O mixing ratios from the MLS on board the Aura satellite. The bottom abscissa indicates days from the summers solstice (DFS). Adapted from *Rong et al.* [2010].

It has been shown through the use of temperature-programmed desorption (TPD) experiments and Infra-red (IR) spectroscopy studies that CO_2 can be effectively trapped within ASW [*Galvez et al.*, 2008]. However, these experiments so far have not been undertaken at conditions relevant to the mesosphere of Earth. Ultra-high vacuum (UHV) studies using CO_2:H_2O mixed ices have often focused on the interstellar medium (ISM). Here the temperatures are often below atmospheric relevance (<90 K), and high H_2O:CO_2 ratios have been used as 60-70% of interstellar ice is H_2O [*Escribano et al.*, 2013; *Galvez et al.*, 2007; *Hodyss et al.*, 2008b]. More relevant studies at higher CO_2:H_2O ratios and pressures have focused on the Martian regolith which is a seasonal layer of ice that forms at the surface. This involved studies at higher temperatures of 140 – 200 K comparable to the Martian polar regions during winter (discussed in section 1.2) [*Bar-nun et al.*, 1985; *Mitterdorfer et al.*, 2011; *Trainer et al.*, 2010]. Often in these studies, although the ratio of gases is known the actual flux of molecules to the surface is not constrained. Formation of ASW has been proposed In the mesosphere and could persist for several hours before crystallisation to CSW occurs [*Murray and Jensen*, 2010]. Given the high ratios of CO_2:H_2O (> 37:1), increasing trends in concentrations and possible ASW formation, it may be possible to trap CO_2 in ice under mesospheric conditions. The ice particles would then act as a temporary sink for gas phase CO_2.

1.1.6 Metal uptake on PMCs

As well as being involved in the initial nucleation of ice particles in PMCs through formation of MSPs, it has been shown that metals from the layers discussed in sub section 1.1.1 can also be efficiently removed from the gas

phase by ice in the mesosphere. Lidar measurements at Spitzbergen (78ºN) of the K layer along with PMSE and PMC observations, showed a reduction in the underside of the layer in the presence of PMC [*Lübken and Höffner*, 2004; *Raizada et al.*, 2007]. Satellite observations have also highlighted the correlation between PMC occurrence, and depletion of the underside of the K layer at high latitudes [*Dawkins et al.*, 2015]. In the case of Fe, bite-outs have been observed in the underside of the metal Layer in the presence of PMCs [*Gardner et al.*, 2005; *Plane et al.*, 2004]. The depletion of the Fe layer by heterogeneous uptake on PMCs is shown in Figure 1.5. Based on measurements from the Scanning Imaging Absorption Spectrometer for Atmospheric CHartographY (SCIAMACHY) on board Envisat, an anti-correlation between Mg density and PMC radiance was observed at high latitudes, tentatively suggesting Mg may be depleted by PMCs [*Langowski et al.*, 2015].

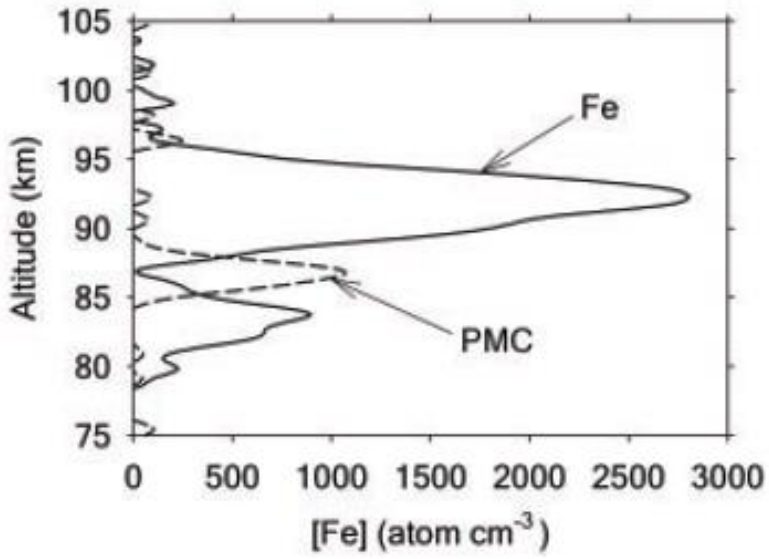

Figure 1.5: Simultaneous retrievals of atomic Fe density and PMC backscatter (expressed as equivalent Fe atoms cm^{-3}) showing a bite-out in the underside of the Fe layer in the presence of PMC. Adapted from *Plane et al.* [2004].

Experimentally, the uptake of metals on ice has been previously investigated with applications to PMCs, showing efficient uptake (uptake coefficient close to 1) for Na and K at 80 - 150 K and Fe at 135 – 150 K, explaining the observed metal depletion during PMC events [*Murray and Plane*, 2005]. A study by *Frankland and Plane* [2015] found that Fe was efficiently released from the ice into the gas phase by energetic ion sputtering by Ar^+, though did not co-desorb when the ice sublimated. Investigations into the photoelectric emission of K, Na and Li on ice have also been undertaken, with the decay in K signal thought to be due to KOH formation [*Vondrak et al.*, 2006; *Vondrak et al.*, 2009]. The uptake and reactivity of Mg on ice and experimental determination of the reactive products of K on ice have not been experimentally investigated previously. An understanding of these metal ice interactions is pertinent for understanding metal layer chemistry in the mesosphere and the formation of MSPs.

1.2 The Martian mesosphere

The Martian atmosphere has important differences when compared to that of the Earth, both dynamically and in its composition. These differences arise from influences during the evolution of the planets, and orbital, size and topographical differences. Mars atmosphere consists of 96% CO_2 with trace species including Ar, N_2, O_2 and CO, with H_2O vapour also being present at the surface (0.03%) [*Mahaffy et al.*, 2013; *Prinn and Fegley*, 1987].

The surface atmospheric density on Mars is significantly lower than Earth with average surface pressures varying from approximately 4 - 8 mbar [*Millour et al.*, 2008]. This pressure range is due to seasonal variations with a pressure minimum during winters caused by condensation of up to 20% of atmospheric CO_2 onto the polar caps forming a solid CO_2 regolith [*Hourdin et al.*, 1993; *Noguchi et al.*, 2014]. The mesosphere of Mars extends from approximately 50 to 100 km with pressures ranging from 10^{-2} to 10^{-4} mbar and temperatures as low as 80 K [*Forget et al.*, 2009]. Figure 1.6 shows temperature profiles recorded close to the Martian northern hemisphere summer solstice and represent a relatively warm profile compared to Martian winter [*Leovy*, 2001]. Temperature profiles on Mars are notably different to Earth, one significant difference being a less varied profile at higher altitudes with the absence of clear temperature maxima and minima. Mars does not have a stratosphere like Earth due to the absence of an O_3 layer. This means vertical transport to the mesosphere is a more prominent process in controlling local temperature conditions. Daily variations in temperature are extreme with the rarefied dry atmosphere meaning heat is radiated quickly from the surface at night. H_2O and CO_2 are atmospherically present as

vapour and as clouds (tropospheric and mesospheric) with sub-zero surface temperatures and pressures too low to accommodate significant liquid H_2O [*Smith*, 2002; *Vincendon et al.*, 2011]. Atmospheric H_2O and more specifically CO_2 ice in the form of clouds is discussed in greater detail in the following subsections.

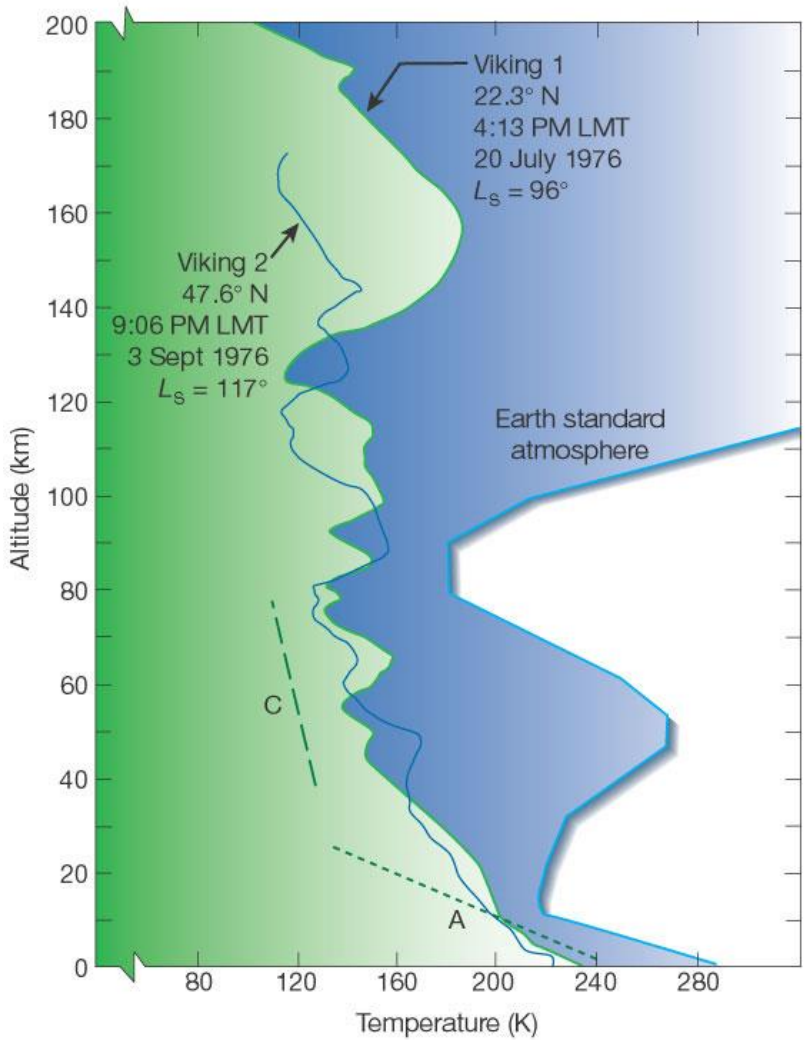

Figure 1.6: Martian atmosphere temperature profiles for the Viking landers compared to a standard earth atmosphere temperature profile. A and C show the Martian adiabatic lapse rate and CO_2 condensation temperature respectively. Adapted from [*Leovy*, 2001].

1.2.1 CO_2 ice clouds

CO_2 ice clouds on Mars are an extremely interesting atmospheric phenomenon, not just because they involve a substance other than H_2O ice, but because they involve condensing the major constituent of the atmosphere. Unlike H_2O ice clouds, this produces crystal growth that is not typically diffusion limited. Although CO_2 ice is present on other planetary bodies, Mars is currently the only known planet where study of these unusual cloud formations is feasible. An understanding of CO_2 clouds is crucial to accurately model the Martian atmosphere and assess the habitability of other extrasolar planets [*Selsis et al.*, 2007]. CO_2 clouds may also be of importance for understanding past Martian climate, in which CO_2 clouds in an early denser atmosphere could have warmed the Martian surface sufficiently to allow for liquid water [*Forget and Pierrehumbert*, 1997; *Forget et al.*, 2013; *Mischna et al.*, 2000; *Ramirez and Kasting*, 2017; *Wordsworth et al.*, 2013].

The first observations of CO_2 ice in the Martian atmosphere were performed by *Herr and Pimentel* [1970] using data from the Mariner 6 and 7 missions. A comparison of the observed reflectance at 4.3 µm with laboratory spectra for solid CO_2 suggested its presence within the atmosphere. The Mars Pathfinder mission in 1997 took images of blue cirrus-like features from the Martian surface (Figure 1.7) that further suggested the presence of high altitude CO_2 clouds [*Smith et al.*, 1997a].

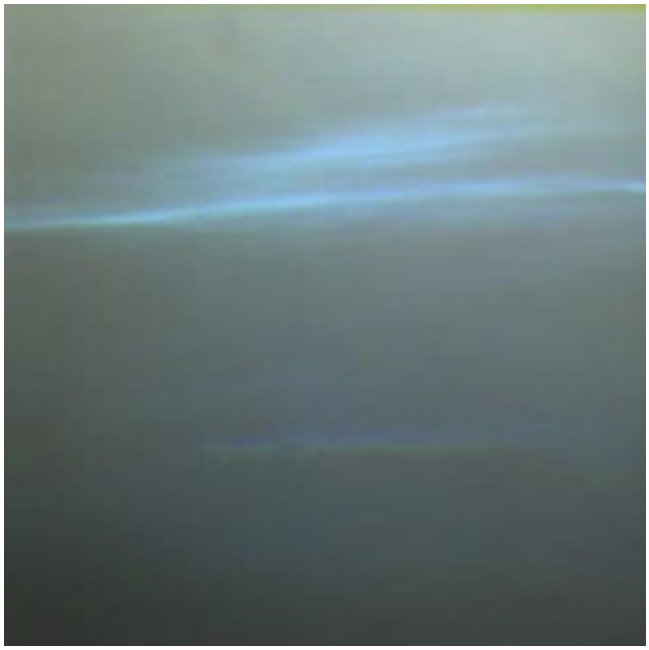

Figure 1.7: Picture taken from the Mars pathfinder rover of a suspected high altitude CO_2 cloud. Reproduced from *Smith et al.* [1997a].

Many studies produced indirect evidence of CO_2 clouds based on observed clouds linked to low atmospheric temperatures in which it would be possible for CO_2 to condense (see, for example [*Bell et al.*, 1996] or *Clancy and Sandor* [1998]). The first comprehensive spectral identification of Martian mesospheric CO_2 clouds was achieved in 2006 using the Observatoire pour la Minéralogie, l'Eau, les Glaces et l'Activité (OMEGA) instrument on board the Mars Express satellite. *Montmessin et al.* [2007] identified the characteristic solid CO_2 reflectance at 4.26 μm as well as ruling out the presence of H_2O ice or dust clouds.

Geographical and seasonal mapping of these high level CO_2 clouds has since been undertaken with an ever-increasing library of observed cloud formations. Cloud observations in the mesosphere are mainly attributed to CO_2 ice, while H_2O clouds are a minor component [*Vincendon et al.*, 2011]. Some example images from the Mars Express satellite are shown in Figure

1.8. The full range of these observed mesospheric CO_2 clouds covers altitudes from 60 to 100 km [*Clancy et al.*, 2007; *Montmessin et al.*, 2006].

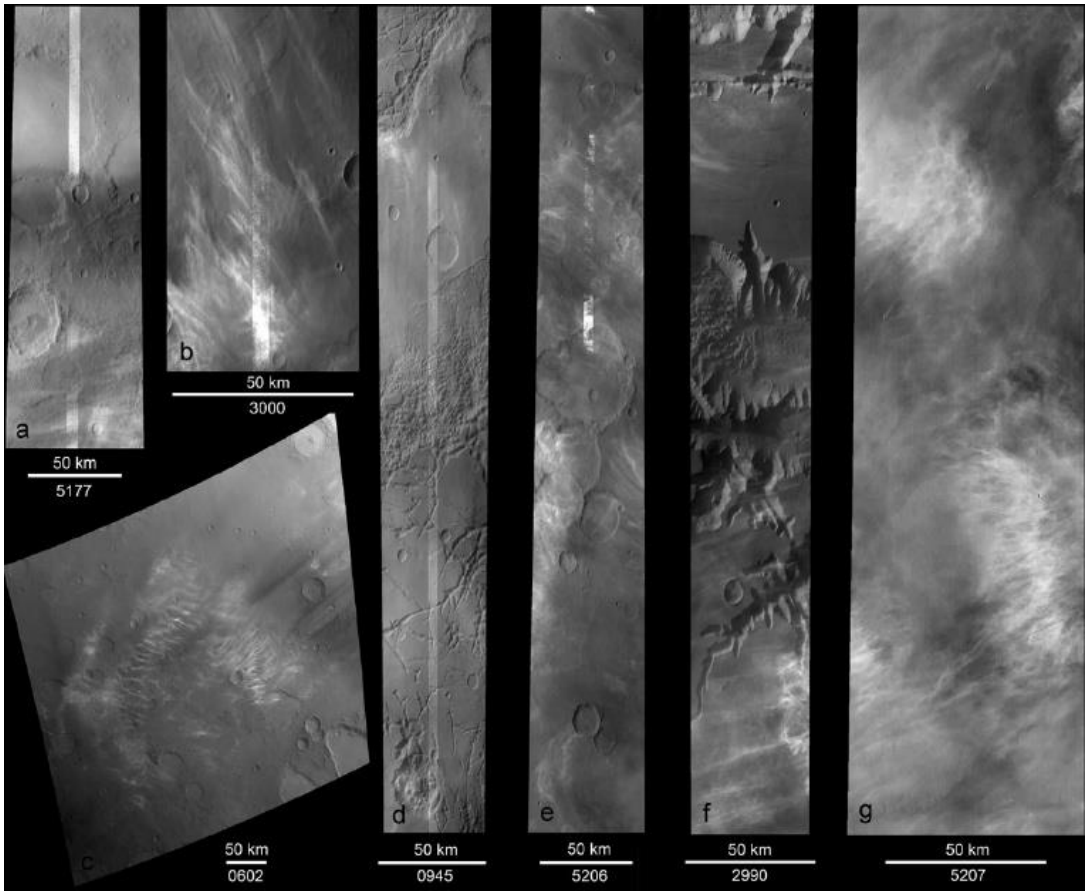

Figure 1.8: Pictures containing high altitude Martian cloud formations from the High Resolution Stereo Camera (HRSC), onboard the Mars express satellite. Reproduced from *Maattanen et al.* [2010].

Mesospheric CO_2 clouds are mostly constrained to equatorial regions (between 20ºN and 20ºS) around the northern hemisphere summer solstice at solar longitudes (Ls) of 0º - 140º when the mesosphere is coldest [*Listowski et al.*, 2013]. For reference in relation to the northern hemisphere, Ls = 90º is the summer solstice and Ls = 270º is the winter solstice. The two main types of these clouds vary depending on the time of day with daytime

and night-time clouds at altitudes of approximately 65 to 85 km and 90 to 100 km respectively. Night-time clouds consist of smaller particle radii (approximately 0.1 µm) compared to their daytime counterparts (1 – 3 µm radii) due to the higher altitude at which they form [*Montmessin et al.*, 2007; *Vincendon et al.*, 2011]. A third, less frequently observed type occurs in mid-latitude regions at altitudes of 53 – 62 km with mean particle radii of 2 µm [*Maattanen et al.*, 2010; *McConnochie et al.*, 2010]. These high altitude clouds are not typically observed during the Mars dust storm season at L_s =180º - 330º [*Clancy et al.*, 2007; *Zurek and Martin*, 1993]. This is due to warming of the atmosphere by the dust layer, which leads to mesospheric temperatures that are not conducive for cloud formation [*Forget et al.*, 1999; *Smith et al.*, 2002].

CO_2 clouds are also present within the troposphere at altitudes less than 20 km, forming in polar regions during the night with particle radii up to 100 µm [*Hayne et al.*, 2012]. They form predominantly during northern hemisphere winter when temperatures closer to the surface are low enough for CO_2 condensation [*Hu et al.*, 2012]. Unlike mesospheric clouds these tropospheric clouds can precipitate CO_2-snow down to the Martian surface, when temperatures are low enough (< 145 K). This is thought to contribute to the accumulation of ice at the poles during winter, a process that reduces the atmospheric pressure by up to 20% [*Hayne et al.*, 2014; *Hourdin et al.*, 1993].

1.2.2 Microphysics of CO_2 clouds

Particle radii as large as 3 µm in daytime mesospheric CO_2 clouds are surprisingly large, considering these clouds are formed at altitudes of up to

85 km [*Vincendon et al.*, 2011] where the sedimentation velocity exceeds 10 m s^{-1}. These particles are much larger than the small ice crystals of Earth's PMCs (subsection 1.1.3) [*Hinson and Wilson*, 2002]. This large particle size is not assisted by rapid crystal growth which had been previously assumed due to the abundance of available CO_2. The rarefied atmosphere limits heat transport while maintaining a high temperature difference between the crystal and gas phase, which leads to low crystal growth rates after a critical ice germ has formed. As a consequence, this limits the maximum ice particle radii [*Listowski et al.*, 2013]. It is also hypothesised that mesospheric updrafts caused by moist convective processes may counteract the rapid sedimentation of the particles and therefore account for the larger than expected CO_2 particle sizes [*Colaprete and Toon*, 2003; *Maattanen et al.*, 2010]. As with H_2O clouds the amount of available INP also affects ice particle size with increased INP concentrations leading to predictions of a greater number of smaller CO_2 crystals [*Colaprete et al.*, 2008; *Maattanen et al.*, 2005].

The extremely low temperatures required for CO_2 deposition (CO_2 frost point temperatures as low as 95 K) are not normally reached in the mesosphere. This has led to speculation that the propagation of gravity waves is required to achieve localised areas of lower temperatures or 'cold pockets' in a similar fashion to the Earth's mesosphere [*Clancy and Sandor*, 1998; *Gonzalez-Galindo et al.*, 2011]. Recent studies have found a correlation between CO_2 cloud occurrence and suitable conditions for gravity wave propagation during equatorial summer. This suggests that gravity waves are necessary to create these 'cold pockets' in which CO_2 clouds can form [*Spiga et al.*, 2012]. These localized low temperature regions constrain the location and

the vertical and horizontal morphology of the clouds. The wave patterns seen in the cirrus-like structures shown in Figure 1.8 illustrate the gravity waves effects.

Homogeneous nucleation of CO_2 is predicted to require very high supersaturation conditions and is thought to be an unlikely pathway to CO_2 cloud formation in the Martian atmosphere under realistic temperature conditions [*Maattanen et al.*, 2005; *Maattanen et al.*, 2010]. It is also thought that ion-induced nucleation would not be able to compete with heterogeneous nucleation in CO_2 clouds on Mars [*Listowski et al.*, 2014]. As is the case for PMCs on Earth, heterogeneous ice nucleation *via* deposition of CO_2 is therefore thought to be the likely nucleation pathway to cloud formation [*Maattanen et al.*, 2005].

Experimental studies concerning heterogeneous Martian CO_2 ice nucleation are extremely limited compared to Martian and terrestrial H_2O ice nucleation. Generally experimental studies regarding CO_2 ice have been tailored towards the similar focus of the CO_2 trapping described in subsection 1.1.5, regarding its occurrence in the ISM or its presence on Mars polar caps [*Escribano et al.*, 2013; *Malyk et al.*, 2007; *Trainer et al.*, 2010]. The only experimental study to date of the kinetics of CO_2 ice nucleation relevant to the Martian atmosphere (theory detailed in subsection 1.3) was undertaken by *Glandorf et al.* [2002] using a similar UHV-based experimental setup. Instead of dust or MSP analogue, H_2O ice condensed onto a Si wafer was used as a substrate. *Via* the use of reflective absorbance infra-red spectroscopy (RAIRS) the broadening and strengthening of the asymmetric stretch and bend absorbance features of CO_2 were used to estimate the

point of nucleation. This led to a series of critical saturation (S_{crit}) and contact parameters (m) for CO_2 ice nucleation across the temperature range 130 to 140 K. Using CNT a critical nucleation rate of 1 cm^{-2} s^{-1} was assumed, determining a S_{crit} of ~1.34 and an m = 0.95, suggesting H_2O would act as an efficient INP under these conditions (m = 1 is a theoretical "perfect" INP). A lack of consideration for the effect of dust particles in heterogeneous CO_2 nucleation (possible INPs are discussed in subsection 1.2.3) is apparent in the literature, while the temperatures studied are ≥ 40 K above typical saturation temperatures in the mesosphere. Subsequent modelling of CO_2 clouds has often relied on this set of CNT parameters (such as *Maattanen et al.* [2005], the theory of which is described in subsection 1.3). Due to the limitations of the dataset, approximations were required for CO_2 nucleation on dust with a contact parameter for water ice on dust used instead (m = 0.97). This again lacks applicability to CO_2 clouds which are observed at mesospheric altitudes.

CO_2 clouds included in Mars general circulation models have sometimes treated CO_2 nucleation as activated when any super-saturation was achieved (i.e. S > 1) regardless of the likely need for increased super-saturation for significant nucleation rates to occur [*Forget et al.*, 1998]. The first model to allow for super-saturation conditions and inclusion of mesospheric CO_2 clouds again used the values of *Glandorf et al.* [2002] but overestimated ice crystal growth rates [*Colaprete et al.*, 2008]. Recent developments have better accounted for reduced growth rates at high supersaturations allowing for more accurate modelling of cloud lifetimes, effective crystal radii and opacities when compared to observations [*Listowski et al.*, 2013; *Listowski et al.*, 2014]. Modelling by *Yiğit et al.* [2015]

used sub grid-scale gravity waves to produce local temperature minimums necessary to facilitate CO_2 nucleation. *Yiğit et al.* [2015] was generally able to use this method to reproduce observed clouds but did not include detailed microphysics, instead determining cloud formation at S = 1.35 (taken from *Glandorf et al.* [2002]). This led to an over-prediction of clouds in polar regions and globally at high altitudes. Due to the steep temperature gradients required from gravity waves to form CO_2 clouds, understanding the microphysics and determining cloud activation temperatures is crucial to correctly model observed cloud occurrence.

1.2.3 Possible INPs in Martian clouds

The variety of possible INPs present for heterogeneous ice nucleation on Mars (both for H_2O and CO_2) shows marked differences compared to Earth. Mars does not have INP sources such as oceanic and biogenic aerosols, so there is a smaller variety of possible INPs available. Over recent decades, using satellite measurements as well as data from the Viking Landers and the Mars Exploration Rovers, it has become apparent that Martian surface dust has a reasonably global uniformity [*Yen et al.*, 2005]. The dominant mineralogy is that of basaltic rocks, with feldspar rich dusts, Mg/Fe phyllosilicates such as Kaolinite ($Al_2Si_2O_5(OH)_4$) and zeolites identified at multiple locations on the Martian surface [*Aronson and Emslie*, 1975; *Clark et al.*, 1982; *Mustard et al.*, 2008; *Ruff*, 2004]. The recent Mars Curiosity mission has led to one of the most comprehensive analyses of dust from the Martian surface to date, *via* X-ray diffraction (XRD) with the major components being plagioclase feldspars and forsteritic olivine (Mg_2SiO_4) [*Bish et al.*, 2013].

As well as the lack of variety in aerosol sources, the high frequency of dust storms (including global storms) is thought to be the reason behind the similarities in surface dust mineralogies regardless of geographic location [*Bish et al.*, 2013; *Elteto and Toon*, 2010]. These dust storms can inject aerosols high into the mesosphere (> 60km) and could be a source of INP for CO_2 and H_2O clouds [*Clancy et al.*, 2010]. For night-time CO_2 clouds (forming above 80 km) the dust maxima (defined as the point of highest dust mixing ratio) is typically below 30 km [*Heavens et al.*, 2011], while for daytime clouds (forming as low as 60 km) the dust maxima is up to 65 km [*Guzewich et al.*, 2013]. This suggests Martian Dust particles (MDPs) could in some cases act as INP for daytime CO_2 clouds in the lower mesosphere. However, modelling of the mesosphere has shown that elevated surface dust alone cannot account for the thickness of observed high altitude CO_2 clouds [*Listowski et al.*, 2014]. The occurrence of MDPs at high altitudes is also often coupled with a warming of the atmosphere due to increased dust loading, which produces conditions not conducive to CO_2 ice formation.

A sporadic ionospheric layer has been observed between 65 and 110 km and attributed to the ablation of meteors [*Pätzold et al.*, 2005]. Using instruments on board the Mars Atmosphere and Volatile EvolutioN (MAVEN) spacecraft Mg^+ and Fe^+ has been observed in the upper atmosphere of Mars [*Benna et al.*, 2015; *Schneider et al.*, 2015]. It has also been predicted that Mg and Fe layers (and subsequent polymerisation to form MSPs e.g. MgOH and $MgCO_3$) could be present at CO_2 cloud altitudes [*Whalley and Plane*, 2010]. It is therefore thought that, in regards to high altitude clouds, MSPs could act as INP similarly to PMCs on Earth (discussed in subsection 1.1.1) [*Listowski et al.*, 2014]. H_2O ice is also thought to be a possible INP for

heterogeneous nucleation of CO_2 and is currently the only INP that has been experimentally investigated (*Glandorf et al.* [2002], see subsection 1.2.2) [*Isenor et al.*, 2013; *Pollack*, 1977]. H_2O ice clouds have been observed up to altitudes of 80 km during southern spring consistent with observations of H_2O concentrations above saturation [*Maltagliati et al.*, 2013; *Vincendon et al.*, 2011]. However CO_2 clouds are not typically observed at this time, and during their main occurrence period, H_2O supersaturations are confined to altitudes below 50 km. This further brings into question the validity of using the H_2O substrate measurements of CO_2 nucleation by *Glandorf et al.* [2002] to describe high altitude CO_2 clouds and the need for study of nucleation on particles more analogous to the mesosphere.

1.2.4 Crystallographic properties of CO_2 ice on Mars

The structure and thermodynamic properties of CO_2 ice particles are also important for building a detailed understanding of the formation of mesospheric CO_2 clouds. As discussed in the previous subsections, accurate parameterization of these clouds helps in understanding the Martian climate as a whole (past and present). This understanding of particle properties is also pertinent for precipitation and CO_2 ice formation at the Martian regolith [*Hayne et al.*, 2014].

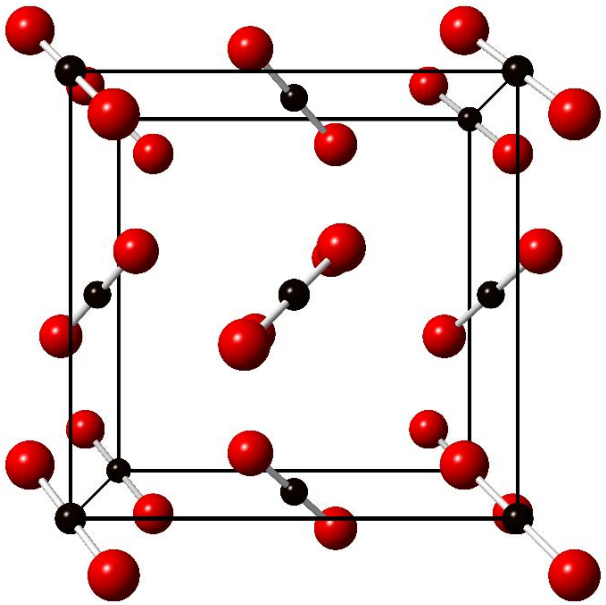

Figure 1.9: Unit cell of cubic CO_2-I. Carbon and oxygen atoms are indicated by the black and red spheres respectively. The diagram was produced using the software package Diamond [Crystal Impact].

Low pressure CO_2 ice has previously been described with a cubic structure with crystal symmetry of space group *Pa*-3 (No. 205) [*de Smedt and Keesom*, 1924]. A single lattice parameter, *a*, is needed to describe the unit cell since $a = b = c$ and $\alpha = \beta = \gamma = 90°$. The cubic symmetry of the unit cell can be seen in Figure 1.9. The single lattice parameter of this ice (assigned as CO_2-I) has been previously determined with limited temperature resolution at low temperatures (<115 K) and under unknown deposition pressure conditions [*Keesom and Kohler*, 1934a; b; *Maass and Barnes*, 1926]. Given the variability in the forms of H_2O ice at low temperatures and pressures [*Murray et al.*, 2015], it would be worth investigating the crystal structure of CO_2 ice under Martian atmospheric conditions.

Parameters related to CO_2 crystal structure such as CO_2 ice density vary in the literature at low temperatures relevant to mesospheric CO_2 clouds. A temperature-independent CO_2 density value of 1.6 g cm^{-3} is often used in nucleation and modelling studies [*Listowski et al.*, 2013; *Listowski et al.*, 2014; *Maattanen et al.*, 2007; *Maattanen et al.*, 2005; *Wood*, 1999]. While the density of H_2O ice remains relatively constant over the temperature range of the Martian atmosphere, it is known that the density of CO_2-I ice is temperature dependent, but is poorly constrained through the Martian mesospheric temperature range. The commonly used CO_2 ice density value of 1.6 g cm^{-3} is applicable to 168 K, a temperature higher than is relevant for CO_2 cloud formation, and is based originally on density values determined by *Maass and Barnes* [1926]. This is lower than density values determined for CO_2 ice at 83 K of 1.68 g cm^{-3} in a study by *Keesom and Kohler* [1934a] (later corrected by *Curzon* [1972]). Inaccuracies in the density value used for CO_2 ice will affect parameters such as ice nucleation, particle growth and sedimentation rates in the modelling of CO_2 clouds and are worth refining.

1.3 Classical nucleation theory for mesospheric CO_2 clouds

As discussed in subsection 1.2.2 heterogeneous ice nucleation *via* deposition of CO_2, in which the energy barrier to nucleation is reduced by the presence of an INP, is thought to be the likely nucleation pathway for CO_2 clouds on Mars [*Maattanen et al.*, 2005]. CNT is used to describe this nucleation and specifically heterogeneous nucleation induced by surface diffusion was used in the analysis of results in Chapter 5 and 6. This theory assumes that CO_2 molecules stick for a certain period of time on the INP and can then diffuse to combine and form clusters; this may result in a critical

cluster leading to stable nucleation of CO_2 ice on the particle. Described here, the theory has been previously applied to the study of CO_2 ice clouds [*Listowski et al.*, 2014; *Maattanen et al.*, 2007; *Maattanen et al.*, 2005]. The rate of heterogeneous ice nucleation (J_{het}) for a spherical INP is given by:

$$J_{het} = A_N Z_{het} \beta_{het} c_{1,s} \exp\left(\frac{-\Delta F_{het}}{kT}\right) \quad (1.1)$$

where A_N is the surface area of the INP; Z_{het} is the heterogeneous Zeldovich factor which corrects for the dissociation of super-critical clusters; β_{het} accounts for the flux of CO_2 molecules on the INP *via* diffusion to form the critical cluster; $c_{1,s}$ is the concentration of monomers on the INP surface and ΔF_{het} is the free energy of forming the critical cluster on the surface of the INP, determined from the Gibbs-Thomson equation. ΔF_{het} is calculated in relation to the homogeneous form (ΔF_{hom}) with a reduction in the energy barrier by a factor $f(m,x)$ as described in *Fletcher* [1958]. The complete ΔF_{het} description is given by:

$$\Delta F_{het} = f(m,x) \frac{16\pi V^2 \sigma^3}{3(kT \ln S)^2} \quad (1.2)$$

where V is the molecular volume in the condensed phase (m_m/ρ, where m_m is the mass of the molecule); σ the surface tension (0.08 J m^{-2} taken from *Wood* [1999]); and S the saturation ratio of CO_2; x is the ratio of the size of the INP to the critical cluster, and m is the contact parameter equal to cos θ, which relates to the contact angle between the INP and the nucleating phase. The concept of m is shown in Figure 1.10, where a reduction in the contact angle reduces the overall surface area of the spherical ice cluster while increasing the proportional surface area exposed to the INP surface. This gives a reduction in the energy barrier (ΔF_{het}) to nucleation in CNT.

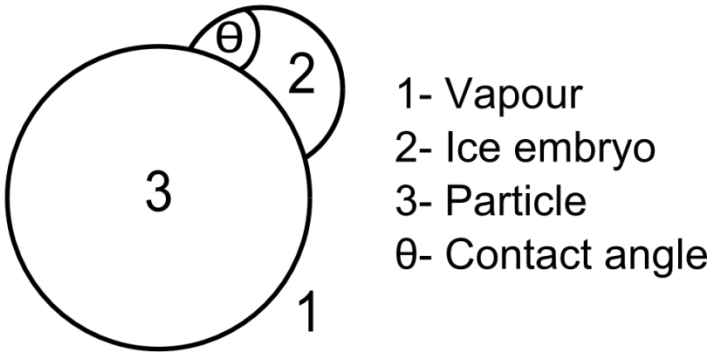

Figure 1.10: Representation of the contact angle parameter (*m*) of an ice embryo on the surface of an INP regarding deposition ice nucleation using CNT.

1.4 Project aims

This literature review has highlighted several research questions and aims to be investigated within this thesis, that relate to the formation and composition of ice in the mesospheres of both Earth and Mars. Four key research questions and aims of this thesis are described here, two relating to PMCs on Earth (section 1.4.1) and two relating to mesospheric CO_2 clouds on Mars (section 1.4.2).

1.4.1 Research questions relating to PMCs on Earth

The Earth's mesosphere contains within it the highest and coldest cloud formations on Earth, where temperatures can reach as low as 90 K as well as relatively high ratios of CO_2:H_2O (> 37:1) [*Emmert et al.*, 2012; *Lübken et al.*, 2009]. CO_2 trapping in H_2O ice matrices has been shown to occur under

different ratios of CO_2:H_2O and temperatures than is relevant for the mesosphere [*Galvez et al.*, 2008; *Hodyss et al.*, 2008a; *Hodyss et al.*, 2008b; *Mate et al.*, 2008]. The first aim of this project is therefore to investigate experimentally whether high CO_2:H_2O ratios could lead to gaseous CO_2 trapping within mesospheric ice particles, acting as a temporary sink of CO_2. This question is answered through the use of TPD experiments in a UHV chamber *via* deposition of representative CO_2 and H_2O fluxes, with the results of this aim detailed in Chapter 3.

Uptake of metals on PMCs has been shown to significantly deplete the metal layers of Fe, Na and K in the mesosphere [*Gardner et al.*, 2005; *Plane et al.*, 2004; *Raizada et al.*, 2007]. It has been suggested that mesospheric Mg could also be depleted by uptake on PMC ice particles [*Langowski et al.*, 2015]. The uptake and reactivity of Mg on ice and experimental determination of the reactive products of K on ice does not appear to have been studied experimentally. The uptake and reactivity of Mg and K is therefore investigated here using the UHV chamber mentioned above and the results are described in Chapter 4.

1.4.2 Research questions relating to Martian mesospheric CO_2 clouds

The mesosphere of Mars contains the only observable occurrences of CO_2 clouds. The microphysics of CO_2 ice formation in these clouds, as well as the INP required for nucleation are currently not well understood and are subject to great uncertainty in cloud models. The only experimental study of CO_2 nucleation by *Glandorf et al.* [2002] was done using a H_2O ice substrate at temperatures too high for the Martian mesosphere (> 130 K). CO_2 nucleation

has not been investigated on representative nanoparticles (such as MSP analogues) or under more representative temperature conditions observed in the Martian mesosphere. In order to improve the parameterization of these CO_2 clouds using CNT (section 1.3), CO_2 deposition on analogue MSP nanoparticles is investigated here using a novel experimental setup called the Trapped Reactive Atmospheric Particle Spectrometer (TRAPS). The results of these experiments are discussed in Chapter 5.

The phase diagrams of some compounds, such as water ice, display complexity with the presence of multiple metastable and stable phases at low temperatures and pressures [*Hobbs*, 1974; *Petrenko and Whitworth*, 1999; *Salzmann et al.*, 2011]. The CO_2 ice structure has never been previously determined experimentally under conditions of deposition growth analogous to the temperature and pressure conditions of clouds in the mesosphere of Mars. Determination of low temperature phases of CO_2 ice or confirmation of an existing phase of relevance to ice formation in the Martian atmosphere is therefore worth investigating. An understanding of the fundamental parameters of CO_2 ice such as ice density and crystal shape are also important for further reducing uncertainties in the modelling of CO_2 clouds on Mars. In order to answer this aim, CO_2 deposition is investigated under Martian temperature and pressure conditions in an environmental chamber, probed by XRD. The results are detailed in Chapter 6.

2 Experimental apparatus and instrument development

This chapter describes the range of experimental apparatus used throughout the results chapters of this thesis, to answer the aims detailed in Chapter 1. A UHV chamber is described, which was used to investigate CO_2 trapping in amorphous ice in chapter 3 and to investigate Mg and K uptake on ice in chapter 4. A RAIRS system is detailed which was designed and built to complement the analysis available for studies in the UHV chamber. Spectra of the IR peak positions of benzene were used to test the RAIRS system and evaluate its capabilities. The TRAPS instrument at KIT was used in chapter 5 to investigate CO_2 nucleation on nanoparticles. Finally, an XRD chamber system and flow setup is described in chapter 6 and was used to determine the fundamental properties of CO_2 ice under Martian conditions.

2.1 UHV chamber studies

In order to investigate ice particles relevant to PMCs a UHV chamber system was used. The UHV chamber is described in subsection 2.1.2, while the specific experimental methodology utilising the UHV chamber is contained within the results chapters 3 and 4.

2.1.1 Why use UHV?

The use of UHV allows for the use of a variety of analytical methods for nanoscale surfaces and has several key advantages over higher pressure systems. Due to the extreme low pressures within the UHV chamber (in this system, typically 3×10^{-9} mbar) the mean free path of a H_2O molecule is approximately 19 km. This means that in the 30 cm diameter chamber described below, gas molecules collide far more frequently with the walls of the chamber than with each other. Thus, gas-surface interactions dominate over gas-gas interactions. This ensures that, during dosing, species directed at the substrate interact with the substrate surface first before interacting with residual gas phase molecules in the chamber. The combination of a low pressure environment, and the ability to resistively heat or energetically sputter the sample allows for the preparation of atomically clean sample surfaces. The molecular flux of contaminants from the residual gas is also drastically reduced with decreasing pressure. Under UHV conditions these clean surfaces can be maintained for several hours. Using the Hertz-Knudsen equation under the conditions of the UHV chamber (described in subsection 2.1.2) and assuming a sticking coefficient of 1, it would take several hours to build up just one monolayer (approximately 1×10^{15} molecules) of contaminant on the sample. This is crucial for

experiments taking several hours that look at the interaction of thin ice films with monolayer scale depositions of CO_2 or metal species. Given the focus of the thesis, the use of a UHV chamber for the reasons discussed above provides a suitable environment for producing ice layers analogous to the nanoscale ice particles in the low pressure region where PMCs form.

2.1.2 The UHV system

The experimental system used in this thesis comprises at its core the central UHV chamber with a selection of sample preparation and characterisation instruments. This instrument has been described in part elsewhere [*Frankland and Plane*, 2015; *Vondrak et al.*, 2006; *Vondrak et al.*, 2009] and is described in detail here. The UHV chamber (shown in Figure 2.1) is a cylindrical stainless steel chamber with a diameter of 30 cm and a volume of approximately 25 L. This system is pumped down to pressures of 3×10^{-9} mbar by a 550 L s^{-1} turbomolecular pump (Varian, TV551 Navigator), which in turn is backed by a high vacuum rotary pump (Varian, DS302). The pressure within the chamber is measured by an ionization gauge (Varian UHV-24), capable of measuring pressures as low as 2×10^{-11} mbar. In order to remove residual water from the system, and achieve lower pressures of 10^{-10} mbar, the system can be baked using ceramic heaters at 450 K for several days. However, due to the introduction of heat-sensitive KBr windows for the IR system (described in section 2.2), bake out was not usually carried out. The UHV chamber is made up of three levels of ports and attachments (levels A, B and C) with Level C containing the preparation and characterisation instruments; a top down schematic diagram of this level is shown in Figure 2.1. The UHV chamber is currently equipped with a

monolayer deposition source (Caburn MCD LTd., e-vap 100) used for Mg deposition (Goodfellows, 99.9+% purity), a shrouded alkali metal dispenser for K deposition (Saes Getters, K/NF/4.5/25 FT10+10) and a needle valve (NUPRO, SS4BK) linked to a glass gas-handling line. The inert ion (Ar^+ or Kr^+) sputter source (PSP technology Ltd., ISIS 3000) is used for energetic ion sputtering of the sample but can be modified in order for it to function as a leak valve, enabling background dosing for the calibrations described in section 3.2. The chamber is also equipped with a quadrupole mass spectrometer (QMS) (Hiden, HAL 3F 301 RC PIC) which is mounted at level C for the experiments in this thesis but can be lowered to level A if necessary.

Within the centre of the UHV chamber is a Cu(111) crystal sample of 12 mm diameter and 2.5 mm thickness, polished to 1 μm and oriented to ± 0.5º of the (111) plane. This is mounted onto the end of a liquid N_2 cooled oxygen free high conductivity (OFHC) copper cold finger which in turn is mounted onto an xyzθ manipulator. The base temperature of this sample is dependent on the quality of the connection to the W wires when mounted, and has ranged from 98 – 110 K across the studies described in this thesis. The sample can be heated resistively by tungsten wires embedded in the perimeter of the Cu(111) crystal, powered by a high voltage supply (Agilent, 6572A). The Cu crystal surface temperature is monitored using a K-type thermocouple positioned in a small hole on the side of the Cu(111) crystal.

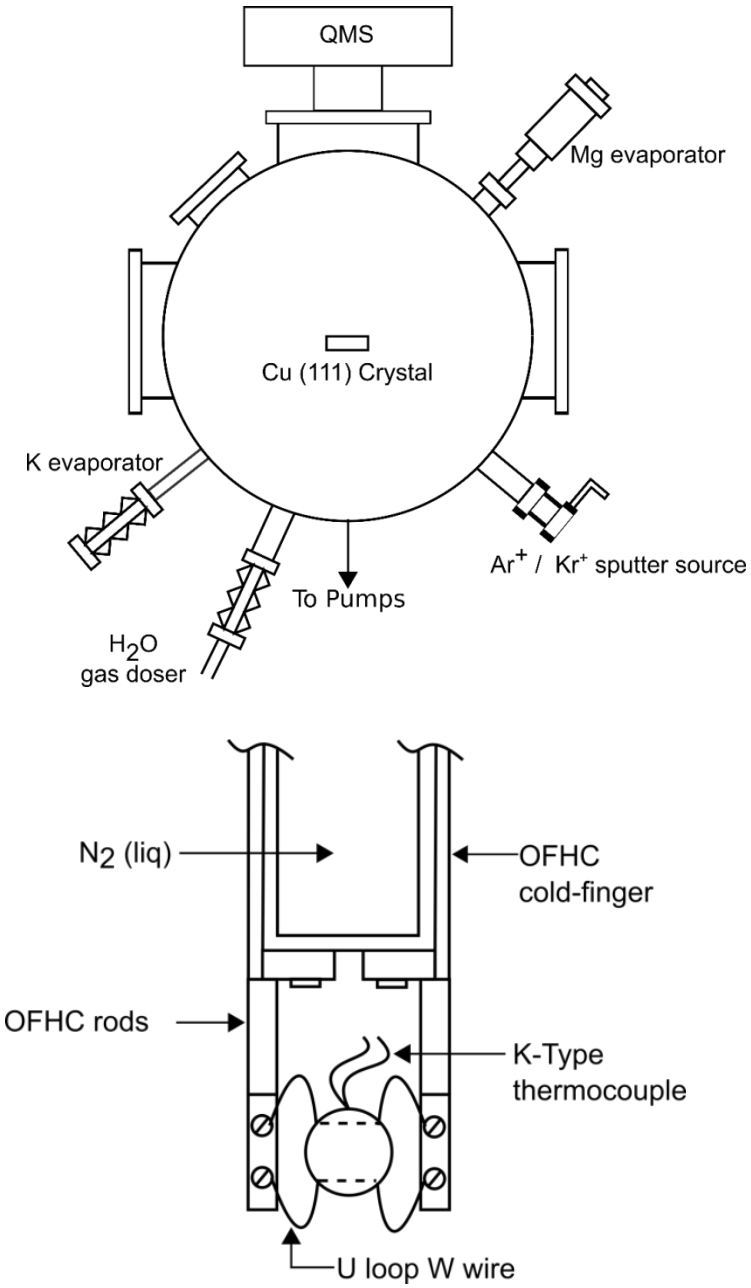

Figure 2.1: Schematic diagrams of a top-down view of the UHV chamber and level C instruments (top) and side view of the Cu(111) substrate mounted to the OFHC copper cold finger.

The needle valve and inert ion sputter source on the UHV chamber are directly connected to a glass gas-handling line where preparation and purification of gases, vapours and mixtures for use in the UHV chamber is carried out. The glass gas-handling line is pumped by a diffusion pump

(Edwards, B34431978) which is backed by a rotary pump (Edwards, E2M5). The pressure between the diffusion and rotary pumps is measured using a gauge (Edwards, 501), while the pressure in the gas line is monitored using two Baratron gauges, 0-10 and 0-1000 torr (MKS baratron 622A). The use of CO_2 and H_2O in this glass gas-handling line are described in Chapter 3, while the use of H_2O, Ar and Kr are detailed in Chapter 4.

2.2 RAIRS system: Design and testing

A new addition to the UHV system developed during this PhD project was a RAIRS system to perform IR spectroscopic measurements of species adsorbed to the sample within the UHV chamber.

2.2.1 Why use RAIRS?

Vibrational spectroscopy is a useful tool for studying the bonding of atoms regardless of whether they are in a gaseous or condensed phase. IR spectroscopy can provide specific information on the types of bonds present (and therefore what compounds are present), the crystal structure and the orientation of molecules in a sample [*Backus et al.*, 2004]. RAIRS has also been used to determine the point of ice nucleation in substrate-based experiments [*Iraci et al.*, 2010; *Phebus et al.*, 2011]. RAIRS is also non-destructive, allowing it to be combined experimentally with other analysis techniques without altering the sample.

IR spectra result from transitions between quantised vibrational energy levels. Molecules can have a range of vibrational motions in the IR *via* the stretching and bending modes of bonds. A combination of observed IR absorption bands (peak position and peak shape) gives information on the bonds present in a molecule and can also provide information regarding bonding sites and molecular orientation.

In order for a molecule to be IR active there must be a change in dipole moment as a result of the vibration that is induced when IR radiation is absorbed. The surface selection rule describes when a molecular vibration is IR active, as shown in Figure 2.2. When a molecule is orientated parallel to

the surface it is adsorbed to, the oscillating molecular dipole (μ_M) is cancelled out by the opposing force of the oscillating image molecular dipole (μ_I) of the surface. Thus the molecular vibration is IR inactive. However, when a molecule is orientated perpendicular to the surface the dipole interactions are reinforced meaning it is IR active [*Greenler*, 1966].

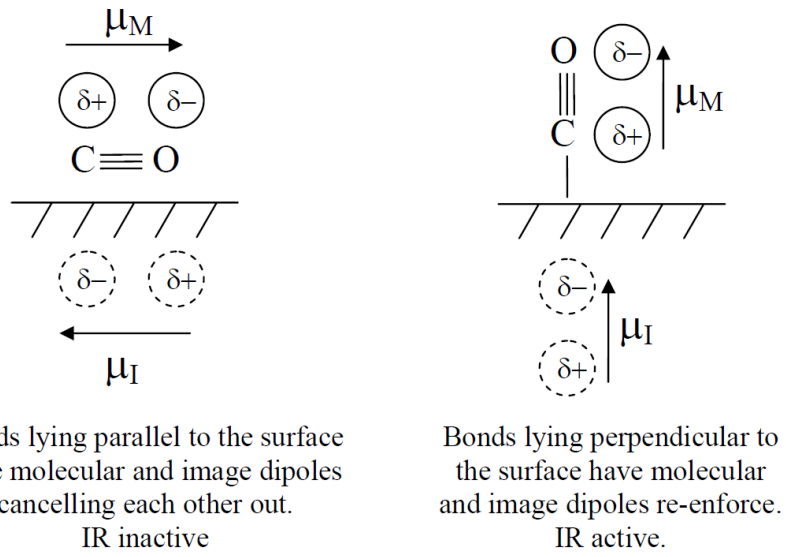

Figure 2.2: Illustration of the surface selection rule for RAIRS. Reproduced from *Attard* [1998].

Due to the opacity of the metal substrates used in the UHV chamber, transmission experiments are not a viable option leading to the use of the reflection mode RAIRS. The RAIRS system developed for this UHV chamber is described in the following subsection.

2.2.2 RAIRS design

Figure 2.3 shows a schematic diagram of the UHV chamber at level A with the designed optical system. This consists of a Fourier transform IR (FTIR) spectrometer (Bruker, IFS 66/S) with an expandable spectral range from far IR to the near UV. This spectrometer is equipped with a mid IR source (Globar) that is externally cooled by deionised water (Aquatherm WGB). Within the interferometer of the spectrometer a germanium (Ge) on potassium bromide (KBr) beamsplitter (Bruker, T303/8A) is installed covering the spectral range of 370 – 7800 cm^{-1}. This beamsplitter can be switched out to access higher wavelengths. The spectrometer is purged using a regulated dry N_2 flow of 600 L/hr. This protects the optics and importantly reduces unwanted noise in the IR spectrum from the absorbance of CO_2 and H_2O. For internal sampling the system contains an IR detector (Bruker, DLATGS KBr) with a spectral range of 360 – 12000 cm^{-1}. For external sampling the beam is rerouted through the UHV chamber by a custom designed optical system.

To enable transmission of IR through the chamber and onto the sample, the UHV chamber was equipped with KBr vacuum viewports (MDC Vacuum Ltd., DN40CF) at port positions 3 and 7. These windows can become degraded if heated to a temperature above 320 K, which is the reason that the UHV chamber could not be baked out (in a typical bake out a temperature of 450 K is reached). This means the minimum achievable UHV chamber pressure was limited to the 10^{-9} mbar range. These conditions still provide the low pressures necessary for UHV work. A series of mirrors encased within a purged system was required in order to manipulate the

beam through the UHV chamber to reflect off the Cu(111) sample and out to an external detector. Custom designs for the purge box and detector purge box that house the optics are shown in Figure 2.4.

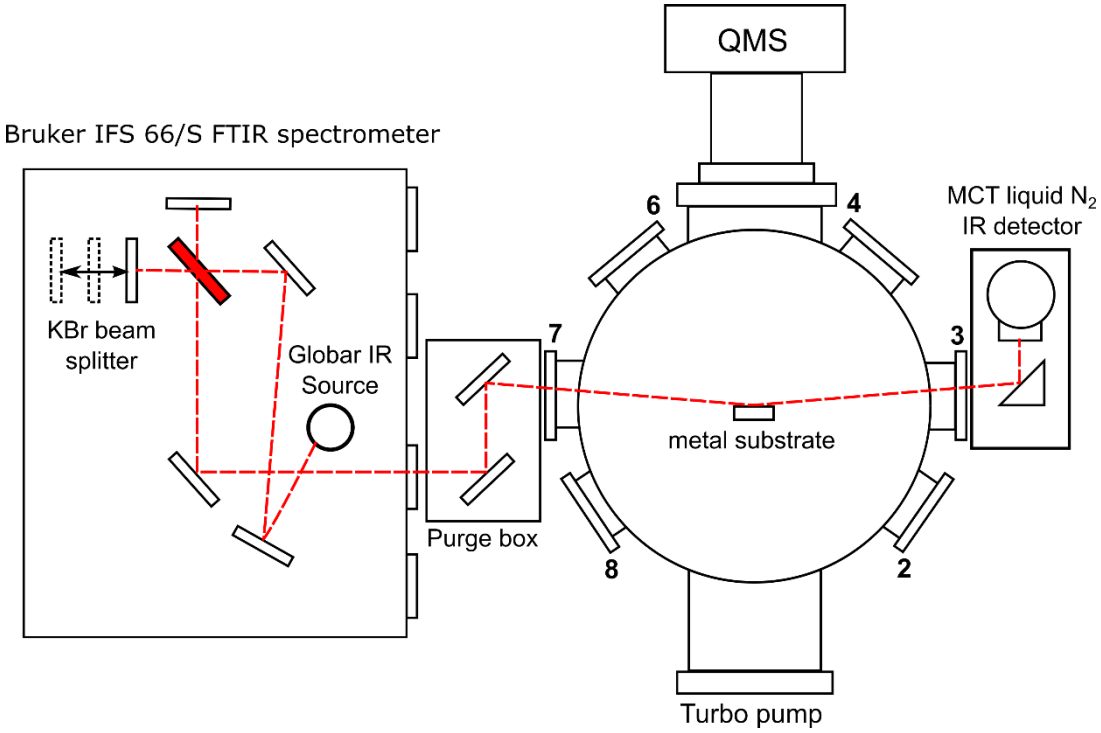

Figure 2.3: Schematic diagram of the UHV chamber (level A) and Bruker IFS 66/S FTIR spectrometer with details of the optical setup. The red dotted lines indicate the IR beam path from the Globar IR source within the spectrometer to the external mercury cadmium telluride (MCT) detector.

The mirror system comprises a periscope arrangement in the first purge box (Figure 2.4a), containing a 5 cm diameter flat silver mirror to angle (as the IR beam exits the spectrometer) the beam at an angle of incidence of 45º. The second mirror is a 5 cm diameter concave silver mirror (approximate focal length 28 cm), that is used to focus the IR beam onto the metal substrate in the centre of the UHV chamber. This two mirror arrangement allows for easy IR beam manipulation into the chamber and ensures that the beam is

efficiently reflected at angles of incidence close to 45º (reflectance of > 95 % across the mid-IR range). The second purge box (Figure 2.4b) is positioned after the beam has passed through the UHV chamber and reflected off the substrate. This purge box contains a 5 cm diameter silver off-axis parabolic mirror, with a focal length of 10 cm (where the external detector is positioned). This focusing ensures that as much of the light reflected from the substrate as possible reaches the sensor of the detector. The external detector is a liq-N_2 cooled mercury cadmium telluride (MCT) IR detector with a spectral range of 420 – 5000 cm^{-1} (InfraRed associates, MSL-8). The mirrors in the first purge box are attached to 2-point kinematic mounts while the parabolic mirror is attached to a 3-point kinematic mount, which allow for fine adjustment of the reflected angle of the IR beam.

The purge boxes are connected to the UHV chamber through flexible PolyVinyl Chloride (PVC) tubing and nylon flanges in order to ensure a sustained purge, thereby reducing beam contamination by residual mid-IR absorbing gas species present in the lab such as CO_2 and H_2O. Both purge boxes are purged from the same N_2 line as the spectrometer, with a needle valve used to distribute a comparatively reduced flow to the purge boxes. The use of flexible PVC tubing to connect the mirror systems increases the range of beam angles that can be readily accessed and enables easy beam alignment by shifting the position of the purge box containing the parabolic mirror and MCT detector. As the KBr windows on the UHV chamber are water soluble, both boxes contain silica gel beads in order to absorb H_2O vapour, thus reducing the humidity within the system and minimising degradation of the windows. These KBr windows have excellent transmission across a 330 – 40000 cm^{-1} range, while the current optics

provide high reflectivity from 400 – 22000 cm^{-1}. Combining this with the ability to switch the external detector and spectrometer IR source to access other frequency ranges (e.g. a NIR detector for the range 4000 - 12500 cm^{-1}) gives great flexibility in the range of absorption bands that could be studied, depending on the molecule in question.

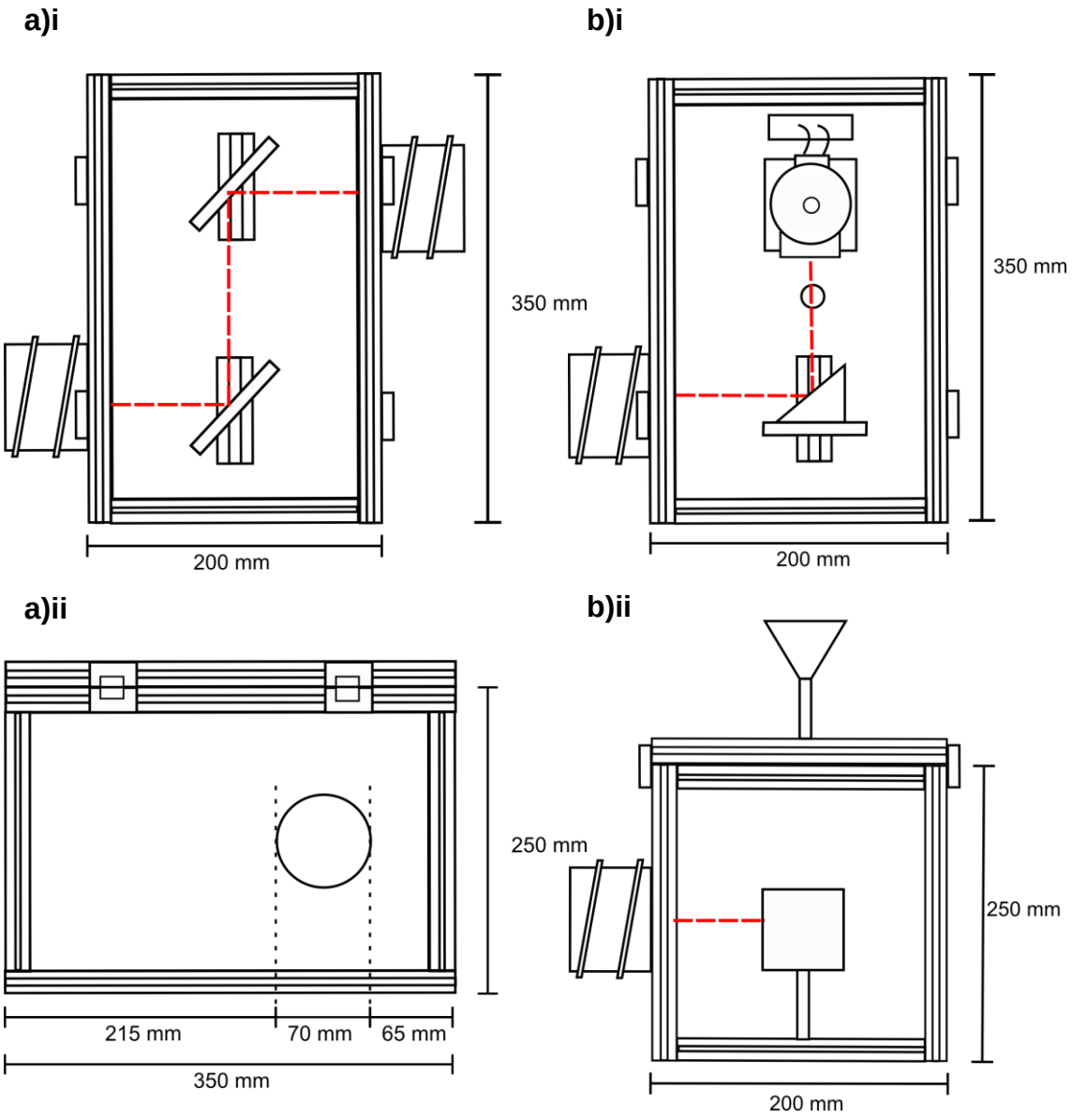

Figure 2.4: Top (i) and side views (ii) of the purge box (a) and detector purge box (b) designs that house the external mirrors used to reroute the IR beam through the UHV chamber.

2.2.3 Use of a grazing angle

The port positions for the reflected IR beam path described in section 2.2 were specifically chosen to provide the highest angle of incidence possible (for grazing angle FTIR spectroscopy), with mirror manipulation allowing for calculated angles of incidence to the sample greater than 75° (typically 78° was achieved). This is advantageous because for a beam perpendicular to the sample surface the phase shift in the incident and reflection vectors approaches 180º so that they cancel each other out *via* destructive interference; this means that minimal absorption is observable. At increasing angles of incidence, changes in the phase shift lead to a sizeable electric vector perpendicular to the sample surface approaching maximum observable absorbance at an angle of incidence of 88° [*Poling*, 1970]. This is also advantageous because at larger angles of incidence the effective path length through the sample is increased and a double pass through the sample occurs. Thus, in accordance with Beer's law of absorbance, the absorption is enhanced resulting in a strengthening of the difference between background and sample signal and therefore further improving the signal-to-noise ratio.

2.2.4 Testing the RAIRS system

Initial tests of the RAIRS system simply looked at improving and achieving the highest possible signal-to-noise through the UHV chamber. Experiments in which background and sample scans were taken sequentially under unchanged substrate conditions (115 K and 3×10^{-9} mbar) but at varying signal amplitude were undertaken. This was achieved by partial misalignment of the IR beam producing a less than optimal interferogram, in

order to evaluate background drift in the signal with changing amplitude. All spectra shown were taken at a base temperature of approximately 115 K due to the lower thermal conductivity of the stainless steel compared to Cu. The interferogram is the raw sample signal collected by the spectrometer before it is converted to an IR spectrum by Fast Fourier Transform (FFT) analysis. These comprised 560 accumulations of background spectra, followed by 560 accumulations of sample spectra (10 minute scans). An example of these initial tests is shown in Figure 2.5. Scans across different signal ranges illustrate that increased signal amplitude leads to reduced noise and highlights the deviation from a zero background at lower signal amplitudes. This curvature of the IR profile can be caused by slight changes in the experimental setup and variability in the IR detector. The effect of spectra curvature is reduced by increasing the signal amplitude and therefore optimizing the interferogram. It is clear that noise from background spectral features dominates in some regions, such as variability in the O-H stretch of H_2O at wavelengths above 3000 cm^{-1}. It should be noted that the absorbance in this study is shown in terms of $\log_{10}(\Delta R/R_0)$, the ratio of change caused by the sample (ΔR) from the background (R_0) instead of simply absorbance units (AU). This is because in the case of FTIR a single beam spectrum is obtained, meaning the background has to be taken separately to the sample (under the same orientation, temperature and pressure conditions) before being recombined, effectively producing a fractional sample absorbance relative to the background.

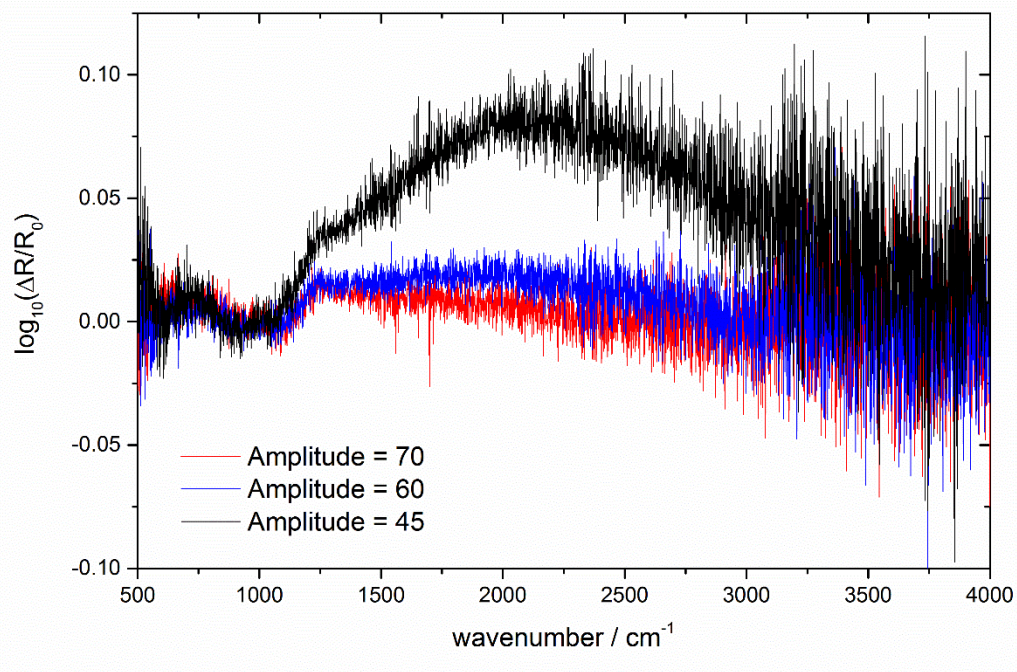

Figure 2.5: A plot of absorbance against wavenumber illustrating the effect of increased signal amplitude on background drift in the measured absorbance for the mid-IR wavenumber range of the Bruker IFS 66/S instrument. Profiles are aligned to highlight the relative shift in absorbance profile across the mid-IR.

2.2.5 RAIRS spectra of Benzene on Fe_2SiO_4

In order to test the capabilities of the newly constructed RAIRS system to measure absorbance, IR spectra were taken to evaluate the characteristic IR absorption band positions for thin films of benzene.

The UHV system at the time was being used to study acetylene uptake and reactivity to form benzene, with relevance to atmospheric uptake on meteoric particles and reaction processes occurring within the atmosphere of Saturn's moon Titan. Cu is known to react with acetylene and could form explosive compounds such as Copper acetylide. Therefore to ensure the safety of the UHV system, the Cu(111) substrate was replaced for this particular study with a stainless steel disc of the same dimensions. This was

coated in a layer of a cosmic dust analogue in the form of amorphous fayalite (Fe_2SiO_4) [*Saunders and Plane*, 2006] to simulate uptake on a particle in Titans atmosphere. A rough surface created by Fe_2SiO_4 particles (particle radii up to hundreds of nm) increases the fraction of scattered light through diffuse reflection and reduces the specular reflected light, thus reducing the signal at the detector from the substrate (compared to the Cu substrate). The high surface roughness will also impact the sample absorbance for lower surface coverages of benzene due to shadowing effects by the Fe_2SiO_4 particles, essentially reducing the intensity of IR that reaches the benzene molecules on the surface.

Benzene (calibrated using the same beam flux procedures detailed in Chapter 3) was dosed for a range of timescales to produce a range of film thicknesses (1×10^{16} – 1×10^{18} molecules) at 115 K on to the steel/Fe_2SiO_4 substrate in the form of a collimated beam *via* the needle valve on level C of the UHV chamber. The sample was then lowered to level A and aligned with the IR beam to optimize the interferogram and achieve the largest signal amplitude possible (~80). 1560 IR spectra (taking ~30 minutes) were accumulated for the background (prior to dosing), and also for sample scans. Typical spectra were recorded at 2 cm^{-1} resolution using an 8 mm beam width across a scan range of 400 - 4000 cm^{-1}. IR spectra from these experiments are shown in Figure 2.6, with each peak shown from the thinnest benzene layer where the peak was observed up to a coverage of 1×10^{18} molecules. A shift to lower frequencies is observed for the C-H out-of-plane bend (4 cm^{-1}) when reducing the benzene layer thickness and therefore moving towards the monolayer regime. A smaller shift of the same trend is observed for the C-C aromatic stretch on the order of 1 cm^{-1}. This

trend of shifting peak with decreasing benzene thickness is not observed for the C-H in-plane bend, however the smallest coverage it was observed at was still well in the multilayer regime at 3×10^{17} molecules. This peak shift could relate to the different binding sites of the benzene onto Fe_2SiO_4 (monolayer adsorption) vs benzene adsorbing onto other benzene molecules (multilayer adsorption). Peak shifting for the C-H out-of-plane and in-plane bend relating to surface coverage is consistent with the findings of *Thrower* [2009] for benzene adsorbed on amorphous silica. The absorbance of the C-H out-of-plane bend also drops off when approaching the lowest coverages, which may be explained by the shadowing effect of the rough Fe_2SiO_4 surface. Given that a benzene molecule is ~0.5 nm in diameter and the Fe_2SiO_4 particles can be 2 magnitudes larger in size, it would be plausible that the effects of the surface could impact the absorbance even for thicker benzene layers.

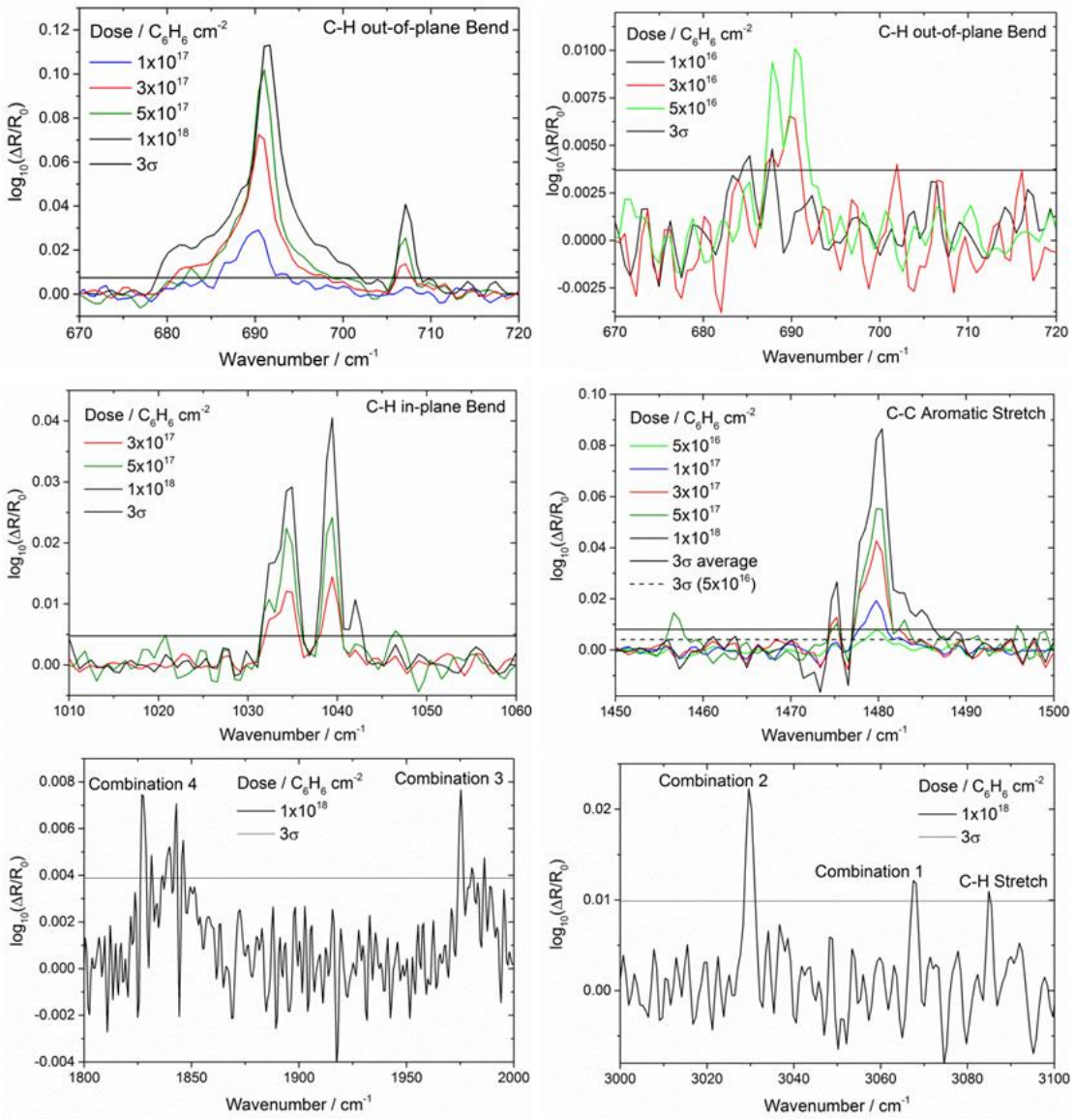

Figure 2.6: IR absorbance spectra taken for a range of benzene coverages illustrating the peak positions for the different vibrational modes of benzene. High and low dose plots are included for the C-H out of plane bend of benzene, in order to show the detection limit of the instrument.

Band assignments for the vibrational modes of benzene based on the multilayer benzene absorbance peaks observed in Figure 2.6 were made in accordance with previous literature and are shown in Table 1. The best agreement in peak assignment occurs when comparing to the study of benzene on amorphous SiO_2 from *Thrower* [2009] with peak assignment

agreeing on average within 3 cm^{-1}. Reasonable agreement is also observed when comparing to the study on an Si(111) crystal [*Strazzulla et al.*, 1991]. However, comparing to the study on Al by *Ruiterkamp et al.* [2005],disagreement in peak assignment is on average 9.5 cm^{-1} and as high as 18 cm^{-1} for the weakly absorbing combination bands. These discrepancies may relate to the specific methodology of the study, or effects of the substrate altering the absorbance peaks.

Table 1: Assignments of vibrational modes for the IR peaks of benzene observed in this study for amorphous Fe_2SiO_4 on stainless steel. Literature values are also included from studies on Al from *Ruiterkamp et al.* [2005], on amorphous SiO_2 from *Thrower* [2009] and from a Si(111) crystal from *Strazzulla et al.* [1991]. All frequencies are in cm^{-1} and mode numbers are included in brackets.

Peak assignment	RAIRS on Fe_2SiO_4 (this study)	Transmission IR on Si(111) [Strazzulla & Baratta, 1991]	RAIRS on Al [Ruiterkamp et al., 2005]	RAIRS on SiO_2 [Thrower, 2009]
C-H out-of-plane bend (v_4)	691	688	678	690
C-H in-plane bend (v_{14})	1039	1040	1038	1037
C-C aromatic stretch (v_{13})	1480	1480	1481	1477
Combination 4 (v_{18}+v_{19})	1828	1836	1812	1832
Combination 3 (v_{11}+v_{19})	1975	1980	1957	1973
Combination 2 (v_{13}+v_{16})	3030	3036	3043	3027
Combination 1 (v_2+v_{16}+v_{18})	3068	-	3075	3065
C-H stretch (v_{12})	3085	3088	3095	3082

Detection limits under the conditions of this study were based on a 3σ evaluation of the background noise of spectra in Figure 2.6 and varied depending on the wavenumber range and benzene film thickness. The detection limits across the mid-IR range studied (500 – 4000 cm^{-1}) varied

from $\log_{10}(\Delta R/R_0) = \pm 0.0025$ up to ± 0.01 in noisier regions more affected by background fluctuations, such as the O-H stretch region of H_2O (> 3000 cm^{-1}). This meant that the strongest absorbing band of benzene in this case (C-H out of plane bend) was detectable at surface coverages of $\geq 1 \times 10^{16}$ molecules. Using a resolution of 1 cm^{-1} did not yield further peak information and actually reduced the signal observed, due to the need for a smaller beam aperture giving reduced beam intensity at the detector.

It should be noted that further improvements to the system have taken place since these initial test spectra of benzene were taken. The system now achieves signal amplitudes in the region of 200 (previously 70) and noise of $\log_{10}(\Delta R/R_0) = \pm 0.001$. This was achieved by switching back to the more reflective Cu(111) substrate, the introduction of a concave mirror with a more appropriate focal length and further improvements to the grazing angle achieved through the sample. This focuses more of the IR beam on to the substrate, leading in turn to more light passing through the sample and reaching the detector. Therefore, the detection limits shown in the benzene spectra are an upper limit.

2.3 TRAPS/MICE apparatus

In order to investigate the nucleation of CO_2 ice on nanoparticles and provide insight into the nucleation kinetics of CO_2 in the Martian mesosphere, a specialized experimental system was required. The experiment in its entirety is called the TRAPS and comprises two key components described in this section: a microwave plasma NanoParticle Source (NPS), and a Molecular flow Ice CEll (MICE). The results using this system are detailed in Chapter 5.

2.3.1 Why use MICE?

The study of suspended particles exposed to saturated environments has been typically studied using diffusion chambers [*Langsdorf*, 1939]. A current example of such systems, referred to as Continuous Flow Diffusion Chambers (CFDCs), is often used for the study of H_2O ice nucleation with application to tropospheric ice clouds on Earth [*Salam et al.*, 2006]. CFDCs operate at much higher temperatures (> 190 K) and pressures (500 – 1000 mbar) and typically much lower saturations (S = 1- 2) than the conditions observed for CO_2 nucleation in the mesosphere of Mars [*Gonzalez-Galindo et al.*, 2011; *Listowski et al.*, 2014; *Rogers et al.*, 2001]. The instruments comprise a cold and warm plate coated in ice in a parallel orientation (they can also be used in other geometries such as cylinders). When heat and vapour is transported from the warm to cold plate via diffusion, linear gradients of temperature and vapour concentration are created in the space between the plates but this leads to a nonlinear saturation profile.

In the case of the MICE apparatus the system is run at much lower pressures than a diffusion chamber (10^{-3} mbar). At these low pressures diffusion does not determine the saturation profile (continuum regime). This is because at low pressure the MICE operates in a free molecular flow regime, where the mean free path of the CO_2 in the gas phase is larger than the distance between the plates. This is similar to the principles of gas-surface interactions discussed for UHV chambers in subsection 2.1.1. The gas particles retain their Maxwell-Boltzmann distribution relating to the temperature of the wall they were released from, which produces a more linear saturation profile between the plates, and also enables higher saturation conditions to be achieved [*Duft et al.*, 2015]. This low pressure (10^{-3} mbar), high saturation environment (S = ~1000) in the molecular flow regime produced in the MICE within the TRAPS apparatus is crucial for producing reproducible conditions close to the mesospheric CO_2 clouds seen on Mars.

The TRAPS system encompassing the MICE has previously been used to study currently unpublished work on water ice growth on MSP analogues applicable to the Earth's mesosphere [*Nachbar et al.*, 2016a]. For the work in this thesis it was used to study CO_2 ice growth under conditions applicable to the Martian mesosphere. As indicated in the contributions section, the MICE was developed and implemented primarily by Dr Denis Duft and Mario Nachbar [*Duft et al.*, 2015]. The TRAPS system including the NPS was initially designed by *Meinen et al.* [2010].

2.3.2 The TRAPS system

The NPS shown in Figure 2.7 produces nanoparticles which can be seen as analogous to particles of meteoric origin of which SiO_2 (ρ = 2.3 g cm^{-3}) and Fe_xO_y (ρ = 5.2 g cm^{-3}) are produced. Solid ferrocene ($Fe(C_5H_5)_2$) is used as a precursor source of Fe atoms when producing Fe_xO_y and in the case of SiO_2 nanoparticles liquid tetraethyl orthosilicate ($C_8H_{20}O_4Si$) is used as a Si precursor. The precursors are heated and introduced as a vapour into a flow tube system. These precursor species are mixed with a flow of primarily He (3 standard litres per minute (slm)) and passed through a microwave resonator creating a plasma (total pressure of 60 mbar) where the precursors are dissociated. An additional 0.3 slm upstream flow of He (80%) and O_2 (20%) is introduced, causing oxidation of the metastable excited Fe or Si atoms in the microwave reactor and subsequent particle formation (particle radii <4 nm under these conditions). Nanoparticles produced in comparable experimental systems were shown to be compact, spherical and singly charged and so are assumed to be in this study [*Giesen et al.*, 2005].

The complete schematic diagram of the TRAPS system in Figure 2.8 shows where the charged nanoparticles are introduced to the system. The nanoparticles are transferred to a low pressure environment and constrained into a beam through the use of a flow-limiting orifice (FLO) and an aerodynamic lens (ADL). The charged particles are guided by a quadrupole deflector with charged electrodes to deflect the particles around the 90° bends of the system. The voltage at these electrodes can be manipulated to mass select the size of particle of interest that enters the MICE quadrupole ion trap. Radio frequency potentials higher than the kinetic energy of the

particles at U_{in} and U_{out} are used to contain 10^7 - 10^8 particles. A He background gas is used to slow the particles *via* collisions to avoid particle loss during filling (during which U_{in} is opened).

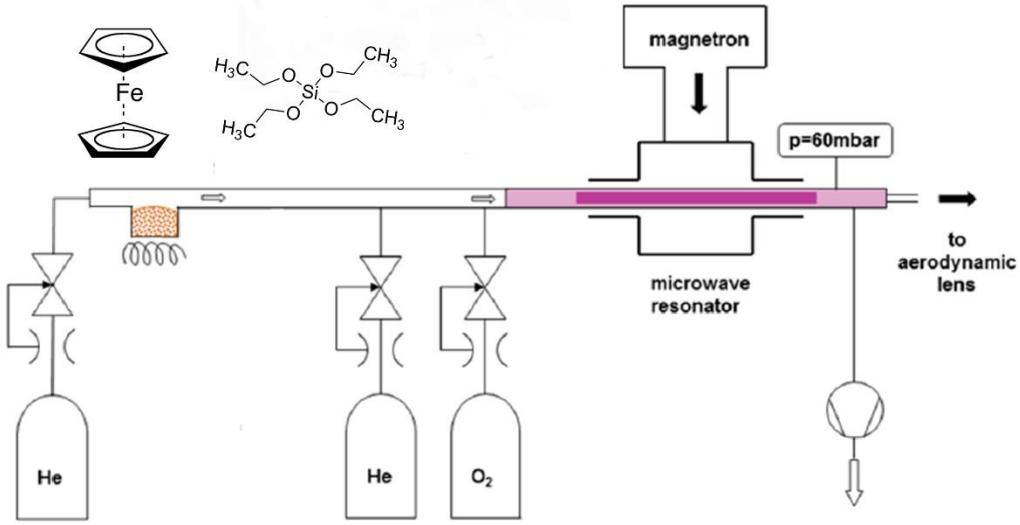

Figure 2.7: Schematic diagram of the NPS within the TRAPS apparatus for production of SiO_2 and Fe_xO_y particles. Adapted from *Nachbar* [pers comms, 2014].

The MICE system in which the particles are trapped comprises a copper tube (the “cold” wall) on which four copper quadrupole rods are connected with high thermal conductivity spacers (SHAPAL, Tokuyama Corp.) which account for 75% of the surface area inside the chamber. The cooling tube (and therefore the quadrupole rods) is connected to a He gas cryostat (DE-104B-Turbo, Advanced Research Systems Inc.) with a temperature range of 25 – 300 K. Between the cold wall and the quadrupole rods (and covering the space between the rods) is a gold plated copper tube that acts as a “warm” wall, connected with low thermal conductivity spacers (PEEK, Victrex plc.) and accounts for the remaining 25% of the surface area within the chamber. This warm wall is heated by two heating foils that are positioned to

minimise temperature gradients across the MICE. The temperature is measured using five Pt-100 probes embedded within the length of the cell. The warm wall surfaces are saturated (at the example base temperatures given) with CO_2 producing an ice layer with a typical thickness in the region of 20 - 50 µm. The CO_2 ice is deposited onto the warm walls of the chamber using CO_2 vapour passed through a hole-filled steel tube that is inserted into the centre of the MICE. *Via* surface heating and cooling of the MICE system, the CO_2 vapour concentration (by sublimation of the CO_2 ice on the walls) and particle temperature can be manipulated until CO_2 ice nucleation conditions are reached. The low pressure on the order of 10^{-3} mbar when entering the MICE is achieved by a rotary pump and the FLO. The geometry of the system enables homogeneous saturation and temperature conditions in the central region of the chamber (7 mm radius) with in which the particle beam is contained (1 mm radius). As noted in subsection 2.3.1, supersaturation under free molecular flow condition reaches higher values and extends over a larger volume than in the diffusive case. Unfortunately due to rapid sublimation of CO_2 from the surfaces of the MICE at particle temperatures above 75 K, studies of ice growth and nucleation were limited to CO_2 concentrations and temperatures slightly below that of the Martian mesosphere. A slight temperature gradient across the MICE of 0.1 K gives a particle temperature uncertainty of 0.4 K and an uncertainty in CO_2 concentration of approximately 10%.

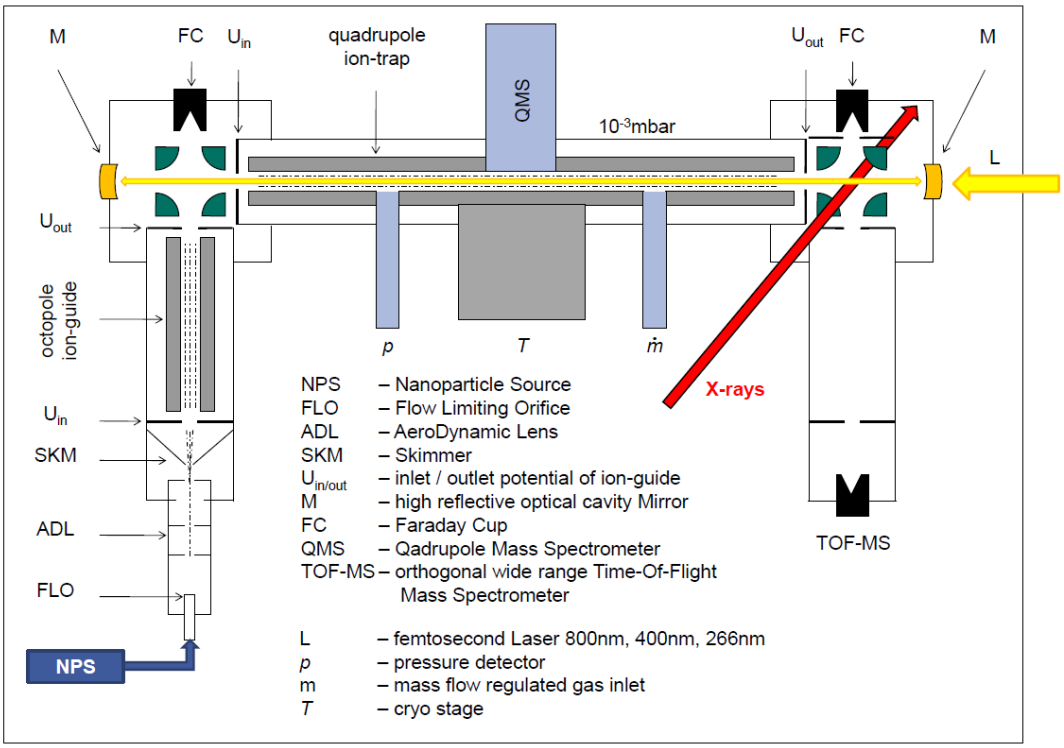

Figure 2.8: Schematic diagram of the TRAPS system. The inflow of particles from the nanoparticle source is indicated in the bottom left of the diagram, while the MICE apparatus is the name for the quadrupole ion trap. In the experiments detailed in this thesis the Laser and X-ray based analysis shown was not possible. Reproduced from *Nachbar* [pers comms, 2014].

Using a series of delayed pulses, particles are ejected from the MICE (~10^5 particles per pulse) and subsequently detected by a home-built Time-Of-Flight Mass Spectrometer (TOF-MS). This allows for the growth of CO_2 ice on the nanoparticles to be evaluated using the time-resolved particle size determination of which the specific methods for a typical experiment and results for CO_2 ice nucleation are described in Chapter 5.

2.4 Environmental XRD chamber

The CO_2 ice crystal structure under conditions relevant to the mesosphere of Mars was determined using a temperature-controlled stage enclosed within an environmental chamber equipped with an x-ray diffractometer. This chamber has previously been used to investigate the properties of H_2O ice [*Malkin et al.*, 2012; *Malkin et al.*, 2015; *Murray et al.*, 2015]. The instrumental setup is detailed below, while results using this instrument and the specific experimental methods are described in Chapter 6.

2.4.1 Why use XRD?

XRD is an extremely useful technique for measurements of crystal structure. This is mainly due to its ability to act as a non-destructive in situ analysis technique for determining the phase and orientation of crystalline ice films. Being able to probe with X-rays a surface that is exposed to Martian mesospheric temperature and pressure conditions through the use of an environmental chamber is advantageous for the study detailed here. The crystallographic structure of a solid can be determined using X-rays through the application of Bragg's law.

A crystal consists of an arrangement of the unit cell (the smallest volume that contains the repeating structure) into a lattice. Crystals are grouped into different three-dimensional lattice systems, of which cubic is of particular interest for low-temperature and low-pressure CO_2 ice formation. Crystallographic directions are lines linking atoms or molecules of a crystal in a particular direction within the unit cell, while crystallographic planes are planes linking these lines. Miller indices (*hkl*) indicate the three-dimensional

orientation of the surface of a crystallographic plane depending on how it inversely intercepts the vectors of the lattice. These planes of atoms within a crystal are spaced a distance *d* (Å) apart and can be resolved into several atomic planes within a crystal, each with a different *d* spacing. Bragg's law provides the angles for coherent and incoherent scattering by X-rays from planes within a crystal lattice which quantitatively determine this *d* spacing in relation to 2θ angle. This relation is shown by:

$$2d_{hkl} \sin\theta = n\lambda \tag{2.1}$$

where λ is the wavelength of the incident X-ray beam and *n* is an integer. Two beams with identical λ and phase approach a crystalline solid and are scattered off two different atoms within it as shown in Figure 2.9. X-rays scattered from parallel planes will combine constructively (constructive interference), when the θ between the plane and the X-ray results in a path-length difference that is a multiple of *n* and of the X-ray λ (meaning they remain in phase). Bragg's law describes the situation for the strongest constructive interference, shown as defined sharp Bragg peaks in an XRD pattern. The angle of this peak is a product of the average *d* in the crystal. Periodically repeating systems such as crystals have a Fourier transform repeating at specific points in reciprocal space which gives rise to the specific angles of Bragg peaks increasing in intensity depending on the number of scattering planes. The produced peaks in spectra from X-ray diffraction can then be fitted to a hypothesised crystal structure and analysed to determine the specific crystal parameters of the sample [*Rietveld*, 1969]. The specific methods employed for this pattern fitting are discussed in more detail in Chapter 6.

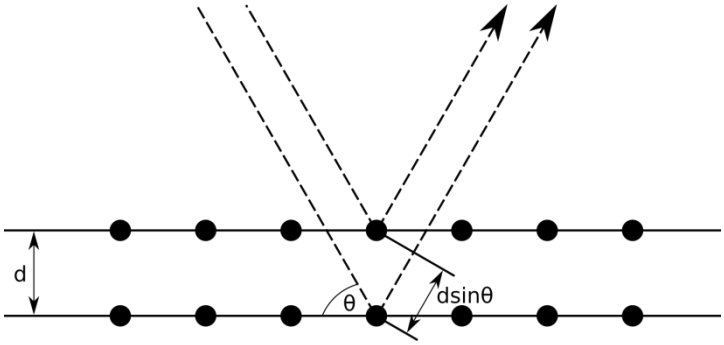

Figure 2.9: Illustration of Bragg diffraction for a crystal plane, two X-ray beams of identical λ are scattered by two different atoms within a crystal, the difference in the distance travelled by the lower beam equalling $2d \sin \theta$.

2.4.2 The XRD system

The X-Ray diffractometer (Bruker D8 Advance) was configured in a standard reflectance geometry and equipped with a Cu Kα X-ray source (λ=1.540598 Å). This system does not have a monochromator, which means that the Kα-1 (λ=1.5406 Å), Kα-2 (λ=1.5444 Å) and Kβ (λ=1.3922 Å) emissions are not filtered out and can reach the sample. Any unwanted peaks related to Kβ emissions are normally within signal noise, but can be accounted for in subsequent analysis. Diffracted X-rays from a sample mounted on an Anton Paar TTK 450 temperature-controlled stage were detected by a VÅNTEC detector (shown in Figure 2.10). The use of Kapton-film windows sealed with O-rings allowed for the transmission of X-rays in and out of the environmental chamber. The air-tight chamber was pumped by using a Pfeiffer Duo 2.5A vacuum pump allowing a pressure range of $1x10^{-3}$ - $1x10^{3}$ mbar. This stage was cooled with liquid nitrogen pumped using a Thomas VTE 6 vacuum pump and the temperature was controlled using a Eurotherm PID controller and resistive heaters. The sample support could be cooled to

a stable temperature from ambient to 80 ± 0.2 K. During experiments this temperature was maintainable at pressures below 10 mbar. Under higher pressures and therefore higher gas inflows, the substrate temperature became unstable due to heating from the chamber gas and a deviation from equilibrium conditions. The sample support was constructed from aluminium, covered with a borosilicate glass slide (160 µm thickness), and adhered to the aluminium support using a thin layer of vacuum grease. The temperature was measured using a Pt-100 probe directly inserted into the sample support. Heat conducting grease was used to maximise thermal contact between the probe and the sample support, as well as between the sample support and the cold stage, thus minimising temperature measurement error and maximising cooling and heating efficiency.

This stage is probed using the powder X-ray diffraction (XRD) technique of which the principles are detailed in subsection 2.4.1. In the experiments described in Chapter 6, CO_2 gas was either vapour-deposited onto a flat substrate, or CO_2 in the form of powdered dry ice was placed in a sample holder and inserted into the chamber before XRD analysis.

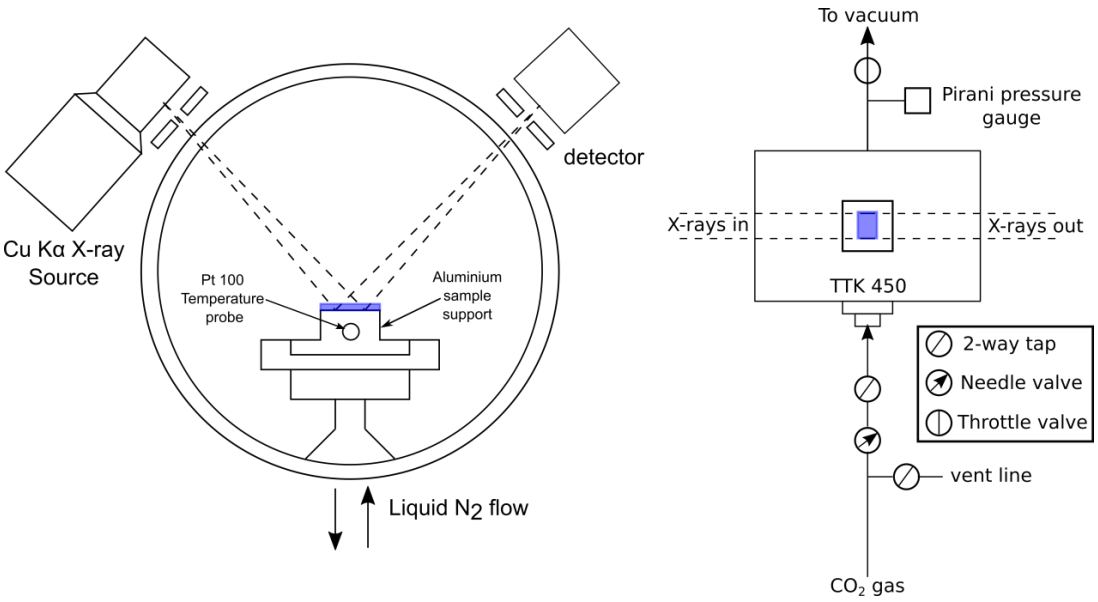

Figure 2.10: Schematic diagrams of the front view of the TTK 450 temperature controlled stage (left) and top down view of the experimental system (right). The position of the CO_2 ice sample is indicated by the blue rectangle (not drawn to scale).

3 CO_2 trapping in amorphous H_2O ice: Relevance to polar mesospheric cloud particles

CO_2 is subject to uniform vertical mixing from the surface up to altitudes at which PMCs can form, leading to a large CO_2:H_2O ratio in the mesosphere (>37:1) compared to the lower atmosphere (>0.01:1) [*Emmert et al.*, 2012; *Rong et al.*, 2010]. This opens the question as to whether CO_2 could become trapped within, and affect the properties of, PMC ice particles. Previously, CO_2 has been trapped experimentally in ASW for application to the ISM, on comets and icy satellites, where H_2O/CO_2 ice interactions are thought to be prevalent, but not under atmospherically relevant concentrations of CO_2 and H_2O [*Galvez et al.*, 2008; *Hodyss et al.*, 2008b; *Mate et al.*, 2008]. This chapter describes TPD experiments undertaken in an UHV chamber to evaluate whether CO_2 could become trapped in PMC ice particles. Beam flux calibrations were used to quantify the flux of CO_2 and H_2O to the sample surface. CO_2:H_2O gas mixtures were used to form ice layers that contained trapped CO_2 in the ice matrix at ratios of 1:1 - 12:1. Due to the presence of a sufficient CO_2 flux, CO_2 trapping in ASW was evaluated in terms of a limiting experimental H_2O flux (4.8×10^{13} molecules cm^{-2} s^{-1}) at conditions above a 12:1 ratio and compared to atmospheric conditions. This comparison suggests that in a saturated H_2O environment during PMC season (10 ppmv of H_2O), CO_2 trapping would only be plausible under extreme temperatures below 100 K.

3.1 Methodology

In this section, the techniques and procedures that were used to produce and analyse thin ice films using gas mixtures of CO_2 and H_2O are described. The methods described within this chapter use the UHV chamber apparatus and associated instruments described in detail in Chapter 2. The results of experiments performed using these methods are detailed in section 3.3, while the preparation and dosing of the gases is also relevant for the methods employed for the beam flux calibrations in section 3.2.

3.1.1 CO_2:H_2O gas bulb mixtures

In order to purify H_2O for use in gas mixtures of varying CO_2:H_2O ratio the freeze pump thaw method was employed. On a glass gas-handling line a sample of deionised water was attached. Liquid N_2 was used to freeze the H_2O which was subsequently exposed to the vacuum. The line was then left to reach base pressure as degasification of the H_2O took place, while maintaining minimal H_2O vapour release from the solid. Once the pressure began to rise (indicating the H_2O ice had started to melt), the sample was isolated from the glass gas-handling line, the ice melted and the whole freeze pump thaw process repeated (3 times). The line was then flushed with the H_2O vapour twice before the gas bulb was filled. The CO_2 was introduced to the gas line as dry ice, and pumped on several times to remove impurities. The line was then flushed with CO_2 and the bulb filled. In the case of the experiments described in section 3.3, gas bulbs of varying CO_2:H_2O ratio were prepared *via* manometric techniques, of which the lower vapour pressure H_2O was always introduced first, before filling with the higher pressure CO_2.

3.1.2 Sample preparation and CO_2:H_2O gas dosing

Prior to dosing, the Cu(111) crystal sample within the UHV chamber was annealed to 800 K for 30 minutes via resistive heating, in order to clean the crystal surface. Once the sample temperature had reduced, the cold finger was filled with liquid N_2 to decrease the sample temperature to a stable base reading of approximately 98 K. The base temperature was maintained throughout the experiment by refilling the cold finger at regular intervals.

The sample was oriented to face the needle valve (X = 10 mm, Y = 13 mm, Z = 170 mm, θ = 330°) for dosing of the CO_2/H_2O gas mixture with the Hiden QMS set to measure the species of interest (in this case (where m is in g) m/z = 18 (H_2O) and 44(CO_2)). The required glass gas-handling line pressure of the gases corresponded to a specific beam flux (calculated in subsection 3.2.2) and was typically 15 torr. Once all mass traces were stable, the dose was started by opening the needle valve (NUPRO, SS4BK), which produced a collimated diffusive beam targeted at the Cu(111) crystal. Once the dose time was complete (typically 2 hours), the needle valve was closed, at which point TPD analysis could be undertaken. An example dose from a typical experiment is shown in Figure 3.1, and effectively shows the detected CO_2 and H_2O that was not adsorbed onto the Cu(111) sample.

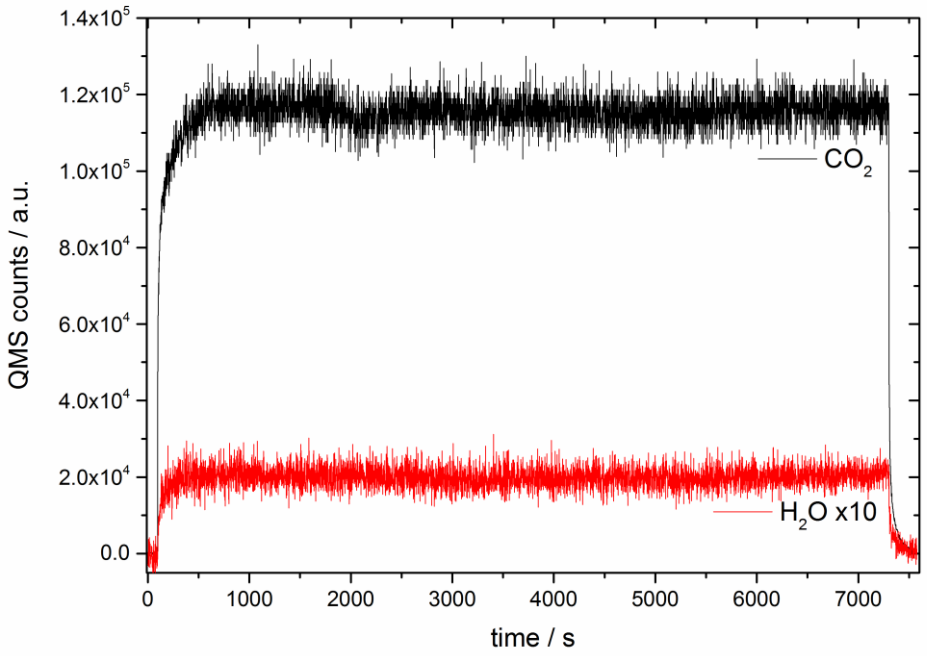

Figure 3.1: Example mass spectrometer trace of CO_2 and H_2O (x10 for clarity) during a two hour dose onto the Cu(111) sample at 98 K for a CO_2:H_2O ratio of 6:1.

3.1.3 Temperature programmed desorption

Once the background QMS mass counts had stabilised after a gas dose, a TPD experiment could be undertaken to analyse the composition of the thin ice film produced. The sample was repositioned to face the QMS (X = 10, Y = 13, Z = 175, θ = 170°) in order to maximise the signal from species desorbing from the Cu(111) crystal. The QMS was set to monitor relevant mass traces and also recorded the temperature relayed from the K-type thermocouple embedded in the sample. Resistive heating was then applied by setting a specific voltage that produced a linear heating ramp of 0.25 K s^{-1} across the temperature range of interest (98 – 200 K). Results from experiments using this TPD procedure on thin CO_2 and ASW films are shown in section 3.3.

3.2 Beam flux calibrations

In order to carry out the experiments detailed in section 3.3 it was necessary to calibrate the beam flux, F_{beam}, of the UHV chambers' collimated diffusive beam doser (NUPRO, SS4BK) for CO_2 and H_2O and evaluate a stable pressure range for the study. This provided a quantitative measure of the gas species used in the CO_2 trapping experiments detailed in section 3.3.

3.2.1 Theory

Pump-down beam flux calibrations were carried out based on theory from *Oakes* [1994] and are described below, modified for the experimental system used in this study. The pump-down beam flux calibrations assume that the number of molecules entering the chamber, F_{in}, is equal to the number of molecules leaving, F_{out}. F_{out} is derived from a time dependent version of the ideal gas equation and is shown in equation 1, where n is the number of molecules, P is the pressure, V_{system} is the volume of the UHV chamber, k_B the Boltzmann's constant and T is the temperature. The pump down curves of each species provide the change in gas pressure over time, dP/dt for that species.

$$\boldsymbol{F_{out}} = \frac{\boldsymbol{dn}}{\boldsymbol{dt}} = \frac{\boldsymbol{V_{system}}}{\boldsymbol{k_B T}} \frac{\boldsymbol{dP}}{\boldsymbol{dt}} \qquad (3.1)$$

The exponential decay of the gaseous species at the termination of the dose (the pump-down curve) is described in Equation 3.2 and is shown experimentally in Figure 3.2 where P_0 is the initial pressure, with C_m the pumping coefficient for the gas at mass m. This is differentiated at the initial time t_o, giving the initial pressure change (Equation 3.3). Substituting this into

Equation 3.1, given the previous assumption that F_{in} = F_{out}, as well as accounting for the cross sectional area of the beam (A_{beam}), yields the calculation of F_{beam} in units of molecules cm^{-2} s^{-1} (Equation 3.4). The values for F_{beam} are calculated using a similar experimental procedure to the one described in *Frankland* [2011] and are detailed in the following subsection.

$$\boldsymbol{P = P_0 e^{-C_m t}} \tag{3.2}$$

$$\left|\frac{dP}{dt}\right|_{t_0} = \boldsymbol{C_m P_0 e^{-C_m t_0} = C_m P_0 e^0 = C_m P_0} \tag{3.3}$$

$$\boldsymbol{F_{beam} = \frac{V_{system}}{k_B T}\left|\frac{dP}{dt}\right|_{t_0}\frac{1}{A_{beam}} = \frac{V_{system} C_m P_0}{k_B T A_{beam}}} \tag{3.4}$$

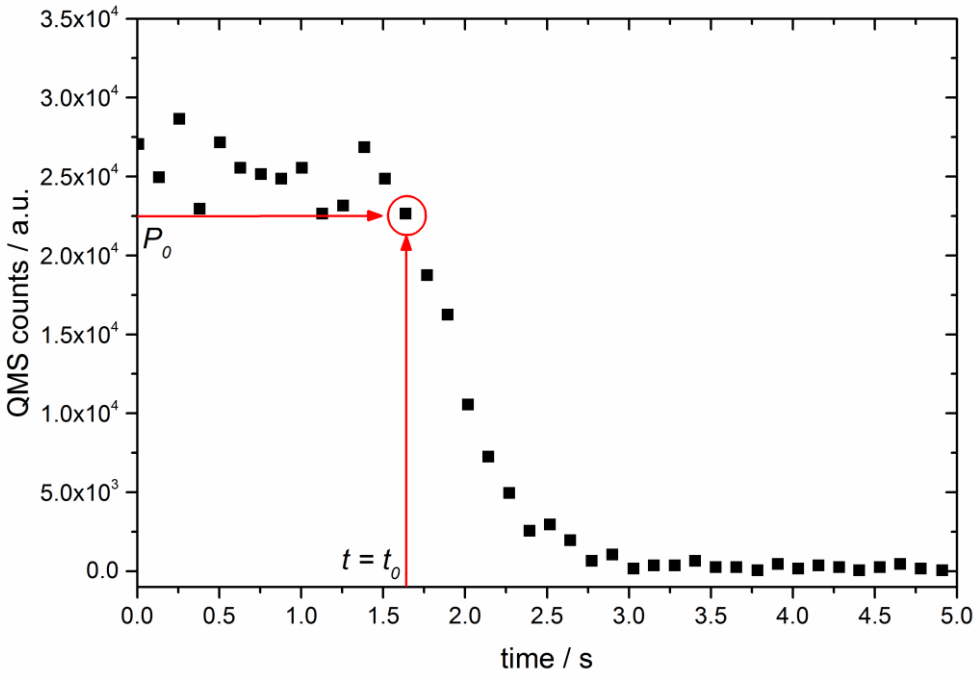

Figure 3.2: QMS counts (a.u) versus time (s) for an example CO_2 pump down curve highlighting the position of P_0 and t_0 at a dosing pressure of 5 torr.

3.2.2 Beam flux determination for CO_2 and H_2O

Sets of pump-down experiments were carried out for both H_2O and CO_2 in order to quantify both species in terms of pressure and F_{beam} within the UHV chamber. The pump-down experiments were performed under UHV conditions at base pressures in the range of 10^{-9} mbar. The gate valve between the turbo pump and UHV chamber was partially closed in order to throttle the pumping speed. This caused a slower signal decay and therefore provided greater time resolution (increased number of data points) for the pump down curve analysis. Pure gas mixtures were prepared in the vacuum gas line (see subsection 3.1.1 for method) with pressures in the bulb of 1 - 15 torr for H_2O and 5 - 16 torr for CO_2.

In order to limit the sample's effect on the dosing beam the sample was raised out of beam alignment (z = 200 mm) and kept at room temperature (approximately 295 K) throughout the experiments. H_2O and CO_2 doses were undertaken at 4 different gas bulb pressures and repeated a minimum of 3 times for each pressure. The QMS (Hiden, HAL 3F 301 RC PIC) measured the intensity of CO_2 and H_2O (masses m/z = 44 and 18, respectively) during each experiment (as detailed in subsection 3.1.2). In order to achieve a stable maximum value for H_2O intensity, a dose of 30 minutes was required with a 30 minute gap between doses to allow for the pressure within the chamber to return back to base levels (10^{-9} mbar). For CO_2, doses only required 2 minutes to achieve a stable intensity with only a 4 minute interval between doses. An example CO_2 pump down experiment is shown in Figure 3.3.

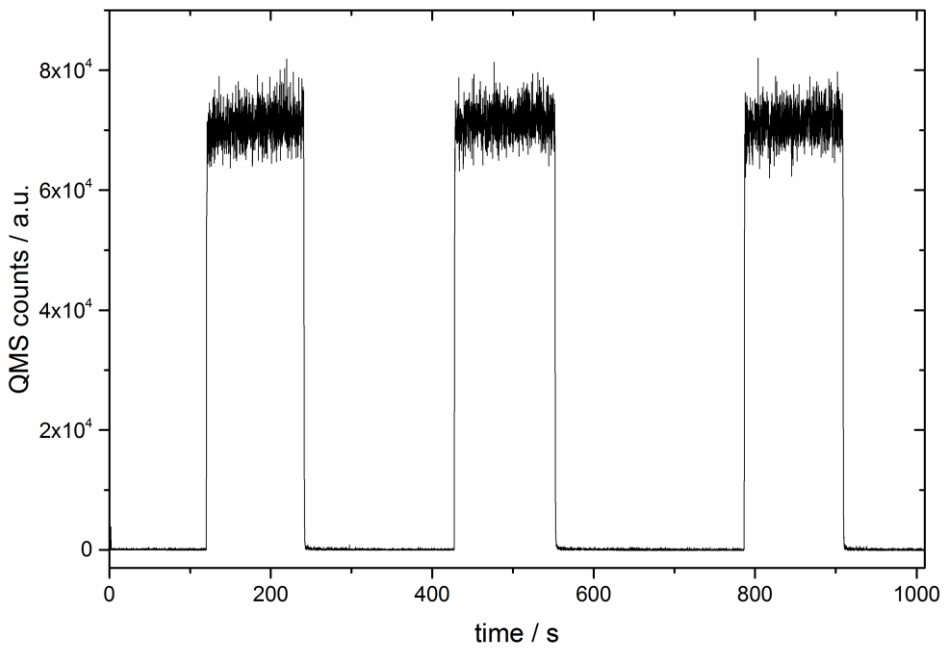

Figure 3.3: QMS counts (a.u.) versus Time (s) for repeats of CO_2 pump-down experiments undertaken at 12 torr.

Maximum QMS counts for each dose were averaged across a minimum of 300 data points and then repeat experiments were averaged at each pressure. The error was determined as the standard deviation of all the averaged doses at that pressure. A fit applied to the data shows a reasonable linear relationship between QMS counts and the gas bulb dosing pressure. Full profiles of both gas species are shown in Figure 3.4.

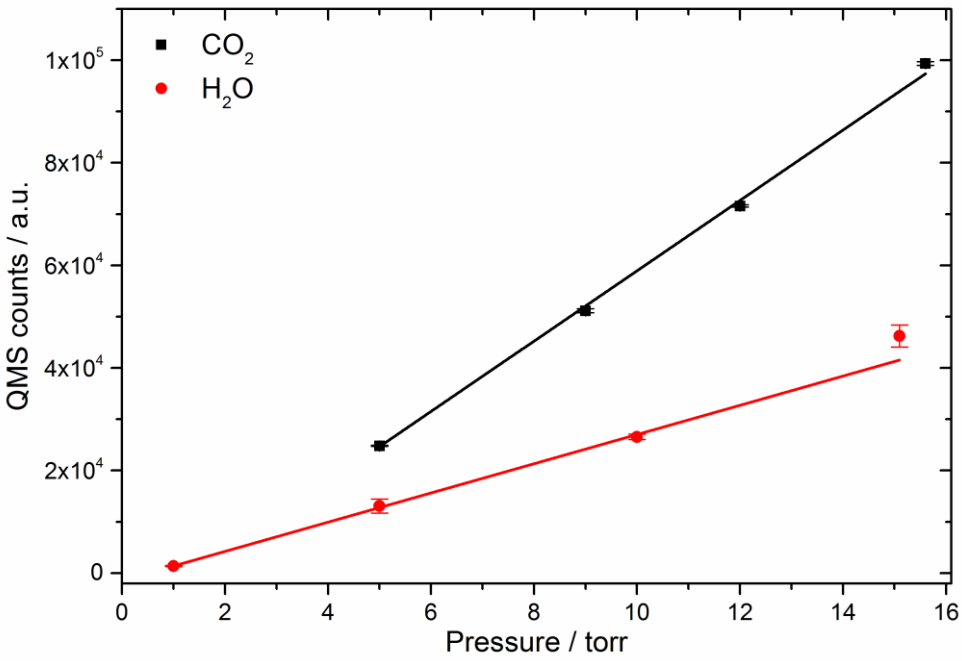

Figure 3.4: QMS counts (a.u.) versus dosing pressure (torr) for CO_2 and H_2O over a range of pressures.

In order to apply the QMS count profiles for CO_2 and H_2O from the pump-down experiments across the relevant pressure range and allow for the calculation of the F_{beam}, a conversion from QMS counts to Pascals was necessary *via* background calibration experiments. To enable these calculations, the ion sputter source (PSP vacuum, ISIS 3000) was modified and used as a leak valve for background dosing. H_2O and CO_2 at pressures in the range of $10^{-7} – 10^{-9}$ mbar were leaked into the chamber while QMS counts of the respective species were monitored using the QMS. Figure 3.5 displays the calibration graphs for H_2O and CO_2, with linear fits (showing good agreement) used to produce pressure calibration equations (equations 3.5 and 3.6, respectively). A conversion factor was applied to the calibrations so that pressure units were converted from mbar (the units of the UHV chambers ion pressure gauge) to Pascals.

$$H_2O\ (Pa) = \frac{H_2O\ (QMS\ counts) - 946.12}{4.35 \text{ x } 10^{11}} \text{ x } 100 \qquad (3.5)$$

$$CO_2\ (Pa) = \frac{CO_2\ (QMS\ counts) - 1143.94}{2.90 \text{ x } 10^{11}} \text{ x } 100 \qquad (3.6)$$

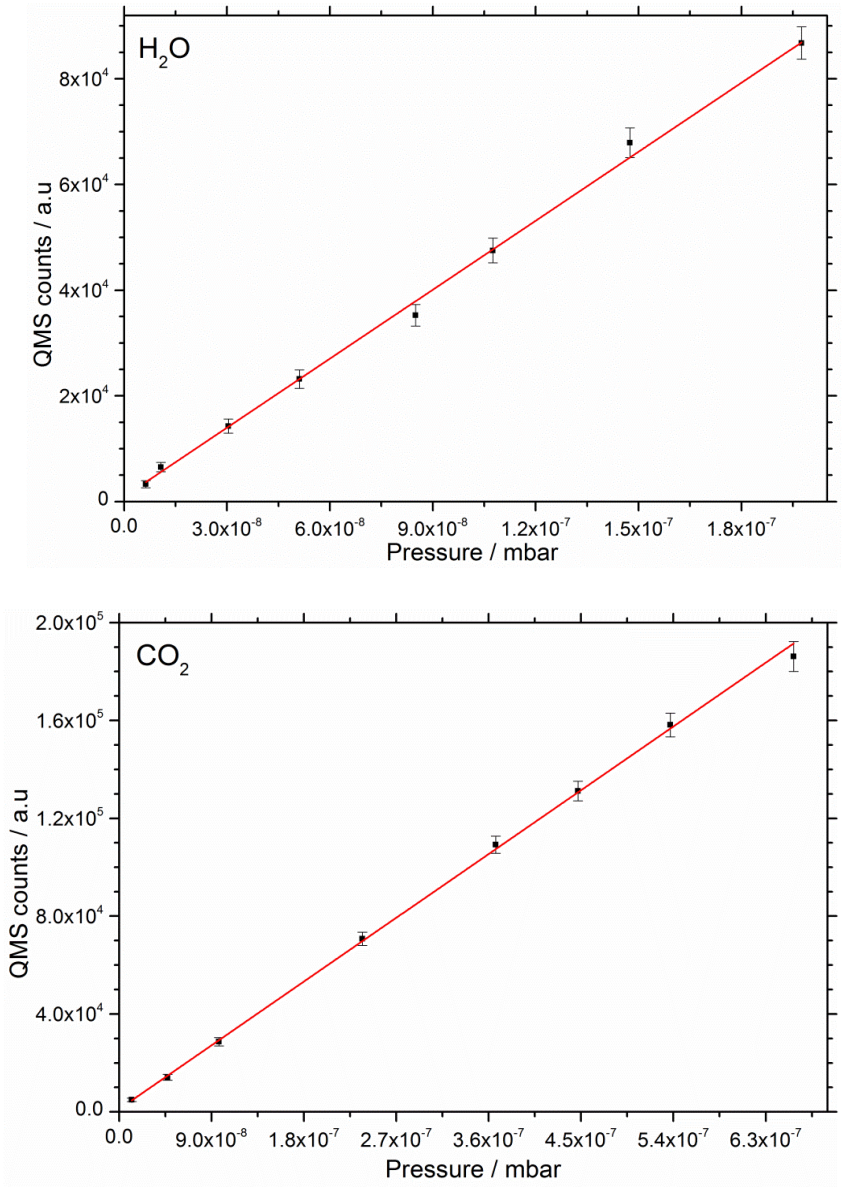

Figure 3.5: QMS counts (a.u.) versus chamber pressure (mbar) across a range of pressures for background doses of H_2O (top) and CO_2 (bottom).

The initial start of each pump-down experiment was isolated and the time corrected to start from zero (as previously shown in Figure 3.2). Plots of ln(*P*) against *t* for each experiment were constructed (an example plot is shown in Figure 3.6) and a linear fit applied. This is equal to a logarithmic version of equation 3.2 (shown in Equation 3.7). This fit was then used to calculate the values of P_0 and C_m for each species at each gas bulb pressure.

$$\ln(P) = -C_m t + \ln(P_0) \tag{3.7}$$

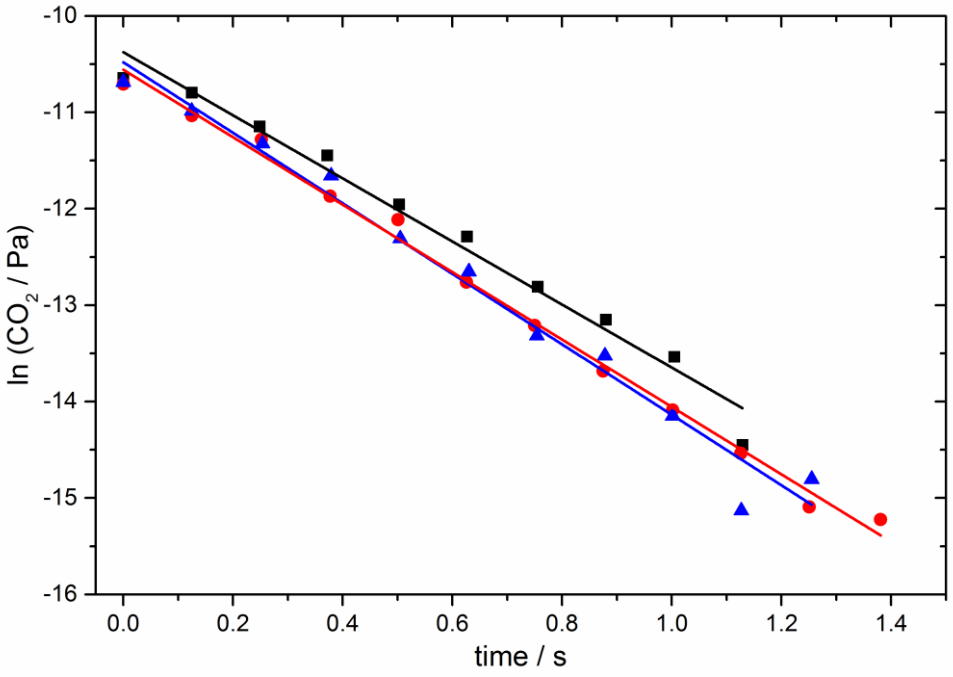

Figure 3.6: Examples of the natural logarithm of pressure (Pa) for three repeat pump-down curves for CO_2 at a dosing pressure of 12 torr.

The averaged values for P_0 and C_m at each gas bulb pressure are shown for H_2O and CO_2 in Table 2. The values of C_m should remain constant for each gas species as the mass of the beam species is unchanged. Values for H_2O in the gas bulb range of 5 – 15.1 torr are in good agreement with an average of 0.049 ± 0.007 s. However, an anomalous value is present at 1 torr

(0.24 s). This is probably due to low H_2O counts close to the noise of the QMS signal, combined with the pressure calibration including an intercept above zero (1000 counts). Values of C_m for CO_2 show good agreement across the pressure range studied with an average of 3.64 ± 0.1 s, although this did not include results obtained at a lower pressure of 1 torr which lead to the discrepancies in C_m values for H_2O.

F_{beam} was calculated using Equation 3.4 (with the reported C_m and P_0) where V_{system} is 0.025 m^3, A_{beam} is 1.13×10^{-4} m^2 and T was assumed as 300 K. Values of F_{beam} were averaged at each gas bulb pressure are shown in Table 2 as well as being plotted against dosing pressure in Figure 3.7. Fits to the data suggest the relationship between F_{beam} and dosing pressure for both species is approximately linear. These fits were used to produce an equation for determining F_{beam} (units of molecules cm^{-2} s^{-1}) for H_2O and CO_2 for a given dosing pressure (equations 3.8 and 3.9 respectively).

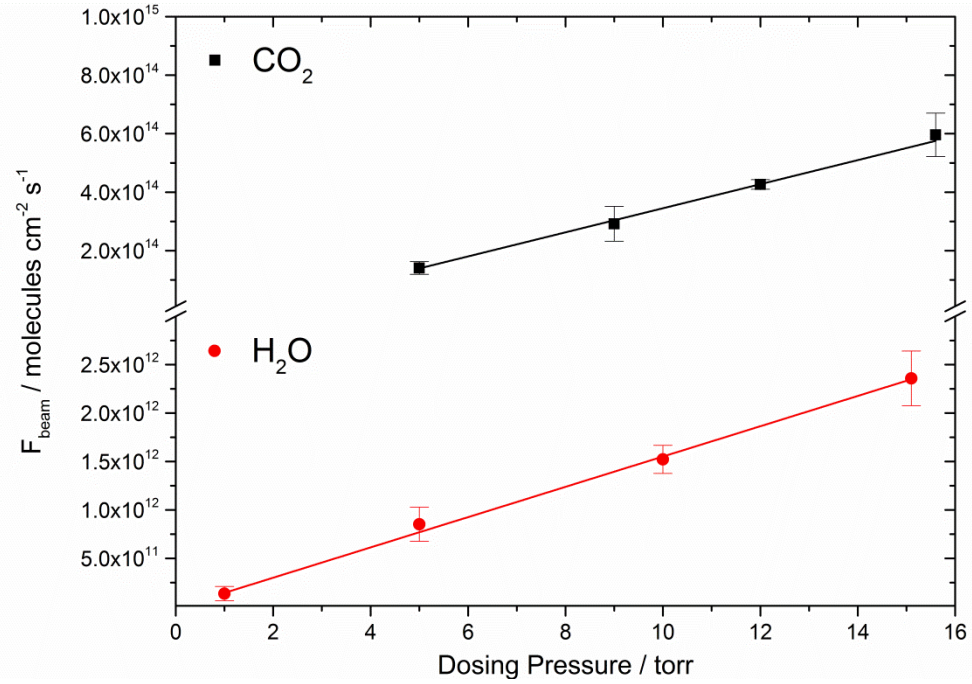

Figure 3.7: Plots of F_{beam} against dosing pressure for CO_2 and H_2O.

$$F_{beam}\ \mathrm{H_2O} = 1.564 \times 10^{11} \times \mathrm{H_2O}\ (P\ /\ \mathrm{torr}) - 1.274 \times 10^{10} \qquad (3.8)$$

$$F_{beam}\ \mathrm{CO_2} = 4.115 \times 10^{13} \times \mathrm{CO_2}\ (P\ /\ \mathrm{torr}) - 6.645 \times 10^{13} \qquad (3.9)$$

Table 2: H_2O and CO_2 Pump-down values of P_0, C_m and F_{beam} for a range of glass line pressures. The errors on F_{beam} are the standard deviation of the repeat measurements at each pressure.

Glass Line Pressure / torr	***P_0* / Pa**	***C_m* / s**	***F_{beam}* / molecules cm^{-2} s^{-1}**
		H_2O	
1	(1.17 ± 0.27) x10^{-7}	0.24 ± 0.19	(1.36 ± 0.74) x 10^{11}
5	(2.79 ± 0.39) x10^{-6}	0.057 ± 0.004	(8.52 ± 1.76) x 10^{11}
10	(5.96 ± 0.28) x10^{-6}	0.048 ± 0.004	(1.52 ± 0.15) x 10^{12}
15.1	(1.03 ± 0.07) x10^{-5}	0.043 ± 0.002	(2.36 ± 0.28) x 10^{12}
		CO_2	
5	(7.12 ± 0.92) x10^{-6}	3.7 ± 0.17	(1.41 ± 0.22) x 10^{14}
9	(1.48 ± 0.29) x10^{-5}	3.68 ± 0.17	(2.92 ± 0.6) x 10^{14}
12	(2.3 ± 0.08) x10^{-5}	3.47 ± 0.19	(4.26 ± 0.16) x 10^{14}
15.6	(3.02 ± 0.48) x10^{-5}	3.71 ± 0.22	(5.96 ± 0.74) x 10^{14}

Inspection of Table 2 reveals significant discrepancies in the calculated values of F_{beam}. The values obtained for CO_2 are 2 - 3 orders of magnitude higher than for H_2O over a similar range of gas bulb pressures. This predicted H_2O flux is several magnitudes too low to form the multilayer films shown in subsection 3.3.2 on experimental timescales. This may be due to the loss of H_2O to surfaces on the dosing line, within the doser and within the

chamber, an issue that is exacerbated by the needle valve position not being diametrically opposite the QMS detector and instead offset by 45º. This causes the collimated beam of H_2O molecules to collide with the sides of the UHV chamber before reaching the detector. This is highlighted by the H_2O pump-down experiments taking 15 times longer to stabilise the dose and 15 times longer to return to base pressure when compared to CO_2. Given this uncertainty, the H_2O beam flux used in the following sections is instead estimated based on the pressure relationship of the CO_2 flux, using a stable combined glass gas-handling line pressure for both species of 15 torr.

3.3 CO_2 trapping in amorphous H_2O ice

3.3.1 CO_2 desorption from the Cu(111) substrate

Using the methods described in section 3.1, initial experiments were undertaken to look at the desorption profile of a pure CO_2 dose in the absence of H_2O. CO_2 was dosed onto the bare Cu(111) sample at base temperature (approximately 98 K) for a range of dosing times (1200 - 7200 s) with subsequent TPD analysis shown in Figure 3.8. As the TPD begins, instantaneous rapid desorption of CO_2 is observed, suggesting that the majority of the CO_2 that sticks to the Cu(111) surface is only extremely weakly physisorbed under these temperature conditions. This conclusion is reinforced by the study of *Ernst et al.* [1999] in which they found that the desorption maximum of CO_2 (on a Cu(110) crystal within a similar UHV system) occurred between 90 and 100 K, meaning that the adsorption conditions in this study (approximately 98 K) lie within the desorption profile of CO_2. This is further indicated by the disjointed leading edge of the profile. The leading edge of the TPD profiles peak at approximately 125 K followed by a falling edge with the absence of further desorption features, returning to background at approximately 220 K. It should be noted that the desorption profiles for CO_2 show no trend of increased adsorption with increasing dose length (total CO_2 flux to the sample ranges from 5×10^{17} up to 3×10^{18} molecules) and are broadly comparable across the CO_2 dose lengths investigated. This suggests a barrier to CO_2 adsorption on already adsorbed CO_2, due to a further reduction in sticking coefficient when transitioning from the monolayer to multilayer regime. This is due to the weak intermolecular interactions (van

der Waals forces) of CO_2/CO_2 adsorption being easily broken down by thermal agitation, leading to a short residence time for CO_2 on the surface. This contrasts with the stronger interactions of polar H_2O molecules adsorbing onto H_2O, of which a minimal barrier to multilayer adsorption exists under the conditions in this study. It is worth noting that neither the monolayer CO_2 or multilayer H_2O is chemisorbed. The H_2O shown in the following subsection is physisorbed under low enough temperature conditions that the weak intermolecular interactions are not broken down. A fraction of the CO_2 flux is weakly physisorbed to the Cu(111) substrate or to already adsorbed H_2O (the sticking coefficients of CO_2 on H_2O and CO_2 on Cu are close to zero).

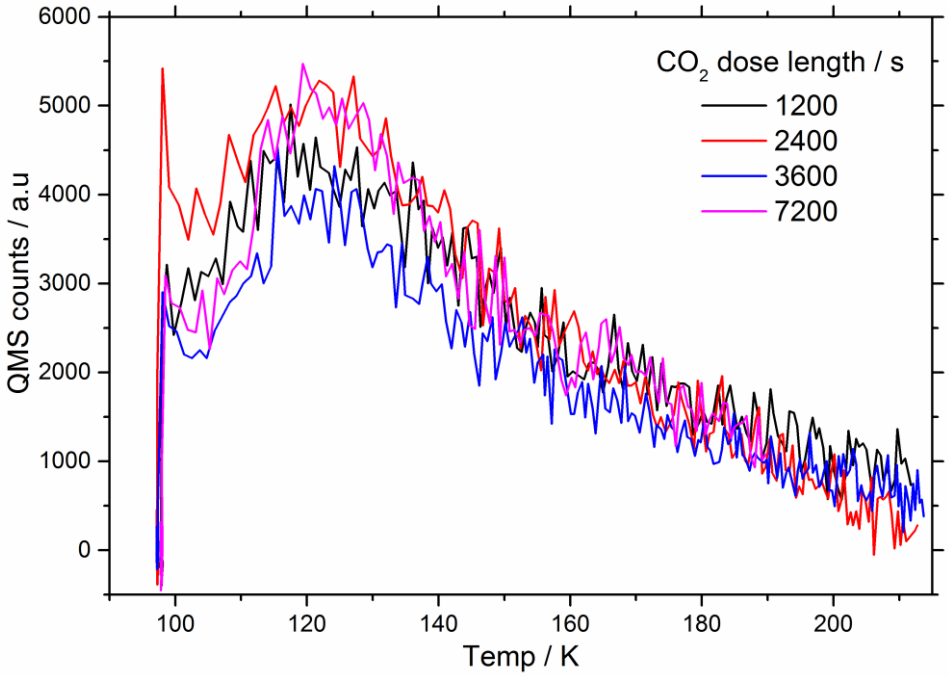

Figure 3.8: TPD traces of CO_2 on bare copper showing the desorption rate in QMS counts (a.u.) against temperature (K) for CO_2 deposited at base temperature (98 K) and varying dose lengths (1200 – 7200 s).

3.3.2 CO_2 trapping and release from H_2O ice

In order to investigate the process of CO_2 trapping in H_2O ice, CO_2:H_2O gas mixtures were deposited and then probed *via* TPD (as detailed in sub-section 3.1.3). Figure 3.9 shows TPD traces of CO_2 desorption from six different experiments in which CO_2:H_2O mixtures of varying ratios (1:1 to 13:1) were dosed onto the Cu(111) sample at base temperature (approximately 98 K). These CO_2 TPD traces were background corrected using pure CO_2 TPD traces (shown in subsection 3.3.1), in order to remove the desorption trace of externally adsorbed CO_2. This results in the residual profile only indicating CO_2 desorption features of CO_2 internally trapped within the H_2O ice matrix. The first desorption feature of trapped CO_2 occurs around 30 K higher than the peak of external CO_2 desorption at 157 K and is prominent in the 1:1 and 3:1 ratio experiments. This desorption feature is known as the molecular volcano peak [*Smith et al.*, 1997b]. The second broader desorption feature accounts for the majority of internal CO_2 desorption at CO_2:H_2O ratios of 3:1 to 12:1 and occurs at 160 - 175 K, referred to as the co-desorption peak. The CO_2 co-desorption peak becomes more prominent while the molecular volcano becomes less prominent, as the CO_2:H_2O ratio increases (and therefore the H_2O flux is reduced). This is followed by a reduction in the co-desorption peak until the CO_2:H_2O ratio reaches 13:1, at which point negligible CO_2 trapping is observed in the ice matrix. This trend of reduced CO_2 trapping with increasing CO_2:H_2O ratio is consistent with *Galvez et al.* [2008].

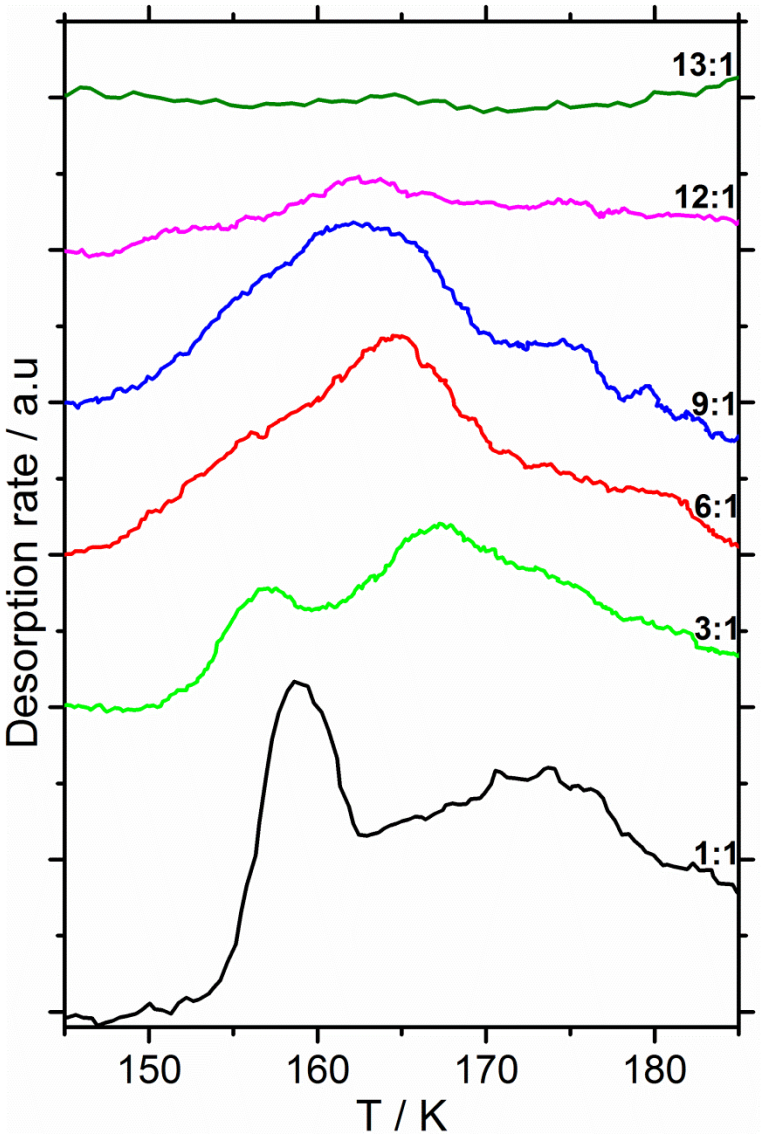

Figure 3.9: Background corrected TPD traces showing the desorption rate (a.u.) of CO_2 against temperature (K) for trapped CO_2/H_2O films (offset for clarity; the zero in each plot is the value at 145 K). The CO_2:H_2O ratio in the dosing mixture is indicated on the right-hand side of each profile.

In order to explain the origin and cause of CO_2 trapped internally in the H_2O ice matrix, the complementary H_2O TPD traces are required. These are shown in Figure 3.10, with the H_2O TPD trace at each CO_2:H_2O ratio corresponding to the CO_2 TPD trace of the same CO_2:H_2O ratio shown in Figure 3.9. The ice film thickness was estimated knowing the total flux of

H_2O to the sample during the dose (calculated in section 3.2), the sticking coefficient of H_2O (0.97 at 98 K), the density of ASW (0.9 g cm^{-3}) and the area of the Cu(111) sample (all variables taken from *Brown et al.* [1996]). Each H_2O TPD trace contains two distinct peaks (most prominently observable for the 1:1 CO_2:H_2O ratio experiment). The first is the ASW desorption peak (the shoulder of the main peak) which occurs at the same temperature as the CO_2 molecular volcano (157 K). This shoulder indicates that ASW was initially deposited onto the surface at 98 K. ASW forms under these conditions as the H_2O molecules do not have the sufficient energy required to re-orientate to more energetically favourable positions and form CSW. The disordered, porous nature of the ASW that forms means that trapped CO_2 molecules can occupy a wide range of different site geometries. The shoulder that can be observed in the leading edge of the H_2O desorption is due to increasingly dominant crystallization of the ASW to form CSW under these temperature conditions which slows overall H_2O desorption. This is due to enough thermal energy becoming available as the temperature increases to mobilise and reorganise the H_2O molecules from the disordered ASW to form ordered CSW. As the H_2O film thickness increases, the ASW and intrinsically linked CO_2 molecular volcano peak shift to higher temperatures due to the greater abundance of ASW available for desorption and crystallisation.

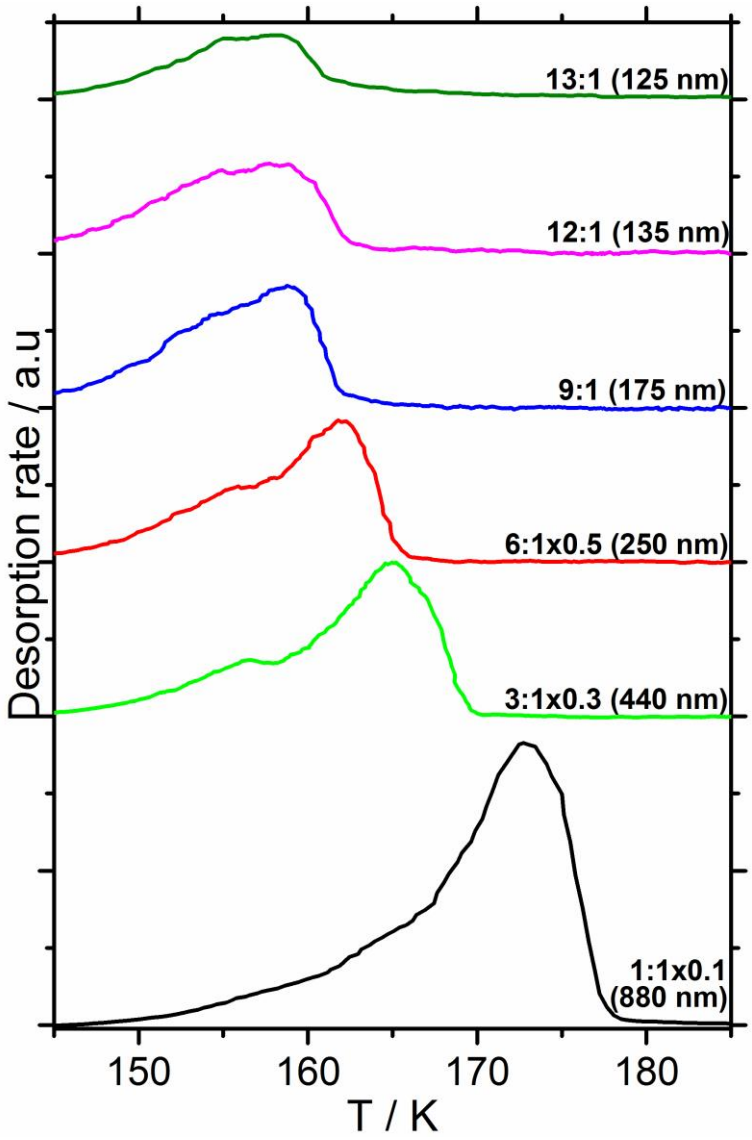

Figure 3.10: H_2O TPD traces showing the desorption rate (a.u.) against temperature (K) for the same CO_2:H_2O ratios as in Figure 3.9 (note that the traces are offset for clarity). Each H_2O trace is labelled with the CO_2: H_2O ratio, the factor by which the data has been rescaled for clarity (if applied) and, in parenthesis, the estimated H_2O film thickness in nm.

The phase change in the H_2O ice and the coupled release of trapped CO_2 *via* the molecular volcano from the ASW ice matrix can be explained using one of two theories: the glass transition; and crystallisation-induced cracking. In the first theory, the ASW film undergoes a glass transition during

annealing [*Jenniskens and Blake*, 1994] which transforms the film into a viscous liquid, enabling the H_2O molecules to re-organise and freeze into CSW (the H_2O desorption shoulder). This molecular reorganisation causes cavities in the ice matrix to open, releasing the trapped CO_2 molecules (molecular volcano) in the uppermost part of the H_2O film producing a short, sharp peak. The temperature of this H_2O glass transition is dependent on several variables including the initial deposition temperature and the heating rate applied [*Jenniskens and Blake*, 1996]. In the second theory, the H_2O ice remains in the “solid” phase throughout the ASW to CSW phase transition. During crystallisation, cracks propagate down through the H_2O film enabling the CO_2 trapped in cavities to escape to vacuum [*May et al.*, 2012; 2013]. This theory is better able to explain the shift to higher temperatures in the CO_2 molecular volcano with respect to increasing film thickness, as the cracks take longer and require higher temperatures to propagate further down the ice layer [*May et al.*, 2011].

The second, higher temperature H_2O desorption peak is the peak of the CSW desorption. The CO_2 co-desorption peak appears at the temperature where maximum desorption of CSW occurs and again shifts to higher temperatures for thicker ice layers. This co-desorption is the release of the remaining CO_2 trapped in the lower layers of the ice matrix that did not have access to the outer surface of the H_2O film during crystallisation of the ASW [*Kumi et al.*, 2006; *Malyk et al.*, 2007].

The extent of CO_2 trapping, as previously mentioned, becomes limited at a CO_2:H_2O ratio of 13:1, at which point no CO_2 desorption features were observed within the ice matrix. In these experiments as the CO_2:H_2O ratio increases, so does the CO_2 flux, while the H_2O flux is decreasing. Given that

the ice film is thinner at 13:1 than the other experiments, it could be the case that the amount of trapped CO_2 is simply below the detection limit of the QMS due to a smaller ice volume. To rule this possibility out, long dose experiments at a CO_2:H_2O ratio of 13:1 were carried out to produce film thicknesses comparable to the lower ratio experiments where CO_2 trapping was observed. These experiments still produced no detectable trapped CO_2. Given that sufficient CO_2 and sufficient film thickness is available across all CO_2:H_2O ratios, the trapping mechanism must be limited by the H_2O flux to the sample surface. Experimentally, this gives a lower limit H_2O flux for CO_2 trapping under these conditions of 4.8×10^{13} molecules cm^{-2} s^{-1}. At lower H_2O fluxes, additional H_2O molecules are not adsorbed quickly enough to close micro-pores in the ice surface. This allows briefly adsorbed CO_2 molecules within these micro-pores to desorb before they can be trapped [*Bar-Nun et al.*, 2007; *Galvez et al.*, 2008; *Laufer et al.*, 1987].

3.3.3 CO_2 trapping under mesospheric conditions

In this subsection the experimentally determined lower limit H_2O flux for CO_2 trapping in ASW is evaluated to determine under what mesospheric conditions CO_2 trapping could occur. This required a comparison to a realistic mesospheric H_2O flux (units of molecules cm^{-2} s^{-1}) where the uptake coefficient was assumed to be unity and is given by:

$$\mathrm{H_2O\ flux} = \frac{\bar{c}}{4}[\mathrm{H_2O}] \qquad (3.10)$$

where $\bar{c}$ is the mean thermal velocity of the H_2O molecules (units of cm s^{-1}) given by:

$$\bar{c} = 1.46 \times 10^4 \sqrt{T/M} \qquad (3.11)$$

where *T* is the absolute temperature in K and *M* is the molar mass in g. The H_2O flux was calculated for conditions typical of the PMC cloud season at an altitude of 83 km (10 ppmv of H_2O for a total pressure of 1 Pa [*Hervig et al.*, 2009; *Rong et al.*, 2012]). For an atmospheric temperature the same as the experimental study (98 K), the maximum H_2O flux predicted is 6.3×10^{13} molecules cm^{-2} s^{-1}, slightly higher than the experimental threshold of 4.8×10^{13} molecules cm^{-2} s^{-1}. A mesospheric CO_2 flux was calculated in the same way for conditions of 360 ppmv of CO_2 at 1 Pa [*Emmert et al.*, 2012], giving 1.2×10^{15} molecules cm^{-2} s^{-1}. This mesospheric CO_2 flux is higher than the experimental range investigated (CO_2 flux = $(3.4 - 6.3) \times 10^{14}$ molecules cm^{-2} s^{-1}) suggesting sufficient CO_2 was available to facilitate trapping. So far this comparison is for a low temperature of 98 K, a temperature that would require strong gravity wave perturbations, rarely reached in the mesosphere [*Lübken et al.*, 2009]. If a parcel of air was cooled to such low temperatures the H_2O would have already condensed, either *via* heterogeneous nucleation below 145 K to CSW or to ASW *via* homogeneous nucleation at highly supersaturated conditions ($S_{ice} = 10^4 - 10^8$) [*Lübken et al.*, 2009; *Murray and Jensen*, 2010; *Plane*, 2011; *Rapp and Thomas*, 2006]. It is therefore necessary to extend this comparison to more frequently observed mesospheric temperature conditions in order to determine the full range of conditions under which CO_2 trapping would be plausible atmospherically. This can be done by estimating the average number of H_2O molecules that would need to deposit onto a CO_2 molecule on the ice surface, in order to prevent the CO_2 molecule desorbing. First, the residence time of a CO_2 molecule on the ASW surface

(τ) is calculated using the reciprocal of the desorption rate coefficient for CO_2, k_{des}, given by *Attard* [1998] as:

$$\tau = \frac{1}{k_{des}} = \frac{1}{A \exp(-\frac{E_{des}}{RT})} \quad (3.12)$$

where A is a pre-exponential factor corresponding to the average frequency of oscillation for the librational modes of CO_2 (2.9×10^{12} s^{-1}) and E_{des} is the binding energy of CO_2 on ASW (23.7 kJ mol^{-1})[*Sandford and Allamandola*, 1990]. This gives τ = 1.48 s for CO_2 on ASW at 98 K. Then, taking the collision cross section of a CO_2 molecule as 0.52 nm^2 [*Atkins and De Paula*, 2009] and the measured experimental H_2O flux limit, a minimum of 0.4 H_2O molecules must deposit on a CO_2 molecule in order to trap it within the ASW before it desorbs. Following this, the number of H_2O molecules depositing on an adsorbed CO_2 molecule under a range of atmospheric temperature and H_2O concentrations was calculated, accounting for the change in CO_2 residence time and H_2O/CO_2 flux. Using 0.4 H_2O molecules per CO_2 as a lower limit, the minimum atmospheric H_2O mixing ratio required to achieve CO_2 trapping across temperatures of 90 - 110 K is shown in Figure 3.11. The region above the red line indicates plausible mesospheric conditions for CO_2 trapping in ASW. Current maximum mesospheric H_2O concentrations during the PMC season are approximately 10 ppmv, suggesting temperatures below 100 K would be required for CO_2 trapping within PMC ice particles. At higher (but still extreme) temperatures more often reached in the mesosphere, such as 110 K, the H_2O concentration would need to be an order of magnitude higher to allow for CO_2 trapping to become a significant process. This leads to the conclusion that CO_2 trapping in ice under current

mesospheric conditions would only be plausible at extreme temperatures below 100 K and not be a common occurrence.

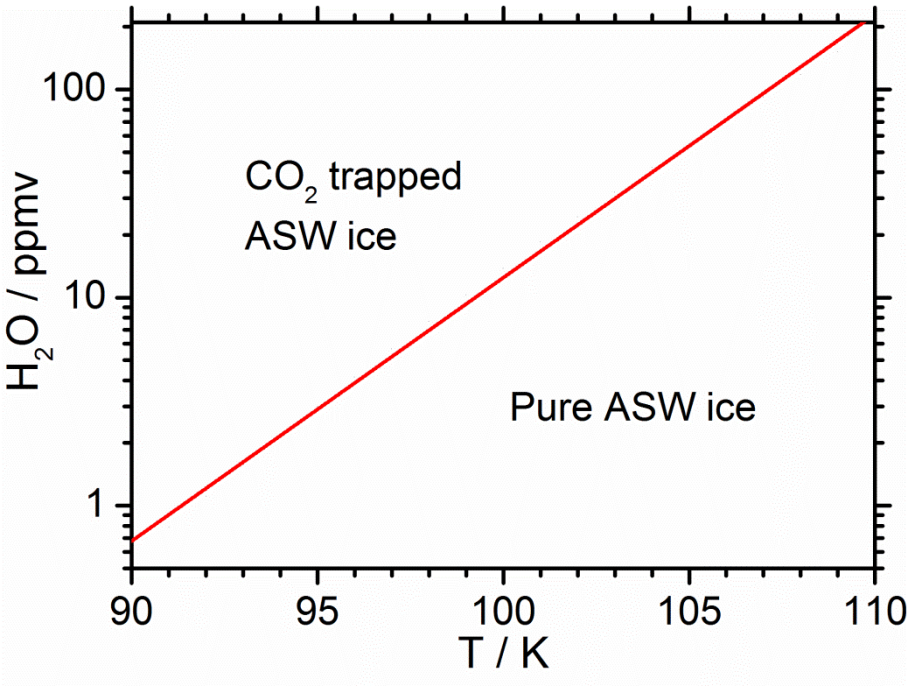

Figure 3.11: A plot of the minimum H_2O concentration (ppmv) required to trap CO_2 in ASW, as a function of temperature. Conditions above the red line are conducive to CO_2 trapping in ASW.

The changing mesosphere was discussed in chapter 1 and could make CO_2 trapping in the mesosphere a more likely process in the future. CO_2 is well mixed up to approximately 80 km, increasing in the mesosphere at comparable rates to surface CO_2 at approximately 20 ppm decade^{-1} [*Emmert et al.*, 2012; *Garcia et al.*, 2014]. Mesospheric H_2O concentrations in the northern hemisphere (77ºN) are increasing at a proportionally smaller rate of 0.07 ± 0.03 ppm decade^{-1} [*Hervig et al.*, 2016a]. The mesosphere is also cooling at the polar regions at a rate of 0.58 ± 0.32 K decade^{-1} [*Berger and Lübken*, 2015]. This mesospheric cooling is driven by CO_2 which has a

cooling effect above 20 km. CO_2 converts thermal energy into IR fluorescence, a significant fraction of which escapes into space [*Laštovička et al.*, 2008]. These trends in H_2O and CO_2 concentration, as well as an intrinsically linked cooling mesosphere all make the process of CO_2 trapping more likely in the future. The likelihood of this process occurring in the mesosphere should therefore be revisited if current trends persist.

3.4 Summary and conclusions

This work has detailed the processes of experimentally trapping CO_2 within an amorphous H_2O ice across a range of CO_2 and H_2O deposition conditions within a UHV chamber. Specifically, the molecular volcano and co-desorption of CO_2 was investigated. Through quantitative determination of the beam flux for the gas species, the limit of CO_2 trapping was established, and attributed to the reduction in the H_2O flux. Comparison of experimental trapping limits to comparable conditions in the mesosphere of Earth, leads to the conclusion that CO_2 trapping is currently an unlikely process except under the most extreme temperature conditions (< 100 K).

4 Deposition of Mg and K on ice: Effects of sublimation and energetic particle bombardment

The deposition and potential reactivity of metal atoms on water ice can be an important process in the mesosphere, affecting the gas-phase chemistry [*Murray and Plane*, 2005]. In this chapter Mg and K were deposited on water-ice films prepared under UHV conditions at temperatures of 110 to 140 K. Energetic sputtering of metal-dosed ice layers by 500 eV Ar^+ and Kr^+ ions showed that whereas K reacts on (or within) the ice surface to form KOH, adsorbed Mg atoms are chemically inert. Combining the experimental data with electronic structure calculations of the metals bound to an ice surface, Mg was found to be unreactive, binding at surface defects, while K readily reacted with the ice surface to produce KOH (8 kJ mol^{-1} exothermic). Theoretical adsorption energies are also reported for K (-68 kJ mol^{-1}), Mg (-91 kJ mol^{-1}) and Fe (-306 kJ mol^{-1}) on ice. TPD experiments revealed that negligible Mg and K containing species co-desorb when the ice film sublimates, indicating that uptake on ice particles causes irreversible removal of the metals from the gas phase. This suggests that uptake on ice particles in polar mesospheric clouds accelerates the formation of large meteoric smoke particles (≥ 1 nm radius) following sublimation of the ice.

4.1 Methodology

The UHV chamber used in this study was also used in Chapter 3 to look at CO_2 trapping in ASW and is described in detail in Chapter 2. To avoid repetition, detail regarding preparation of gas mixtures, dosing and TPD can be found in section 3.1. Prior to each experiment the Cu(111) crystal was cleaned by annealing to 800 K for 30 min and when necessary, sputtered by 500eV Ar^+ or Kr^+ using the inert ion sputter source to remove any residual Mg or K.

In a typical experiment an H_2O ice film was deposited on the Cu(111) crystal using a purified source of H_2O, directed by the needle valve at the substrate (held at mesospherically relevant temperatures of either 110 or 140 K) as an effusive collimated beam. To determine surface coverage, the pressure dependent beam flux of this doser for H_2O was previously calibrated for the UHV chamber in section 3.2 and for this study was 5.5×10^{14} molecules cm^{-2} s^{-1}. For a 7200 s H_2O dose under the temperature conditions of this study (110 – 140 K) using a sticking coefficient of 0.97 and an ice density of 0.9 g cm^{-3} taken from *Brown et al.* [1996], this deposited an estimated 1.3 µm thick ice film. A Mg or K layer was then dosed on top (surface) or in the middle (sandwich) of the ice film using the appropriate monolayer dosing apparatus. This metal-ice layer was then subject to analysis via two different thin film techniques. The first was TPD (see sub-section 3.1.3), which investigated the thermal release from the ice layer of Mg and K containing species. A linear heating ramp of 0.5 ± 0.02 K s^{-1} was used, corresponding to the maximum evaporation rate of PMC ice particles estimated by [*Gadsden*, 1982]. The second technique used was energetic

ion sputtering by 500 eV Ar^+ or Kr^+ directed at the Cu(111) substrate, combined with mass spectrometry to monitor ejected species. The energetic sputtering removes layers of the H_2O ice film and adsorbed metal species, effectively burrowing through the ice layer to provide a profile of the metal species present throughout the ice (illustrated in Figure 4.1).

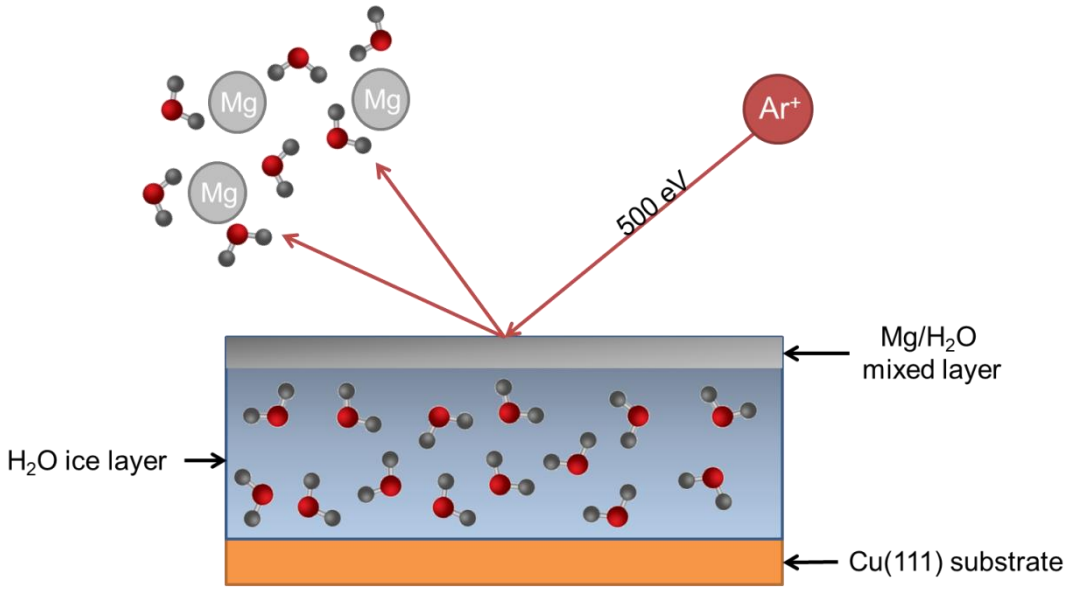

Figure 4.1: Diagram showing the energetic sputtering ions of an Mg dosed ice layer by 500 eV Ar^+. This high energy impact stripped Mg (or K) and H_2O from the layer which was then detected by the QMS.

The mass spectra taken of Mg-ice and K-ice sputtering were background corrected against a corresponding sputter profile of pure ice. These sputter profiles were also normalized in terms of fluctuations in the ion beam, measured as a change in the current to the sample via a pico-ammeter connected to the substrate. Results from TPD experiments are described in section 4.2. Energetic sputtering of pure H_2O layers are shown in section 4.3 and sputtering of Mg and K dosed ice layers are shown in section 4.4. The

electronic structure calculations and analysis shown in section 4.5 were carried out by Prof John Plane.

4.2 Sublimation of metal-ice layers

Mg-ice and K-ice layers were deposited as described in section 4.1 and then subject to TPD in order to simulate the sublimation of ice particles within a PMC. In Figure 4.2 TPD traces of multilayer H_2O films (Mg or K dosed ice) deposited at 140 K are shown, a profile that is consistent with previous studies [*Fraser et al.*, 2001]. In the case of H_2O dosed at 140 K (subsequently cooled to 110 K before TPD), a crystalline ice is formed [*Sack and Baragiola*, 1993; *Safarik and Mullins*, 2004]. This ice layer therefore does not undergo the glass transition of the amorphous ice deposited at 98 K and discussed in Chapter 3. As the temperature of the sample was increased from 110 K, sublimation of the ice was detectable at approximately 140 K, peaking at 183 K. If the adsorbed Mg and K did desorb from the ice layer, co-desorption would have peaked at approximately the same temperature as the crystalline ice. Co-desorption has been previously observed in chapter 3, for CO_2 trapped in H_2O ice. However, the TPD traces for Mg and K are primarily within the background noise (3σ) suggesting that desorption of the metals from the ice was negligible. Monitoring other K (KOH) and Mg (MgO, MgOH, $Mg(OH)_2$) species during the TPD experiments also displayed no detectable co-desorption peak. This lack of co-desorption was also observed in TPD traces taken of Mg and K dosed onto amorphous ice at 110 K.

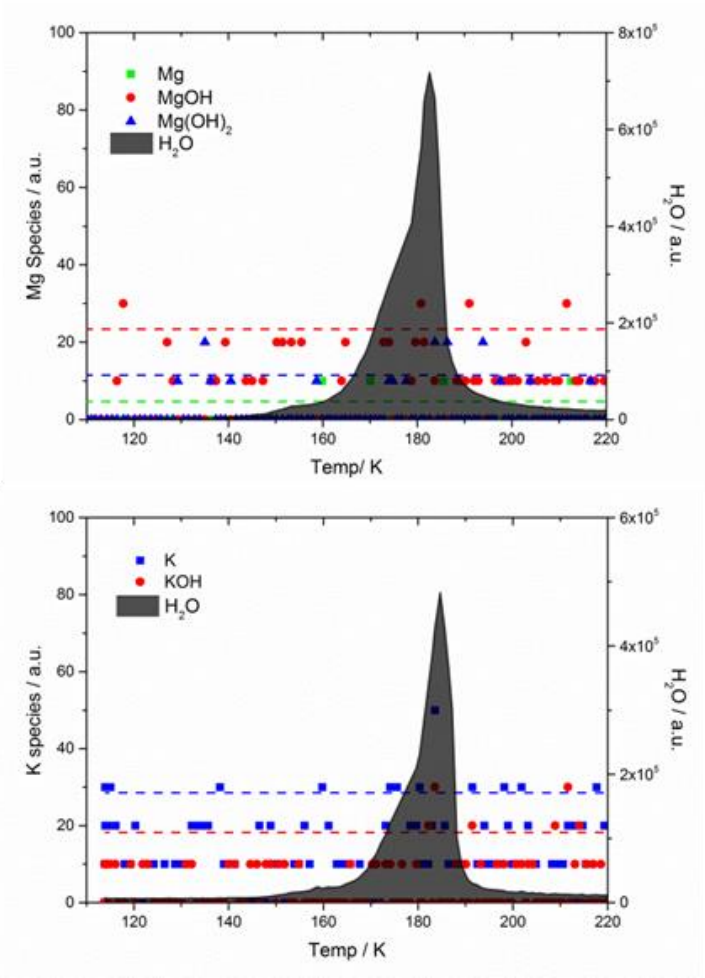

Figure 4.2: TPD traces of Mg (top) and K (bottom) dosed onto H_2O ice at 140 K, including associated compounds that were monitored by the QMS. The dashed lines indicate the 3σ noise for the corresponding species based on the background signal.

Figure 4.3 shows mass spectra of energetic ion sputtering (500 eV Kr^+ for K, 500 eV Ar^+ for Mg) of the Cu substrate carried out after the TPD shown in Figure 4.2. In both the case of Mg and K, clear broad peaks were detected (m/z = 24 and 39 respectively) corresponding to the respective metal species. This observation reveals that instead of co-desorbing with the ice, Mg and K species are instead left behind as a residual on the Cu(111)

substrate after the ice layer has sublimated, this process has also been observed previously in the case of Fe [*Frankland and Plane*, 2015].

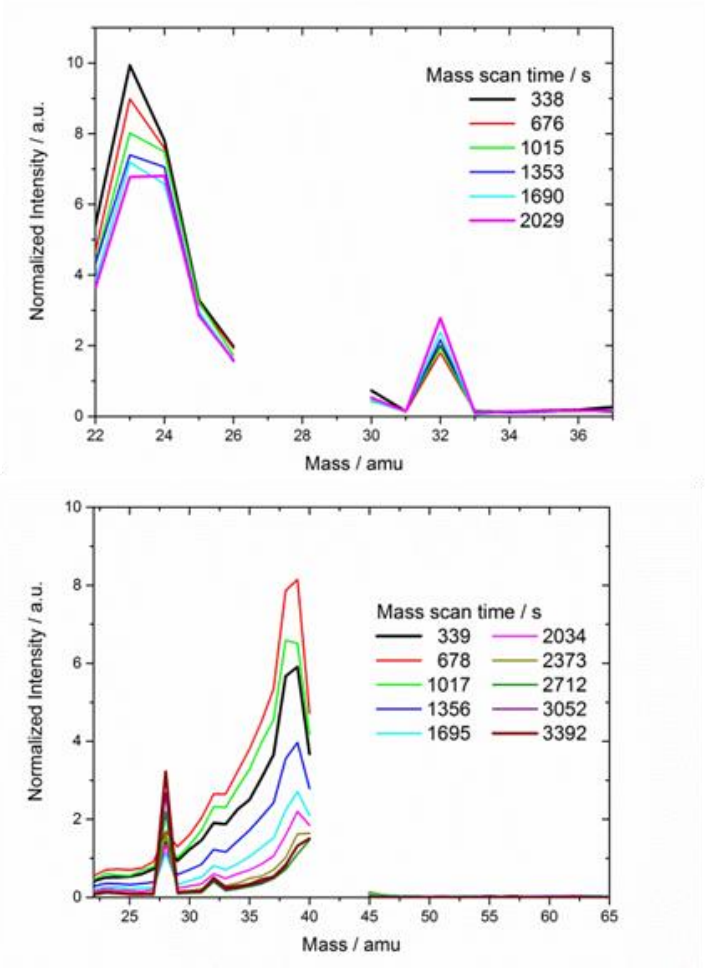

Figure 4.3: Histogram mass spectra of the Mg (top) and K (bottom) normalized signal observed during energetic ion sputtering (by either 500 eV Ar^+ or Kr^+) of the Cu substrate after sublimation of the ice layer. m/z gaps in the sputter profiles correspond to the removal of background signals for N_2 (m/z = 28) and double charged Kr (m/z = 42).

4.3 Energetic sputtering of pure H_2O ice

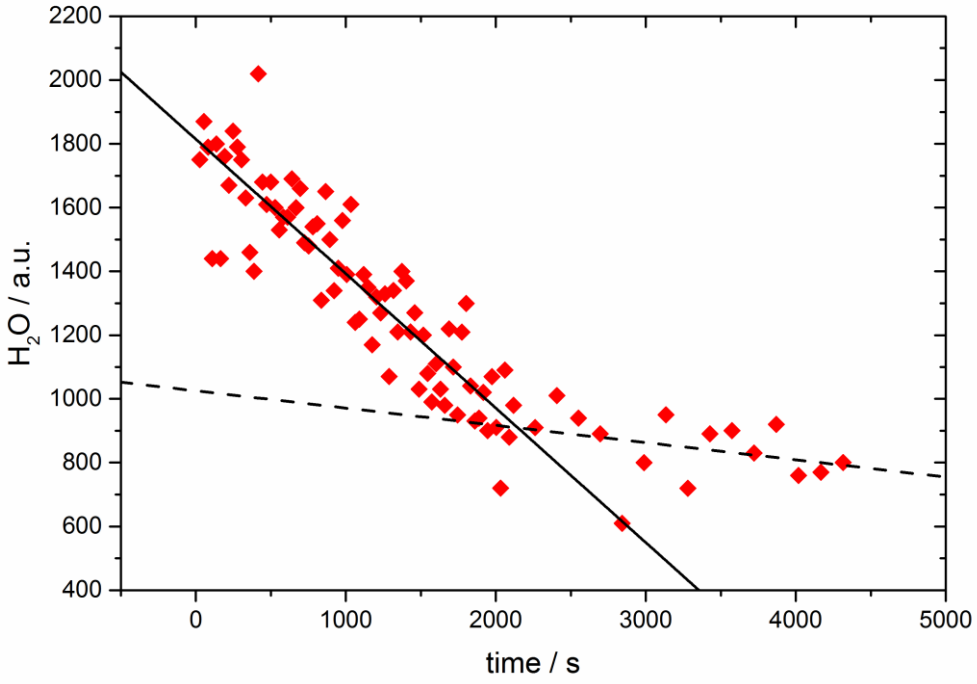

Figure 4.4: Example H_2O trace monitored during the time of energetic sputtering by 500 eV Ar^+ of a 1.3 µm ice layer held at 110 K. Linear fits are applied to two sections of the data to illustrate a reduction in signal to background levels.

Background experiments were undertaken to investigate the sputtering of the H_2O ice layer by 500 eV ions. An example of such an experiment is shown in Figure 4.4 for sputtering of a 1.3 µm H_2O layer by 500 eV Ar^+. The H_2O signal reduces with time, as sputtering removes H_2O molecules from the ice surface until the signal reaches background levels at 2100 s. At 2100 s the Ar^+ beam has sputtered down through the whole ice layer and coincides with a sputter peak at m/z = 63, attributed to sputtering of the now exposed Cu(111) substrate.

Sputtering at 500 eV can be described as a cascade of elastic collisions within the ice when the Ar^+ impacts the ice surface [*Galli et al.*, 2016]. This means each Ar^+ ion impacts a wider area of the sample than simply its physical cross section. The sputter rate of H_2O can be estimated using an Ar^+ flux of $(8.2 \pm 0.3) \times 10^{13}$ Ar^+ cm^{-2} s^{-1} [*Frankland and Plane*, 2015], the total sputter time of 2100 s and the total number of H_2O molecules adsorbed to the substrate (3×10^{18} molecules). This gives a sputter rate estimate of 17 H_2O molecules for each Ar^+ impact. It should be noted that this is an upper limit estimate, as only an unknown fraction of the H_2O layer is removed by sputtering. This means that the real sputter rate will be less than 17 H_2O molecules per Ar^+. This upper limit sputter rate is still of comparable magnitude to literature values for Ar^+ sputtering of low temperature H_2O ice [*Famá et al.*, 2008; *Galli et al.*, 2016].

4.4 Energetic sputtering of Mg and K dosed ice

The interaction of Mg and K adsorbed to the ice layer was probed by in-situ sputtering of the ice without TPD. Metal-ice layers were deposited (see section 4.1) and 60 minutes after deposition were subject to energetic sputtering. The normalized signals of gas phase Mg and K species removed from H_2O ice via energetic ion sputtering are shown in Figure 4.5. By monitoring the H_2O sputtering (see section 4.3) and knowing the H_2O ice thickness (1.3 µm), it was possible to convert the total sputter time (assuming a linear sputter rate) to an estimate of the distance through the ice layer, shown on the top abscissa in Figure 4.5.

Firstly, it is clear from the sputter profiles that energetic sputtering by 500 eV Ar^+ and Kr^+ readily removes Mg and K from the ice surface that were adsorbed 60 minutes after deposition. The metal traces reach background levels by the time the energetic sputtering had burrowed through the H_2O ice film (2100 s) and begun to sputter the Cu(111) substrate below.

In the case of Mg (top of Figure 4.5), the profiles of surface compared to sandwich adsorbed Mg are quite different. The surface adsorbed Mg remained close to the surface of the ice, producing a sharp peak approximately 80 nm below the surface of the ice layer. A rapid initial decay in the signal with a long tail is observed after the Mg peak. The sandwiched H_2O-Mg-H_2O layer peaks closer to the middle of the ice layer (approximately 500 nm deep) as would be expected based on the deposition conditions, but has a broader, more diffuse profile both towards the surface of the ice, and towards the Cu(111) substrate.

In the case of K (middle of Figure 4.5), differences compared to the position of the Mg within the ice layer are apparent, and generally the K species are adsorbed deeper in to the ice. The surface adsorbed K displays a broader primary peak that occurs almost 300 nm deeper into the ice layer than for surface Mg. The peak K signal from the sandwiched H_2O-K-H_2O layer is from deeper into the ice than the respective Mg experiment, but shows a peak profile similar to the surface adsorbed K. A smaller secondary peak in the signal near the surface of the ice is observed at the same ice depth (approximately 100 nm) in both K experiments. This comparable K ejection from different deposition conditions could be caused by K ejected during

sputtering from a different surface such as the W mounting wires, or Cu support arms where H_2O may also have been present.

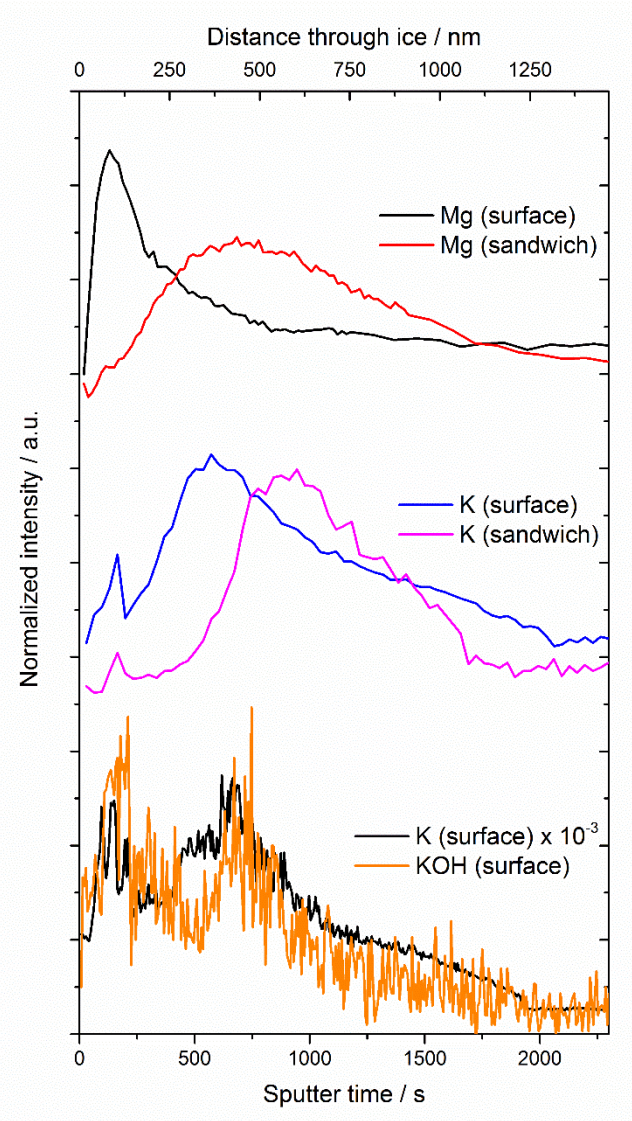

Figure 4.5: Vertically offset profiles of normalized Mg and K signals produced by energetic sputtering of metal-ice layers deposited at 110 K using 500 eV ions of Ar^+ or Kr^+. “Surface” profiles indicate metal adsorbed onto the 1.3 µm ice layer, while “sandwich” profiles indicate when the metal was adsorbed between two 0.65 µm ice layers. The bottom profile highlights KOH formation when the QMS was set to lower ionisation energies in order to avoid fragmentation (20 eV instead of 70 eV).

An interesting question is what process governs the differing peak positions of the metals. Are the differences due to the binding, diffusion rates or simply just different deposition conditions created by the two dosers. A set of experiments with a range of delay times before sputtering (15 – 120 mins) did not exhibit an observable trend of increased diffusion of the metals into the ice with time. The possible effects of the different binding of the metals is discussed in section 4.5 but it isn't possible to rule out possible effects of different deposition conditions.

With the QMS set at an electron energy of 70 eV, no reactive products of Mg or K on the ice surface were detected (m/z range of 20 – 80). This could be due to un-reactivity of the metals with the ice, or because reaction products were fragmented within the QMS and therefore not detected. The electron impact ionization of the QMS was therefore shifted down to lower electron energies (20 eV) in order to detect reaction products that would otherwise have been fragmented at 70 eV. Once again, no reaction products were detected across deposition temperatures of 110 - 140 K for Mg, suggesting Mg is unreactive when adsorbed to ice under these conditions. K-ice experiments at lower electron energy led to an observed peak at m/z=56 in the sputter signal, assigned as KOH and shown at the bottom of Figure 4.5. The corresponding K signal has been scaled and highlights the comparable profile shape of K and KOH through the ice layer. Both the primary and secondary peaks of K and KOH occur at similar distances into the ice, suggesting KOH is formed wherever K is present. In a previous photoelectric emission study by *Vondrak et al.* [2009] the K signal on the ice decayed on a time scale of several minutes. Given the 60 minutes' delay between deposition of the metal and sputtering in these experiments, it suggests that

(in the absence of another loss mechanism) complete conversion of K to KOH in the ice layer is occurring. The observed K signal at 20 eV would then be attributed to the majority of KOH formed on the ice still fragmenting under these conditions. Operating the QMS at 20 eV was the experimental lower limit of the system in terms of detecting K species ejected from the ice.

4.5 Electronic structure calculations of Metal-ice interactions

In order to explain and understand the reactivity of K and un-reactivity of Mg on the ice surface seen in the experimental data in section 4.4, theoretical calculations of the metals binding to ice were undertaken. Calculations for Fe with relevance to the previous work of *Frankland and Plane* [2015] were also done. These electronic structure calculations were carried out by Prof John Plane at the B3LYP/6-311+G level of theory using the Gaussian 09 suite of programs [*Frisch et al.*, 2009].

Figure 4.6 shows the optimized structures of Mg, Fe and K adsorbed on a model ice surface consisting of 12 H_2O molecules arranged in two stacked hexagonal rings. There are significant differences in the way the three metal atoms adsorb.

In the case of Mg, the adsorption energy is -91 kJ mol^{-1}; however, the Mg is bound to the lone electron pair on a *single* H_2O molecule, on the outside of the hexagonal H_2O structure at a surface irregularity. The Mg is therefore unreactive, but adsorbs relatively strongly at this site. Binding at the surface irregularity in a theoretical open 12 H_2O molecule system is possible, but would have different implications for a real bulk ice in the case of a PMC particle. Instead of binding at the edge of the H_2O ring Mg would bind only at a defect/imperfection on the crystal surface such as a step edge. This Mg adsorption behaviour could explain the experimental observation in Figure 4.5 where the majority of the Mg is adsorbed close to the surface of the ice. Binding only at surface defects also suggests that the uptake of Mg onto ice

will be lower compared to K or Fe and will depend on its ability to migrate to these surface defect sites.

The Fe adsorption energy is -306 kJ mol^{-1}, because the Fe has actually inserted into a H_2O molecule to form the very stable HFeOH molecule bound to the surface. This is consistent with the observation of $Fe(OH)_2$ in the sputtering experiment of *Frankland and Plane* [2015]. After the formation of HFeOH, further rearrangement with an adjacent H_2O on the surface should produce $Fe(OH)_2 + H_2$ without a significant activation barrier [*Frankland and Plane*, 2015].

The K adsorption energy is lower at -68 kJ mol^{-1}. However, once adsorbed the K atom can insert into a surface H_2O, producing KOH embedded at the ice surface with a dangling H atom (bottom panels of Figure 4.6). This state is only 60 kJ mol^{-1} higher in energy than the initially adsorbed K atom. Thus, the overall process to form KOH is -8 kJ mol^{-1}. This process is slightly exothermic or perhaps thermo-neutral, within the uncertainty at this level of theory [*Foresman and Frisch*, 1996]. In contrast, the *gas-phase* reaction $K + H_2O \rightarrow KOH + H$ is 171 kJ mol^{-1} endothermic (at the B3LYP/6-311+g(2d,p) level), illustrating the significant solvation of polar KOH on the ice surface. Once KOH has formed, the dangling H atom can easily migrate across the surface to find another dangling H and form H_2. The energy involved in converting the adsorbed K to KOH is consistent with the decay rate of K of 5×10^{-3} s^{-1} on ice at 92 K [*Vondrak et al.*, 2009].

Without the metals present in these electronic structure calculations this 12 H_2O molecule system would be observed as two perfectly mirrored hexagonal rings. Due to the strong binding of the metals to the ice

(equivalent of 3+ hydrogen bonds) distortion of the H_2O rings occurs. Less distortion would be expected for a real world bulk ice system, in which the H_2O rings are locked into more rigid sheets of hexagons.

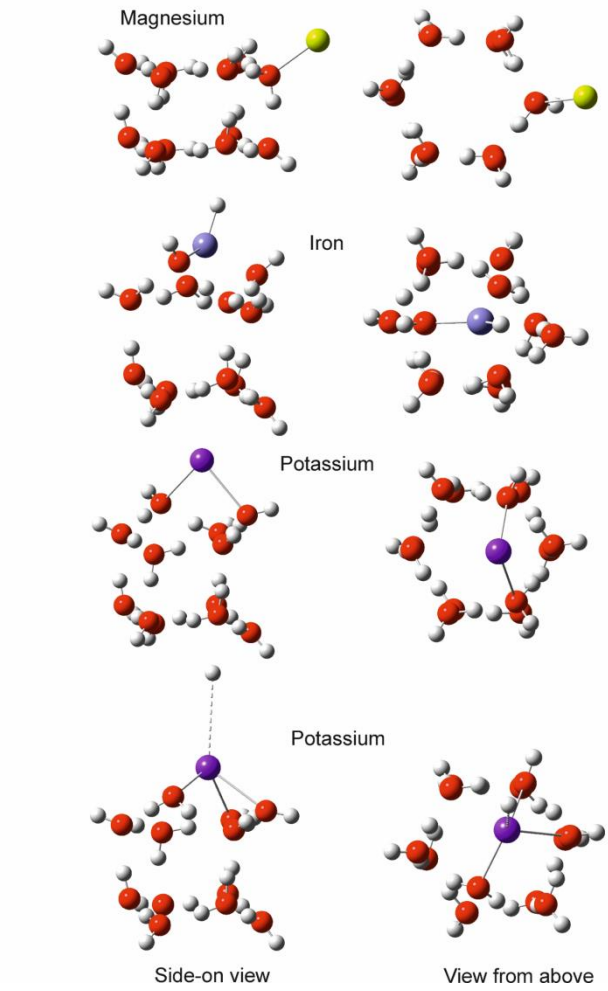

Figure 4.6: Structures of Mg, Fe or K bound to a model ice surface of two hexagonal rings of 6 H_2O molecules based on electronic structure calculations (at the B3LYP/6-311+G level of theory). The white spheres are H atoms and the red spheres are O atoms. An Mg atom (yellow spheres) is shown bound to ice in the top two panels, while an Fe atom bound to ice (grey spheres) is shown in the following two panels. In the lower 4 panels a K atom is shown first binding to the ice and then reacting to form KOH and releasing an H atom.

4.6 Effect of metal uptake on ice on MSP coagulation

It was shown in section 4.2 that Mg and K were not co-desorbed with the ice layer during sublimation and instead the metals were left as residuals on the substrate surface. This process has also been observed for Fe by *Frankland and Plane* [2015]. This residual formation raises an interesting question regarding the coagulation of MSPs in the presence of PMCs.

The 1.3 µm thick H_2O film was evaporated during the TPD experiments in approximately 100 seconds giving a desorption rate of 13 nm s^{-1} (at a heating ramp of 0.5 ± 0.02 K s^{-1}). This rate is much higher than the predicted maximum desorption rate estimated in the mesosphere of about 0.6 nm s^{-1} (for a 50 nm radius ice particle at 170 K) by *Gadsden* [1982]. It is unlikely that adsorbed metals on PMC particles undergoing this comparatively slower evaporation rate would co-desorb, and indicates that the experimental observation here should be atmospherically analogous to the sublimation of PMC particles.

For PMCs this suggests that any metals removed from the gas phase onto the ice particle surface would be permanently locked into the solid phase. As the region of the mesosphere warms, or the PMC particles sediment into a warmer and/or unsaturated region of the mesosphere, sublimation of the H_2O will commence. The adsorbed metal species will then migrate deeper into the particle until sublimation of the PMC particle is complete, leaving behind a residual particle composed of adsorbed metal atoms, metal compounds, and MSPs, including (for heterogeneous nucleation) the particle on which the ice originally condensed. This process means that PMC particles in the Earth's mesosphere will compete with MSP growth via

coagulation and condensation of metallic species from the gas phase, which in turn may influence the growth and transport of MSPs during summer at high latitudes. PMCs could therefore act as a second MSP coagulation mechanism. Figure 4.7 shows a comparison of the surface area available for growth and coagulation on existing MSPs (taken from modelling the distribution of charged particles measured by a rocket payload [*Plane et al.*, 2014]), compared with the surface area available on ice particles during a strong PMC event (modelled from lidar backscatter measurements at the South Pole [*Plane et al.*, 2004]). At the cloud peak, the PMC provides at least 2 orders of magnitude greater available surface area for metal uptake compared to the background MSPs.

In order to illustrate the effect of the increased surface area available on PMCs for MSP production, a simple model of MSP formation due to metal uptake on PMCs is detailed here for typical PMC conditions in the mesosphere. Metal uptake was evaluated for a mesospherically abundant metal (Fe) using conditions representative of 83 km and 140 K with an Fe density of 10^4 atom cm^{-3} based on model and lidar data from *Feng et al.* [2013]. Injection of fresh Fe into the layer from meteoric ablation is taken as 0.05 atom cm^{-3} s^{-1} from *Carrillo-Sánchez et al.* [2016]. An uptake coefficient of unity is used for Fe on ice and uptake is calculated using first order uptake kinetics (see *Frankland et al.* [2015] for theory).

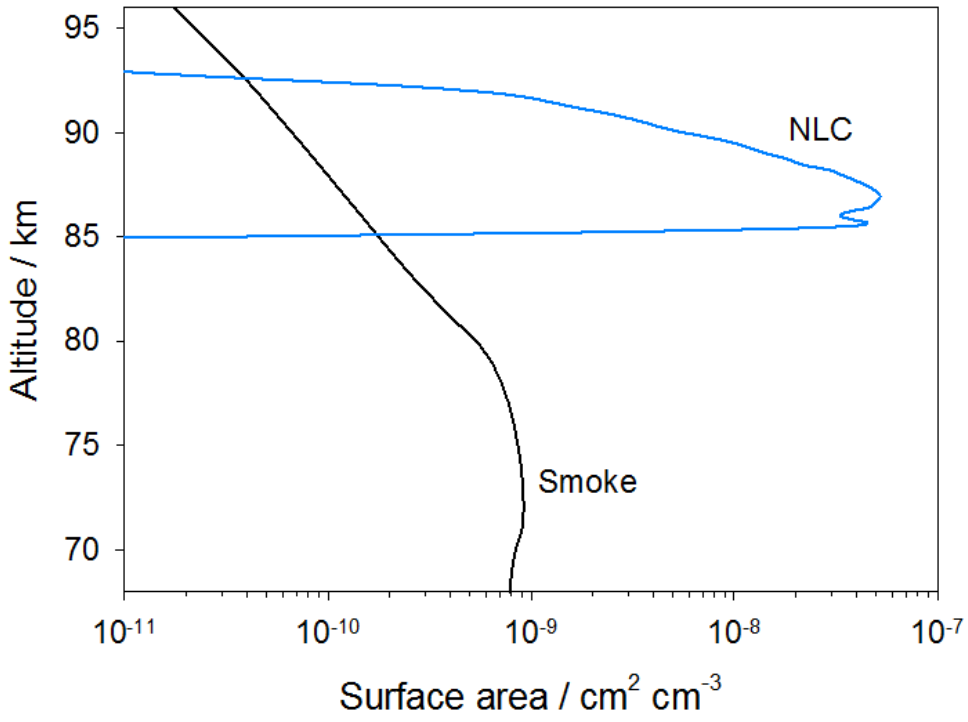

Figure 4.7: Comparison of available surface area from MSPs (taken from modelling the distribution of charged particles measured by a rocket payload [*Plane et al.*, 2014]) and during a strong PMC event (modelled from lidar backscatter measurements at the South Pole [*Plane et al.*, 2004]).

This uptake of Fe over time is shown in Figure 4.8 for a range of ice particle concentrations. At an ice surface area of 6 x 10^{-8} cm^2 cm^{-3} (200 cm^{-3} of 50 nm radius ice particles) the Fe layer is 99+ % depleted within 5 hours under the strong PMC conditions shown here [*Murray and Plane*, 2005; *Plane et al.*, 2004]. Therefore, assuming complete depletion of the Fe layer on this timescale is a reasonable approximation. While PMCs can persist for 24+ hours, 5 hours is representative of individual ice particle lifetimes in a strong PMC [*Kiliani et al.*, 2013]. The Fe adsorbed to an individual ice particle is assumed to coagulate into a single spherical MSP (density of 2 g cm^{-3}) after

sublimation of the ice. This produces MSPs (200 particles cm^{-3}) with a radius of 1.25 nm (If fayalite (Fe_2SiO_4) was formed) or a radius of 1 nm (if goethite (FeO(OH)) was formed).

This simple model does not account for coagulation with any MSP that nucleated the ice initially, which would further increase the radius of the residual MSP formed. Inclusion of any MSPs already present in the ice can be evaluated using the measurements of *Hervig et al.* [2012] where a 0.01-3% volume inclusion of MSP in PMC particles was deduced. If this volume of MSP was present in 50 nm radius ice particles after sublimation it would leave a 2.4 – 15.8 nm radius MSP (assuming the same MSP density of 2 g cm^{-3}).

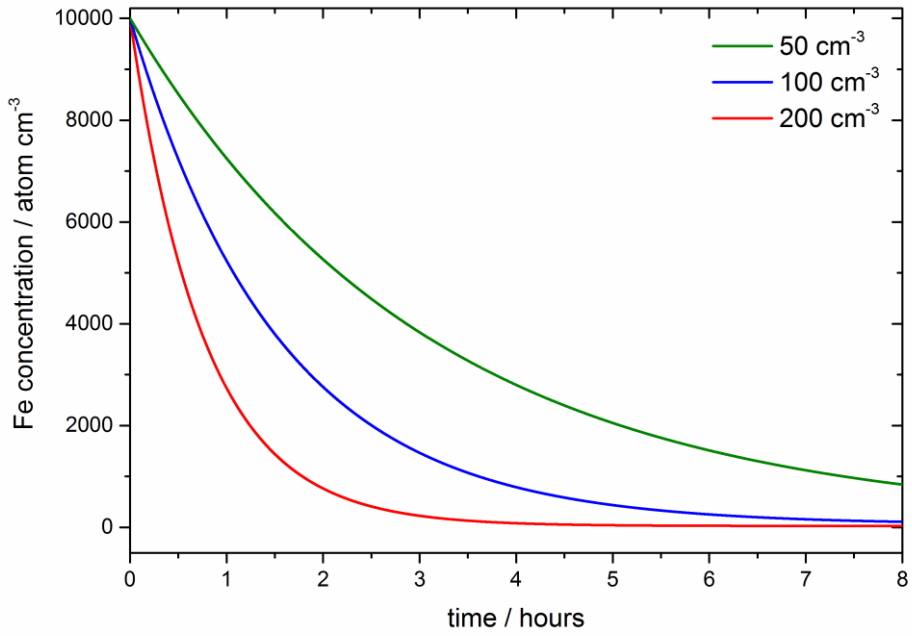

Figure 4.8: Calculated depletion of a 10^4 atom cm^{-3} Fe layer by uptake on 50 nm radius ice particles at varying number concentrations. This was for typical conditions at 83 km.

MSP formation by PMCs can be compared to the predicted growth of MSPs by coagulation in a 1-D microphysical model that used an ablated input of 5 t d^{-1} [*Plane et al.*, 2014]. For an altitude of 83 km, the concentration of 1 nm radius MSPs is 100 cm^{-3} and for 2 nm radius MSPs is 60 cm^{-3}. The coagulation of MSPs in PMC particles would affect the distribution of MSPs in the region of the cloud, increasing the number of ≥ 1nm radius MSPs present after sublimation of the cloud layer. Further modelling accounting for both the PMC microphysics and MSP coagulation is necessary to fully understand the effect of these competing coagulation processes on the overall distribution of MSPs in the mesosphere.

4.7 Summary and conclusions

In this chapter experiments on ice films within a UHV chamber were used to investigate the binding and reactivity of Mg and K on ice at temperatures of 110 – 140 K. Both metals were readily adsorbed under these conditions but were found not to co-desorb with the ice layer upon sublimation. Sputtering experiments showed that the metals are left as residuals after the ice sublimes. It is hypothesised here that PMCs could act as a secondary coagulation mechanism. The depletion of metal during a PMC event would lead to the formation of a population of large (≥ 1 nm radius) MSPs in the region of the cloud. Additionally, due to the differing reactions of the metals with the ice compared to reactions in the gas phase, the MSPs produced may be of different composition. The effects on the mesosphere of this process requires future modelling to account for cloud microphysics and competing MSP formation mechanisms. Energetic sputtering by 500 eV Ar^+ and Kr^+ of metal dosed ice layers also showed that Mg was unreactive, while

K formed KOH on the ice surface. These observations were supported by electronic structure calculations, with an Mg atom shown to be unreactive due to binding on a lone H_2O molecule at a surface irregularity, while an initially adsorbed K atom requires relatively little energy to insert into a surface H_2O to produce KOH and a dangling H atom. The calculations here also explain a previous observation that adsorbed Fe reacts on low-temperature ice to produce $Fe(OH)_2$.

5 Heterogeneous CO_2 ice nucleation on nanoparticles under Martian mesospheric conditions

Mesospheric CO_2 ice clouds are an unusual formation observed in the Martian atmosphere [*Montmessin et al.*, 2006]. These clouds are thought to be formed *via* deposition of CO_2, the main constituent of the atmosphere, following heterogeneous nucleation. MSPs have been suggested as a likely INP for these clouds [*Listowski et al.*, 2014]. This relatively newly observed cloud is poorly understood, with large uncertainties and unknowns regarding the microphysical formation process. The TRAPS instrument (detailed in chapter 2) was used at temperature and pressure conditions close to the mesosphere of Mars to investigate heterogeneous nucleation of CO_2. Results from experiments using TRAPS to investigate the nucleation and growth of CO_2 ice on nanoparticles (MSP analogue nanoparticles of Fe_xO_y and SiO_2) are presented here. A desorption energy of CO_2 on the nanoparticles was determined as $\Delta F_{des} = (18.5 \pm 0.2$ kJ mol$^{-1})$, while the contact parameter m was determined using CNT as 0.78 ± 0.02. Applying these CNT parameters to CO_2 clouds in the Martian mesosphere gave nucleation activation temperatures of 8 – 18 K (dependent on particle size) below the CO_2 saturation temperature. This suggests that lower temperatures are required to initiate cloud formation than previously thought.

5.1 Methodology

As stated in the contributions section, the work in this chapter was led by Dr Denis Duft and Mario Nachbar [*Duft et al.*, 2015; *Meinen et al.*, 2010]. This included the development and methodology of the TRAPS instrument and leading the raw data analysis for these experiments. The TRAPS instrument used in this study was detailed in chapter 2, with the methods for a typical experiment looking at CO_2 deposition on nanoparticles detailed here.

First, a population of nanoparticles of either Fe_xO_y or SiO_2 was generated in a 3.3 slm flow of He and O_2 by using a suite of precursor flows, in combination with a microwave plasma particle source within the NPS. This formed spherical, compact and singly charged particles with typical radii of 2 – 4 nm, depending on the vapour pressure of the precursors [*Giesen et al.*, 2005]. The particle flow (60 mbar) was then transferred into a vacuum chamber (10^{-3} mbar) using differential pumping in combination with the FLO and ADL. The charged particles were controlled using ion guides and quadrupole deflectors to transfer the particles to the MICE (see chapter 2 for more detail on the MICE). Typically 10^7 particles were introduced to the MICE in 1 s, where the particle temperature (T_{part}) and supersaturation was held constant (e.g. $T_{part} = 69.44 \pm 0.4$ K and $S = 567 \pm 142$) during the experimental timescale (typically 140 s). The associated errors are caused by the slight temperature gradient (0.1 K) across the length of the MICE. Deposition of CO_2 occurred on the nanoparticles if supersaturation in the MICE was sufficient. The deposition rate of CO_2 was probed in each experiment by extracting a fraction of the total particle population (approximately 10^5 particles every 6 s) at time intervals relative to the

particles residence time in the MICE. The extracted particles were assumed to be representative of the total particle population due to the relatively homogeneous temperature and saturation conditions within the MICE. These extracted particles were then transferred to a TOF-MS to evaluate the time dependent growth of CO_2 ice on the particles. A TOF-MS accelerates ions in relation to their mass to charge ratio, with heavier ions travelling slower and taking longer to reach the detector compared to lighter or multiply charged ions. The time-of-flight spectra can therefore be used to evaluate the added mass of the CO_2 deposited on the initially bare nanoparticles as a function of residence time in the MICE (knowing the initial particle mass). This was achieved by fitting the recorded particle time-of-flight spectra with a Gauss curve. The peak of the mass for the Gaussian distribution was determined as the modal particle mass with 1σ of the fit as the uncertainty. In the following section, an example of the particle mass distributions for three experiments on SiO_2 nanoparticles is used to illustrate CO_2 deposition and growth under different conditions.

The full temperature range accessible to the MICE in this study was 62 - 73 K. This was limited by the rapid loss of CO_2 ice from the warm walls of the MICE at higher temperatures. The upper limit of 73 K is close to the conditions where CO_2 clouds have been observed in the Martian mesosphere (75 -100 K) [*Montmessin et al.*, 2006]. The CO_2 pressure in the MICE (10^{-3} mbar) satisfactorily reproduces typical mesospheric conditions observed on Mars for altitudes of approximately 80 km [*Forget et al.*, 2009].

5.2 CO_2 adsorption, nucleation and growth

Figure 5.1 shows a series of measurements of CO_2 nucleation and growth on 2.5 nm radius SiO_2 particles. The CO_2 concentration in these three experiments was held constant at 10^9 cm^{-3} while the T_{part} was altered. Lowering the T_{part} therefore increased the supersaturation that the particles were exposed to. The mass of the bare SiO_2 particles (black dashed line) corresponds to a particle distribution exposed to conditions in the MICE where CO_2 deposition did not occur. Any additional mass above this line is therefore attributed to uptake of the CO_2 atmosphere within MICE. Lowering the T_{part} and therefore increasing the supersaturation led to three distinct types of CO_2 deposition (shown by [a], [b] and [c]). Curve [a] shows a situation where the nanoparticles were exposed to sufficient supersaturation to cause adsorption of CO_2 on the SiO_2 (S = 900) but not high enough to overcome the energy barrier to nucleation. With increasing exposure time to supersaturated conditions the number of CO_2 molecules adsorbed increases (exponential growth), before reaching an equilibrium. At this equilibrium point the adsorbing and desorbing flux of CO_2 from the SiO_2 particle surface is assumed to be the same, observed as a plateau in particle mass. This relationship is used to evaluate an important parameter in CNT, the ΔF_{des} of CO_2 on the nanoparticles, calculated in section 5.3. At a slightly lower temperature (66.4 K) shown in curve [b], the supersaturation is high enough (S = 2100) to overcome the energy barrier to nucleation. Growth can be seen to occur exponentially until it diverges from adsorption growth at a residence time of approximately 67 s. This divergence from adsorption growth to linear rapid growth is interpreted as the point of nucleation. This

was used to calculate another crucial parameter in CNT, *m*, in section 5.4. Finally, curve [c] at a further decreased T_{part} (64 K) and significantly increased supersaturation (S = 11500) produces a high nucleation rate, with rapid linear growth from the onset of observation. This differing deposition behaviour over < 3 K highlights the steep temperature dependence of CO_2 nucleation on these nanoparticles.

Note that as well as the three experiments shown in Figure 5.1, many experiments were done on SiO_2 and Fe_xO_y over a range of T_{part} and supersaturation conditions. For determining the ΔF_{des} of CO_2 on the nanoparticles in section 5.3 and for the *m* determination in section 5.4 a total of 142 experiments were undertaken. See *Nachbar et al.* [2016b] for a comprehensive table of all the experiments carried out for analysis.

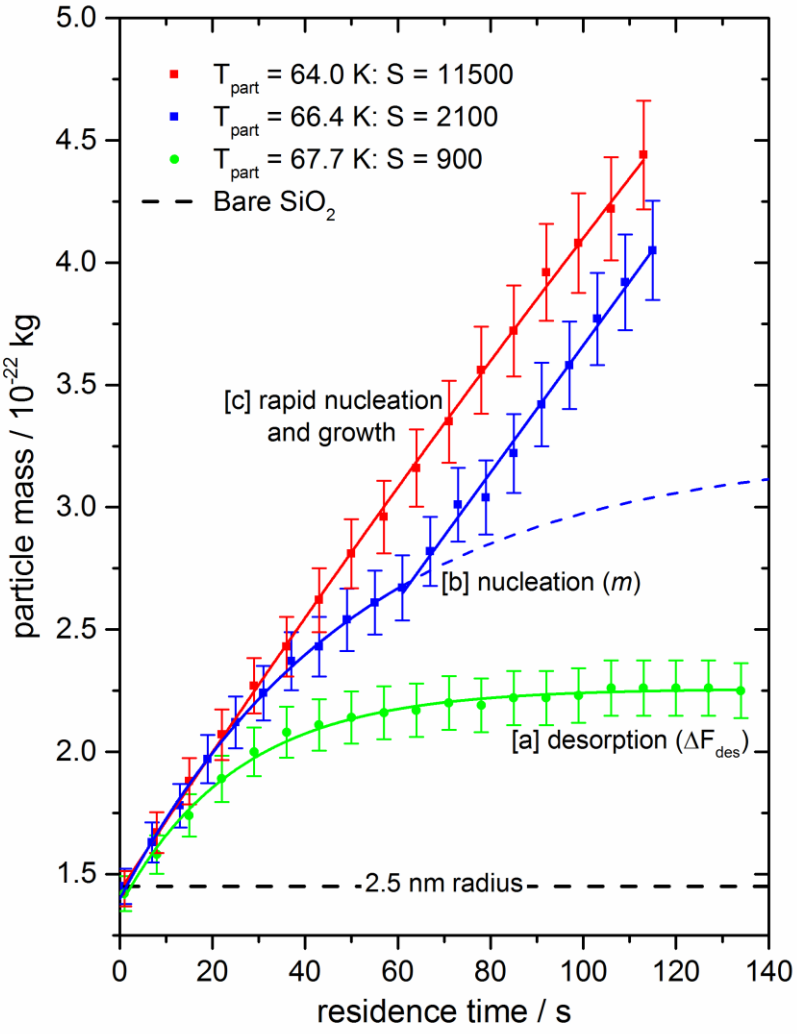

Figure 5.1 Particle mass against residence time in the MICE for a set of experiments of CO_2 deposition on 2.5 nm radius SiO_2 particles. Different growth regimes are shown for adsorption (curve [a]) used to determine the ΔF_{des}, delayed nucleation and growth (curve [b]) used to determine the m and also rapid initial nucleation and growth (curve [c]). The error bars relate to the standard deviation of the measured time-of-flight spectra.

5.3 Desorption energy of CO_2 on SiO_2 and Fe_xO_y

Determination of the ΔF_{des} for CO_2 on the SiO_2 and Fe_xO_y used in this study is necessary for accurately calculating the surface monomer coverage of CO_2, $c_{1,s}$ on an INP under atmospheric conditions. $c_{1,s}$ is a variable within the CNT theory approach to heterogeneous nucleation (see Equation 1.1 in section 1.3). The $c_{1,s}$ on the surface of an INP is calculated from the incoming and outgoing flux of CO_2 molecules by assuming a steady state, where the outgoing flux is dependent on the ΔF_{des}. $c_{1,s}$ is shown as:

$$c_{1,s} = \frac{p_{CO_2}}{\upsilon\sqrt{2\pi m_{CO_2} kT_{part}}} \cdot exp\left(\frac{\Delta F_{des}}{kT_{part}}\right) \tag{5.1}$$

where υ is the vibrational frequency of a CO_2 molecule on the surface of the INP (2.9×10^{12} s^{-1} taken from *Sandford and Allamandola* [1990]), p_{CO_2} is the CO_2 vapor pressure and m_{CO_2} is the mass of a CO_2 molecule. It is important to determine the ΔF_{des} for both SiO_2 and Fe_xO_y as $c_{1,s}$ affects the nucleation rate with a $c_{1,s}^2$ dependency.

Experiments using SiO_2 and Fe_xO_y nanoparticles that exhibit adsorption growth behaviour similar to that seen in curve [a] of Figure 5.1 were used to determine the ΔF_{des}. In the case of curve [a] the mass of approximately 1200 CO_2 molecules was added to the bare SiO_2 particle. Making the assumption of sub-monolayer CO_2 coverage the $c_{1,s}$ was calculated. The $c_{1,s}$ was then divided by the gas phase CO_2 concentration and, knowing the T_{part}, the only unknown variable in Equation 5.1 was the ΔF_{des}. Equation 5.1 was fitted using a non-linear least squares method known as the Levenberg-Marquardt algorithm for a range of T_{part} (and therefore a range of $c_{1,s}$) to determine

ΔF_{des}. The same fitting was done for the upper and lower limits of the normalized $c_{1,s}$ values to determine the error. This gave a ΔF_{des} of 18.43 ± 0.15 kJ mol^{-1} and 18.52 ± 0.15 kJ mol^{-1} for CO_2 on Fe_xO_y and SiO_2 respectively. The ΔF_{des} for is substrate specific. However, in this case the ΔF_{des} of both materials agree within error, so a common value is used in this study of 18.5 ± 0.2 kJ mol^{-1}.

5.4 Contact parameter determination

The surface diffusion approach of CNT was used to evaluate *m* and is described in detail in chapter 1. Briefly, CNT assumes that adsorbed CO_2 molecules diffuse on the INP surface. These CO_2 molecules can then collide and combine to form clusters, which could reach the critical size to initiate nucleation. *m* relates to the contact angle of the nucleating phase on the particle surface ($m = \cos\theta$) (see Figure 1.10) and is a measure of the specific nucleating ability of an INP, reducing the free energy barrier to nucleation (ΔF_{het}) (Equation 1.2).

A set of experiments using a range of conditions for both SiO_2 and Fe_xO_y nanoparticles that produced growth similar to that seen in curve [b] in Figure 5.1 was used to determine *m* for nucleation of CO_2 on nanoparticles in the MICE. This involved experiments with particles of initial radii of 2.4 – 3.1 nm for SiO_2 and 1.9 – 2.1 nm for Fe_xO_y, particle temperatures of 64 – 73 K and CO_2 concentrations from 8 x 10^8 cm^{-3} to 4 x 10^{11} cm^{-3} (the full experiment list can be found in *Nachbar et al.* [2016b]).

The $c_{1,s}$ (Equation 5.1) used in CNT assumes a steady state equilibrium. The steady state assumption of the growth plateau in ΔF_{des} experiments is not

observed in these experiments. This is because the particles continue to adsorb more CO_2 molecules as a function of the time exposed to supersaturated vapour in the MICE. The nucleation rate is time dependent, increasing during adsorption until either the critical concentration to initiate nucleation (rapid growth in curve [b]) or the equilibrium surface concentration (plateau in curve [a]) is reached. In the case of curve [a], the nucleation rate is too low to initiate nucleation on enough particles to be observable on experimental timescales (140 s). The lower temperature of curve [b] means a higher equilibrium $c_{1,s}$ (see Equation 5.1). Increased exponential growth compared to curve [a] is apparent due to the higher equilibrium $c_{1,s}$. At a residence time of approximately 67 s the exponential growth changes to rapid linear growth, interpreted as the point of nucleation. The surface concentration of CO_2 at this transition point for each experiment is therefore determined as the critical concentration for nucleation.

No significant broadening of the particle mass distributions was observed during nucleation. This suggests that nucleation of the majority of the particles occurred within a single experimental time step (6 s). The nucleation rate at the critical surface concentration of CO_2 is therefore estimated as 1/6 times this value. Combining these variables with the INP radius, T_{part}, CO_2 concentration and saturation ratio (in the MICE), Equation 1.1 can be numerically solved to determine *m*, which is rather insensitive to the nucleation rate. One order of magnitude change in nucleation rate produces only a 1% change of *m*. The error associated with this order of magnitude change is combined with the errors of the other variables to give an overall error in the *m* value. As the nucleation is extremely temperature dependent the main error source in *m* is due to the ± 0.4 K uncertainty in the

temperature of the MICE. The determined *m* values are shown in Figure 5.2. A lack of temperature dependence on *m* is apparent over the temperature range 64 – 73 K and there is no significant difference within error of the *m* determined for the different INPs (SiO_2 and Fe_xO_y). Therefore an overall mean value for the *m* of 0.78 ± 0.02 was determined.

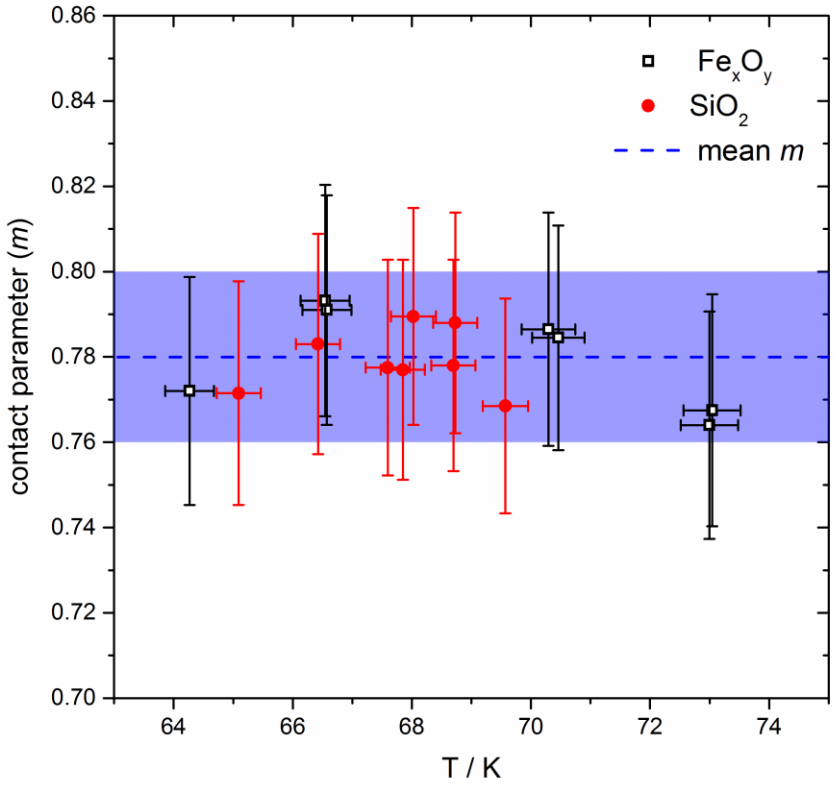

Figure 5.2: The *m* with particle temperature for Fe_xO_y particles and SiO_2 particles. The dashed line and shaded area represent the determined mean value of 0.78 ± 0.02.

5.5 CO_2 nucleation in the Martian mesosphere

The mean value of *m* (0.78 ± 0.02) was used in conjunction with the ΔF_{des} (18.5 ± 0.2 kJ mol^{-1}) to evaluate the nucleation rates of CO_2 under representative Martian mesospheric conditions. This extrapolation makes the assumption that the *m* and ΔF_{des} values are independent of T_{part}. A CO_2 ice density of 1.5 g cm^{-3} was used in this section taken from *Luna et al.* [2009]. The use of this density value was valid for evaluation of the experimental data at temperatures below 80 K. Use of this density above 80 K is investigated in chapter 6.

5.5.1 CO_2 nucleation rates using a fixed atmospheric density

Initially a fixed CO_2 concentration of 1 x 10^{14} cm^{-3} was used to evaluate nucleation rates, which corresponds to a mesospheric altitude of approximately 70 km [*Forget et al.*, 2009]. Nucleation rates as a function of temperature were calculated for a range of INP sizes (1 – 30 nm radius) and are shown in Figure 5.3. The nucleation rate is extremely temperature dependent, increasing by 3 orders of magnitude for a 1 K reduction in temperature. It is also significantly dependent on the size of the INP, for 2 – 30 nm radii INP a 13 K shift in the nucleation rate profile is apparent. At larger INP radii the effect is minimal as increasing the INP radii from 30 - 200 nm only shifts the nucleation temperature by 1 K.

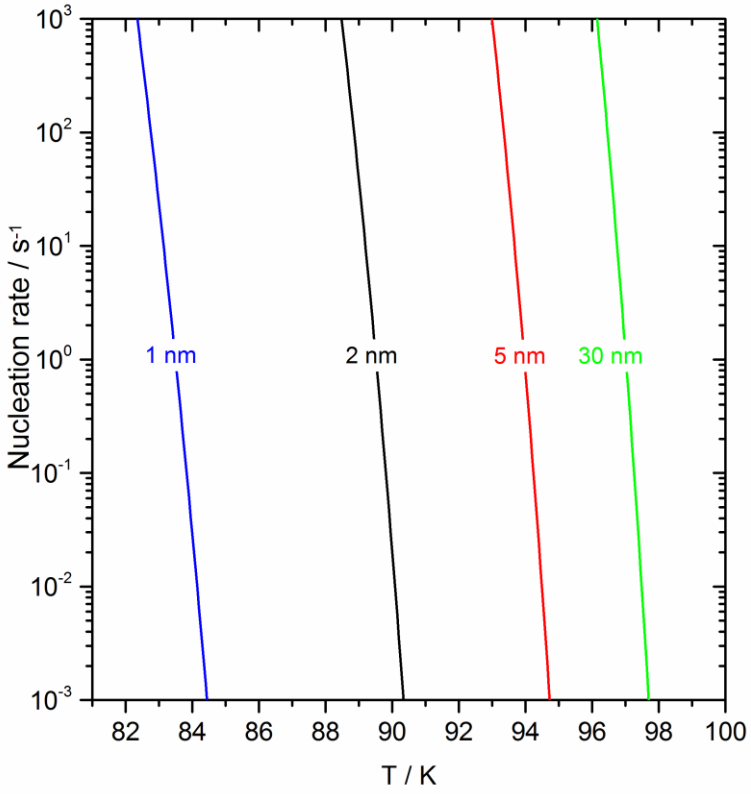

Figure 5.3: Nucleation rates for different INP sizes (1 – 30 nm radius) using CNT as a function of temperature. A fixed CO_2 concentration of 1×10^{14} cm^{-3} was used here. The values of ΔF_{des} and m were determined in sections 5.2 and 5.4 respectively.

5.5.2 CO_2 nucleation rates using a variable atmospheric density

The use of a single atmospheric density provides an illustration of the dependence of nucleation rate on temperature and particle size. The calculated nucleation parameters are now instead applied to an atmospheric density profile in order to relate directly to atmospheric observations. Nucleation rates were calculated using a fit to the overall atmospheric density of the entry profile of the Mars Pathfinder from *Magalhães et al.* [1999], assuming a 95% mixing ratio for CO_2 [*Mahaffy et al.*, 2013].

Due to the steep temperature dependence of the nucleation observed in Figure 5.3, at each particle size a characteristic temperature is apparent for

nucleation. The cold pockets in which mesospheric CO_2 clouds form have a lifetime of a few hours [*Listowski et al.*, 2014]. Here it is assumed that in the presence of abundant INPs a nucleation rate of 0.01 s^{-1} is sufficient to form a cloud on this timescale. The temperature at which this nucleation threshold is reached is referred to here as the Nucleation Activation Temperature (NAT).

The altitude dependent NATs for 2 nm and 30 nm radius INPs in the Martian atmosphere is shown in Figure 5.4. The Pathfinder temperature profile from *Magalhães et al.* [1999] includes temperatures up to 5 K below the saturation temperature (T_{sat}) (where S = 1) at an altitude of 80 km. In early modelling studies of CO_2 cloud this would have been deemed sufficient to activate cloud formation [*Forget et al.*, 1998]. However, the predicted NATs in this study are 8 – 18 K below the T_{sat}, suggesting CO_2 clouds would not have formed under these conditions. Significant temperature depression below T_{sat} is therefore necessary to form CO_2 clouds in the Martian mesosphere when using this parameterization. The temperature depression required to facilitate cloud formation can be seen in the satellite temperature profile taken from *Montmessin et al.* [2006] of occ #1205. A cold pocket is present at an altitude of approximately 96 km, where temperatures dropped up to 20 K below the T_{sat}. These conditions are predicted to lead to cloud formation on INPs with radii ≥ 2 nm. This prediction is corroborated by the observation of a detached layer at altitudes just below the temperature minimum (approximately 75 – 93 km altitude). This detached layer was likely caused by nucleation of CO_2 and subsequent growth and sedimentation of the CO_2 ice particles from the cold pocket above.

It should be noted that the problem of predicting cloud formation in reality is more complex than the simple comparison shown here, requiring modelling that includes microphysical processes. Cloud formation is still dependent on the availability of sufficiently active INP and sufficient exposure time to supersaturated conditions. This is highlighted by observations in certain cases of temperatures up to 20 K below T_{sat} in the absence of CO_2 cloud [*Montmessin et al.*, 2011]. It would be advantageous in the future to have observations of particle size distributions in the mesosphere, given the high variability of nucleation rates depending on particle size.

The NATs were recalculated using the *m* of 0.95 taken from *Glandorf et al.* [2002]. This comparatively higher *m* produces NATs 5 - 7 K warmer. Several major differences between this study and the work of *Glandorf et al.* [2002] could account for the difference in reported *m* and subsequently shifted NATs. Firstly the temperature range studied by *Glandorf et al.* [2002] was 130 -140 K, significantly higher than the 64 – 73 K investigated in this study. Temperature dependence of *m* has been previously observed for experiments looking at H_2O ice nucleation on Mars [*Trainer et al.*, 2009]. No temperature dependence in *m* was observed over the individual temperature range in both studies (approximately 10 K) but a gradient in *m* could be apparent over the full 76 K temperature range. Finally and possibly most importantly, *Glandorf et al.* [2002] investigated CO_2 nucleation on planar H_2O instead of on SiO_2 and Fe_xO_y nanoparticles. This will lead to the availability of different nucleation sites that could be less efficient in the case of this study.

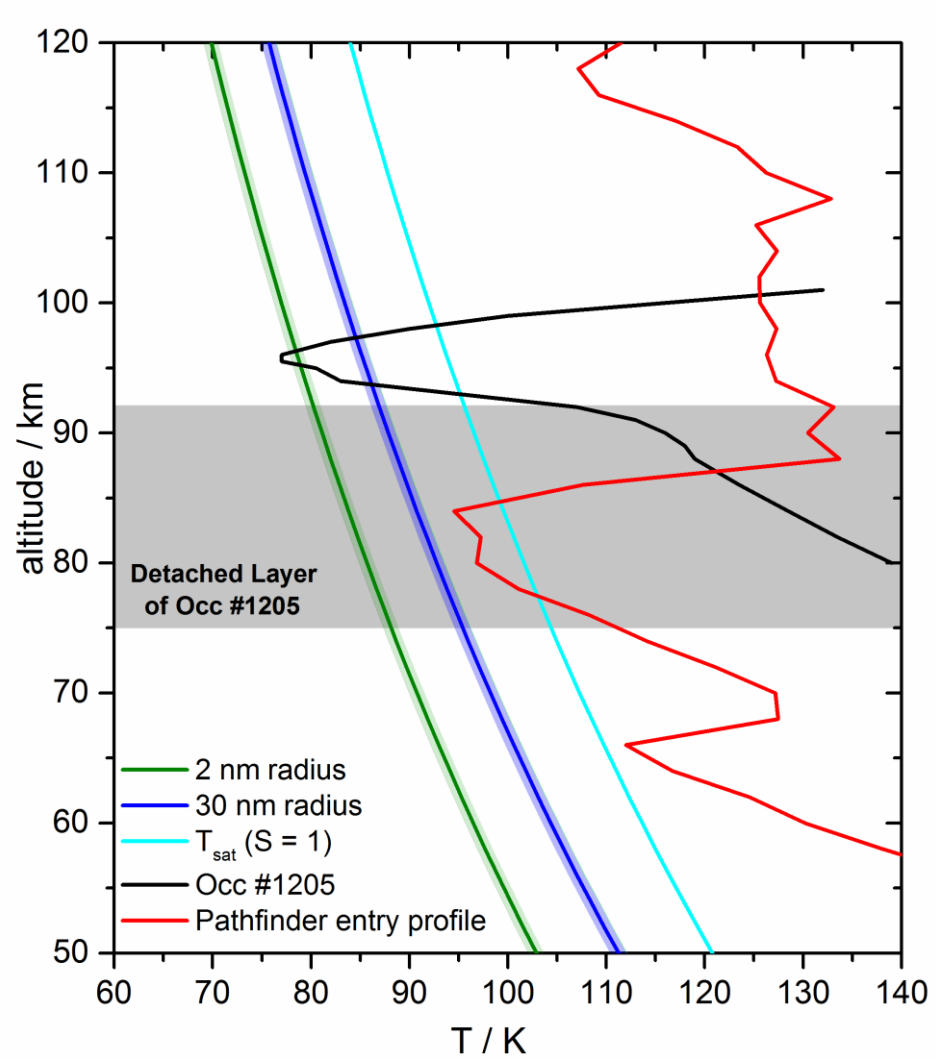

Figure 5.4: Calculated NAT (nucleation rate = 0.01 s^{-1}) with altitude for a 2 nm (green curve) and 30 nm INP (cyan curve), the shaded area is the uncertainty due to the error in *m* and $\Delta F_{des.}$ For comparison, the T_{sat} is included (blue curve, where S = 1). Two measured temperature profiles, the Pathfinder entry profile [*Magalhães et al.*, 1999] and orbit 1205 (occ. #1205) of *Montmessin et al.* [2006], are shown for comparison. A detached layer observed during the measurement of occ #1205 (attributed here to CO_2 cloud formation) is shown by the grey shaded area.

5.5.3 INPs in the Martian mesosphere

Whatever the cause of the differences in *m,* it is also worth evaluating which parameterization is most applicable to the Martian mesosphere. The likelihood of H_2O INPs for mesospheric CO_2 cloud formation was questioned previously in section 1.2.3. Due to the lack of H_2O supersaturation in the mesosphere (altitudes above 50 km) during CO_2 cloud season, H_2O ice is an unlikely nucleation pathway [*Maltagliati et al.*, 2013]. This suggests that the parameterization of *Glandorf et al.* [2002] isn't applicable to typical mesospheric CO_2 clouds. MDPs were suggested in section 1.2.3 as a possible INP source, when the second dust maxima (45 – 65 km) and mesospheric CO_2 cloud altitude range (60 – 80 km) overlap during the daytime [*Guzewich et al.*, 2013; *Montmessin et al.*, 2006]. The measurements in this study of *m* could be applied to MDPs. Given the comparable nucleating efficiency (within error) in this study of the SiO_2 and Fe_xO_y and the comparable ΔF_{des} (18.5 ± 0.2 kJ mol^{-1}) to that of an MDP analogue palagonite (19.6 kJ mol^{-1}) [*Zent and Quinn*, 1995]. However, in order to substantiate this hypothesis, studies on more INPs with differing composition (including MDP analogues) should be carried out in the future to determine possible variability in *m*. MSPs are thought to be the likely source of INPs for these high altitude clouds, as the presence of MDPs alone can't reproduce observed mesospheric CO_2 clouds [*Listowski et al.*, 2014]. Given the use of MSP analogues in this study, this parameterization is recommended for application in future modelling of mesospheric CO_2 ice clouds.

5.6 Summary and conclusions

A novel experimental system (TRAPS) has been employed to investigate the nucleation of CO_2 on nanoparticles of SiO_2 and Fe_xO_y under conditions close to those observed in the Martian mesosphere. Distinct adsorption and nucleation growth regimes on these two analogues were observed and used respectively to determine a mean ΔF_{des} of 18.5 ± 0.2 kJ mol^{-1} and m of 0.78 ± 0.02. Applying these CNT parameters to CO_2 clouds in the Martian mesosphere led to NATs 8 – 18 K (dependent on INP size) below the T_{sat}. This suggests that a larger temperature depression below T_{sat} than previously thought is needed to form clouds. The nucleation parameters included here are recommended for use in future modelling studies of the mesosphere.

6 CO_2 ice structure and density under Martian atmospheric conditions

Clouds composed of CO_2 ice form throughout the Martian atmosphere as detailed in chapter 1. Mesospheric CO_2 ice clouds are thought to form at temperatures below 100 K (investigated in chapter 5) [*Listowski et al.*, 2014]. Lower altitude CO_2 ice clouds in the wintertime polar regions form up to around 145 K and are related to the build-up of the polar ice caps [*Hayne et al.*, 2012]. However, the crystal structure and related fundamental properties of CO_2 ice under Martian conditions are poorly characterised. Here, XRD measurements of CO_2 ice are presented, grown *via* deposition from the vapour phase under temperature and pressure conditions analogous to the Martian mesosphere. A crystalline cubic structure was determined, consistent with the low-pressure polymorph (CO_2-I, space group *Pa*-3 (No. 205)) for CO_2 deposited at temperatures of 80 - 130 K and pressures of 0.01 – 1 mbar. The thermal expansion of CO_2 was determined across 80 – 130 K that allowed for a fit of CO_2 ice density measurements across a larger temperature range (80 – 195 K) when combined with literature data (CO_2 density in $g\ cm^{-3} = 1.72391 - 2.53x10^{-4}\ T - 2.87x10^{-6}\ T^2$). Temperature-dependent CO_2 density values were used to estimate sedimentation velocities and heterogeneous ice nucleation rates and is recommended for use in future studies of Martian clouds. The possible shape of CO_2 ice crystals in the Martian atmosphere was predicted and shows that a cubo-octahedron is the equilibrium shape. A range of shapes in the O_h point group is also possible, from cubes to octahedra.

6.1 Methodology

CO_2 ice crystal structure was examined on a temperature-controlled stage enclosed within an environmental chamber. This stage is probed using powder XRD. A description of the instrument, and detail of the XRD technique can be found in Chapter 2. In these experiments, CO_2 gas was either vapour deposited onto a flat substrate, or CO_2 in the form of powdered dry ice was placed in a sample holder and inserted into the chamber. This XRD instrument has been used previously to study vapour deposited H_2O ice [*Malkin et al.*, 2015; *Murray et al.*, 2015].

In a typical vapour-deposition experiment the environmental chamber was first pumped to a pressure of < $1x10^{-2}$ mbar to ensure minimal H_2O vapour contamination during cooling. The sample was then cooled from 300 K to 80 K at a rate of 20 K min^{-1}. At the deposition temperature a diffraction pattern was recorded (2θ = 20°- 50°) to ensure no contamination in the form of water ice frosting had occurred on the glass slide. For CO_2 vapour deposition, a flow of pure CO_2 gas (Air Products CO_2 purity 4.5) was administered directly into the chamber via a needle valve. The environmental chamber was kept at low pressures during deposition (0.01 - 1 mbar) using the vacuum pump and throttle valve. Low-resolution XRD patterns (2θ = 20°- 30°) were taken continuously during deposition until sufficient signal was observed. The system was then sealed to maintain the pressure and higher resolution XRD patterns with increments of 2θ = 0.0426° were obtained at 2θ = 20° - 50°. Experimental diffraction patterns were corrected against an Si standard, accounting for peak shifting due to sample height.

For experiments looking at the structure of dry ice, an indented aluminium sample holder without a borosilicate glass slide was used. Dry ice was ground using a pestle and mortar and packed into the sample holder under liquid N_2. A flow of dry Ar gas over the holder was used to minimise water ice contamination. Grinding was done in order to minimise the preferred orientation in the crystals. The environmental chamber was cooled to 80 K at vacuum in the absence of a sample holder and was flushed with dry N_2 before transferring the sample holder containing the dry ice into the chamber and promptly sealing it. XRD patterns were then taken across the scan range 2θ = 20° - 50°. XRD patterns of dry ice, and CO_2 ice deposited at 80 K and 110 K are shown in the following section in order to determine the crystal structure and temperature dependent properties of the ice.

6.2 Crystal structure of CO_2 ice deposited from vapour

Figure 6.1 shows diffraction patterns of typical vapour-deposited CO_2 ice at 80 K and 110 K, ground dry ice and a predicted pattern using known lattice parameters of CO_2-I with space group *Pa*-3 (taken from *de Smedt and Keesom* [1924]). The structure of CO_2-I is detailed in subsection 1.2.4 and is described by a single lattice parameter, due to its cubic structure. Experiments were carried out at pressures as low as 0.01 mbar, corresponding to a Martian atmospheric pressure where CO_2 clouds have been observed at altitudes of 60 - 65 km [*Forget et al.*, 2009; *Kleinbohl et al.*, 2009]. The vapour-deposited ice at 80 K displays distinct Bragg peaks associated with a crystalline structure, consistent with previous studies that suggest amorphous CO_2 ice only forms at temperatures below 50 K [*Souda*, 2006]. The Bragg peaks in the vapour-deposited and dry ice samples are at comparable 2θ angles to the Bragg peaks in the predicted pattern. However, the 200 peak at 33° is absent in the vapour-deposited material at 80 K and the relative peak intensities vary between the measured (80 K, 110 K and dry ice) and calculated pattern for an ideal powder.

In order to test if the diffraction pattern for the vapour-deposited ice was consistent with the CO_2-I phase it was necessary to use a Rietveld refinement method [*Rietveld*, 1969]. Initially, the whole powder pattern decomposition was performed following the *Pawley* [1981] method (using the software package TOPAS 4.2) in order to confirm a fit to the CO_2-I literature crystal structure and determine the lattice parameters. The fit to the diffraction pattern in Figure 6.1 shows that the ice generated via vapour

deposition has a structure consistent with standard CO_2-I but with preferred orientation.

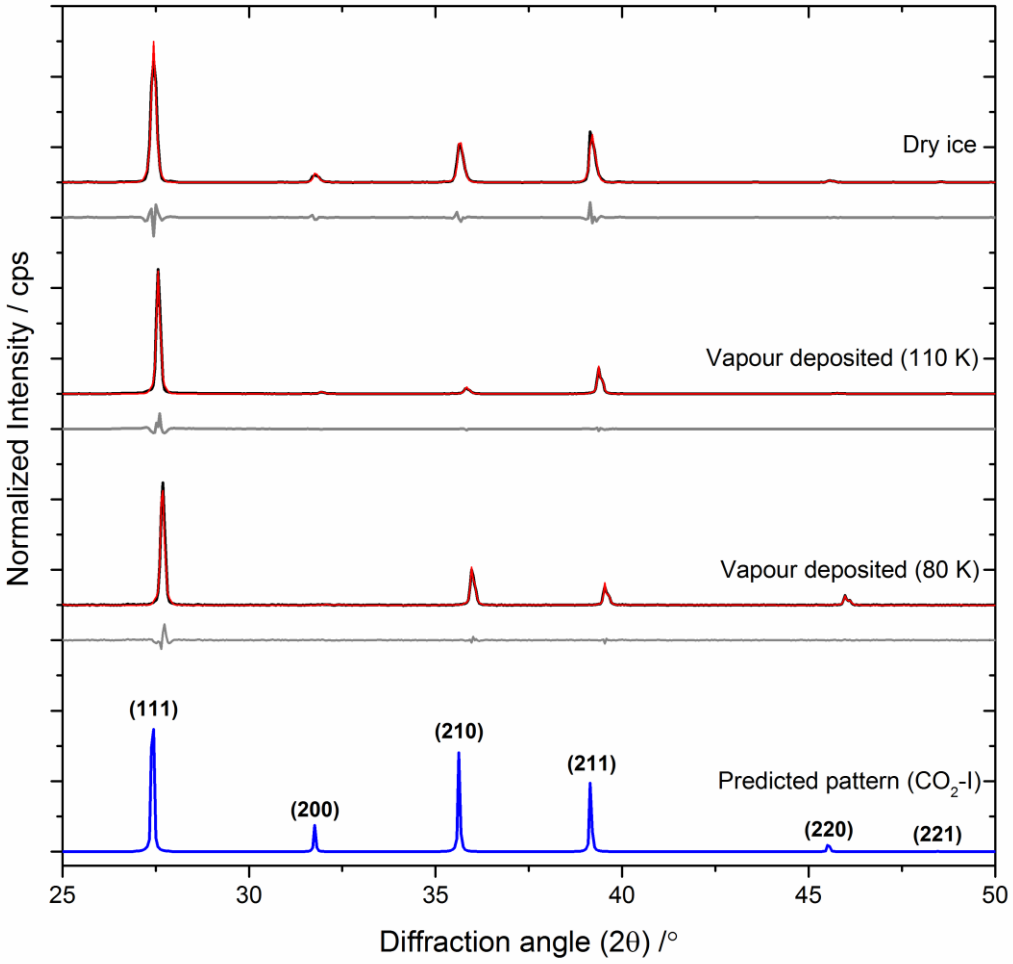

Figure 6.1: Background corrected and vertically offset experimental XRD patterns of a typical vapour-deposited CO_2 ice at 80 K and 110 K, ground dry ice and a calculated XRD pattern based on current crystal structure for CO_2-I [*de Smedt and Keesom*, 1924]. Profiles are normalised to the intensity of the 111 peak (2θ = ~27.5º). The TOPAS refinement of the vapour-deposited and dry ice CO_2 patterns (black lines) for CO_2-I using the *Pawley* [1981] method is indicated by the red lines. The grey line shows the residuals of the fits.

6.2.1 Preferred orientation in CO_2 ice

Preferred orientation in powder diffraction patterns arises whenever there is a non-random orientation of crystallites in a sample. In order to obtain a perfect powder pattern, crystallites must be both numerous and randomly orientated. This produces diffraction rings and is comparable to the powder XRD technique used here where the detector measures across a segment of the diffraction ring. In contrast, if a population of crystals all had identical crystallographic orientation, as might happen in epitaxial growth on a surface, all the diffracted X-rays would be concentrated into spots with each spot corresponding to a specific crystallographic plane. In the case of this situation, the powder XRD instrument would not produce a meaningful diffraction pattern. An intermediate situation exists in Figure 6.1 where the crystallites are partially ordered, which results in Bragg peaks which can either be more or less intense than those in the ideal powder pattern and sometimes be missing all together. The analysis presented in Figure 6.1 shows that patterns of the CO_2 ice grown from the vapour phase and the powdered dry ice sample are consistent with the standard CO_2-I phase with different degrees of preferred orientation.

In addition to using the *Pawley* [1981] refinement method, the XRD patterns of vapour-deposited CO_2-I were also refined using the *Le Bail et al.* [1988] method. Although both are least-squares refinements, the method developed by *Le Bail et al.* [1988] treats the diffraction patterns without the need for peak intensities (while other crystallographic parameters are known), which in this case are affected by preferred orientation. This simplified method is reasonable due to the lack of overlapping Bragg peaks.

The crystallographic properties calculated by both of these refinement methods agreed within error.

6.2.2 Temperature dependence of CO_2 ice structure

CO_2 ice layers deposited at 80 K and 110 K were warmed at 1 K min^{-1} with diffraction patterns taken at 5 K intervals. The temperature dependence of the unit cell parameters of CO_2-I deposited from the vapour at 80 K (80 - 120 K) and 110 K (110 – 130 K) was determined from this using the *Pawley* [1981] refinement method detailed in section 6.2 and is shown in Figure 6.2. The experiments in this study require a thin CO_2 film in good thermal contact, limiting the study to temperatures of ≤ 130 K because the ice film was lost to sublimation at higher temperatures. The length of the lattice parameter (and therefore unit cell volume) increases with temperature due to thermal expansion of the crystal lattice. Good agreement within error can be seen between the CO_2 ice deposited at different temperatures.

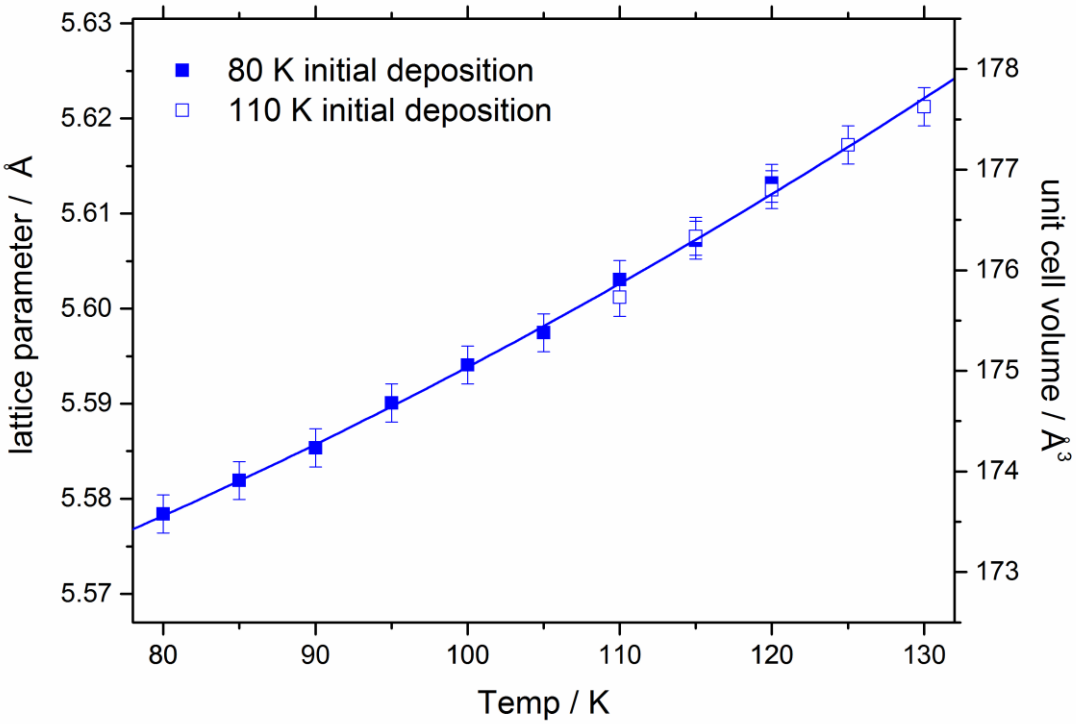

Figure 6.2: CO_2-I lattice parameters and unit cell volumes for deposition at 80 K and 110 K. The blue line indicates a polynomial fit to the dataset.

6.2.3 CO_2 ice density

The CO_2 ice density was calculated based on changes in the unit cell volume with temperature. The CO_2 ice densities as well as the lattice parameters from Figure 6.2 are tabulated in Table 3. The densities from this study and other literature values are shown in Figure 6.3. A larger density (1.684 ± 0.002 g cm^{-3} at 80 K) is reported here when compared to the corrected CO_2 density values of *Keesom and Kohler* [1934a] (where the lattice parameter values were converted from kX to Å (where 1 kX = 1.002 Å [*Bragg*, 1947] by *Curzon* [1972]). While one density value at 90 K from *Maass and Barnes* [1926] is in good agreement with the present study, the variability in the values determined when repeated (1.663 - 1.674 g cm^{-3} at

90 K) compared to the higher temperature densities (≥ 138 K) suggests errors in their method when applied to these low temperatures. It should be noted that in this study the density determined from temperature repeats in different experiments agreed within error. The higher temperature values from *Maass and Barnes* [1926] follow a similar temperature dependence to the lower temperature values determined in this study. While a lattice parameter for CO_2 ice at 150 K based on a single crystal refinement by *Simon and Peters* [1980], when converted to a density, is in significant disagreement with this study and other literature density values (it should be noted that no temperature uncertainties are given by *Simon and Peters* [1980]).

Table 3: Summary of CO_2-I crystal structure parameters with temperature, determined from diffraction patterns of vapour deposited CO_2 ice.

Temperature / K	Lattice parameter (± 0.002) / Å	Unit cell volume (±0.19) / Å^3	Density (± 0.002) / g cm^{-3}
80 K initial deposition			
80	5.578	173.554	1.684
85	5.582	173.928	1.681
90	5.585	174.209	1.678
95	5.59	174.677	1.673
100	5.594	175.052	1.67
105	5.597	175.334	1.667
110	5.603	175.898	1.662
115	5.607	176.275	1.658
120	5.613	176.842	1.653
110 K initial deposition			
110	5.601	175.71	1.663
115	5.608	176.37	1.657
120	5.613	176.842	1.653
125	5.617	177.22	1.649
130	5.621	177.599	1.646

In general the density profile can be seen to decrease with increasing temperature, consistent with the thermal expansion of CO_2 ice. A second-order polynomial fit through the data in this study (80 – 130 K) and the *Maass and Barnes* [1926] data at temperatures ≥ 138 K yields the following equation of state for the CO_2 ice density (in units of g cm^{-3}) at 1x10^{-2} mbar:

$$\mathrm{CO_2\ density\ (80-195\ K)} = 1.72391 - 2.53 \times 10^{-4} T - 2.87 \times 10^{-6}\ T^2 \quad (6.1)$$

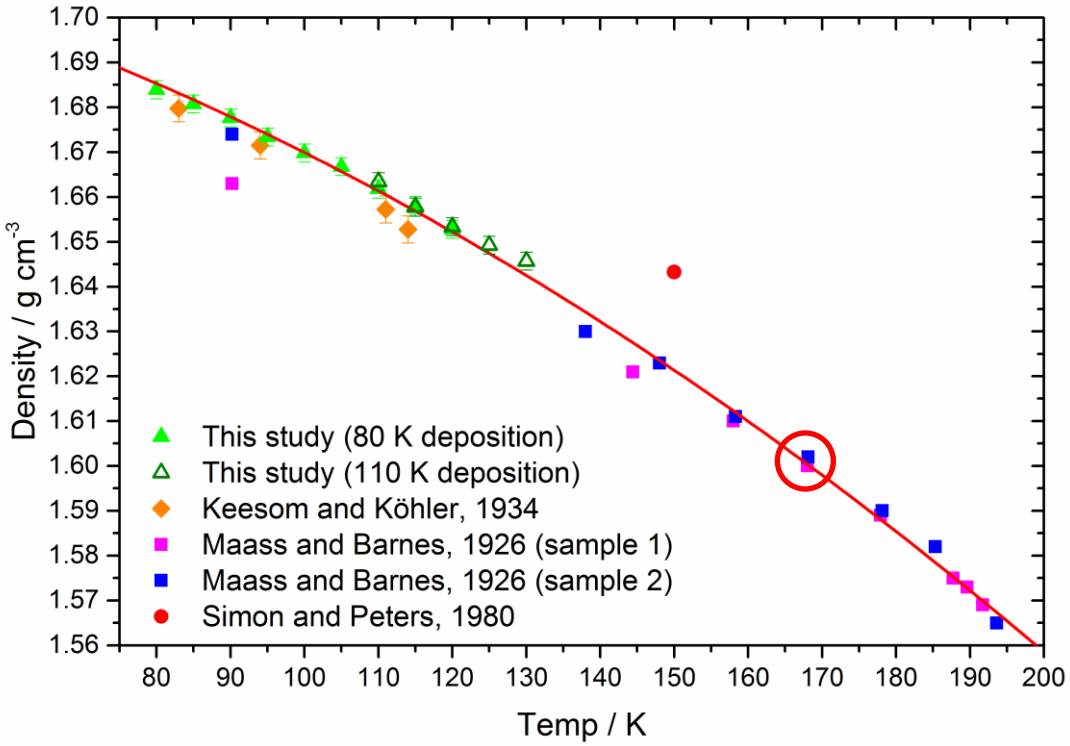

Figure 6.3: CO_2 density values obtained from the lattice constants determined in this study as well as comparisons with literature values [*Keesom and Kohler*, 1934a; *Maass and Barnes*, 1926; *Simon and Peters*, 1980]. The 2nd order polynomial fit is represented by the red line. The red circle indicates the literature value typically used in Martian modelling of 1.6 g cm^{-3}.

6.2.4 Linear thermal expansion of CO_2-I

Using the temperature-dependent polynomial fit to the CO_2 density across 80 – 195 K, linear thermal expansion coefficients for CO_2-I were calculated from the volume expansivity coefficient (β) given by:

$$\beta = (1/V)(dV/dT) \qquad (6.2)$$

where the linear expansivity coefficient (α) is then (1/3)β. The thermal expansion of CO_2 shown in Figure 6.4 is compared to hexagonal H_2O ice (H_2O-I_h) over the same temperature range [*Röttger et al.*, 1994]. The thermal expansion of CO_2-I shows a positive gradient and doubles over the temperature range (80 – 195 K), much larger compared to H_2O ice. This rapid expansion for CO_2-I highlights the need to use temperature-dependent parameters when modelling CO_2 ice.

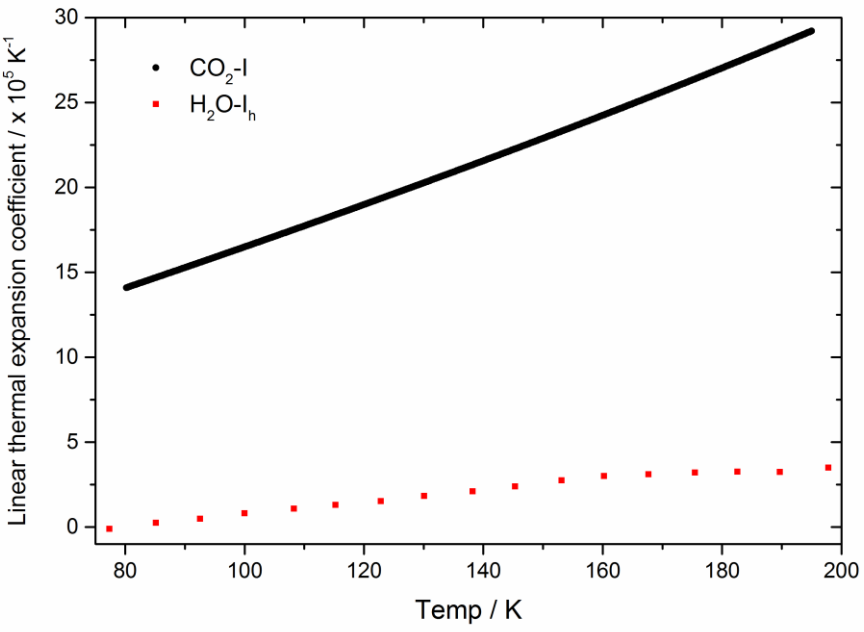

Figure 6.4: Linear thermal expansion coefficients (x10^5) calculated for CO_2-I from Equation 6.1 and for H_2O-I_h using data reproduced from *Röttger et al.* [1994].

6.3 Mesospheric effects of changing CO_2 ice parameters

In this section the effect of crystal structure and density on the microphysics of mesospheric CO_2 clouds on Mars is explored. The impact of using the temperature-dependent density data from this study is compared to the previously used values in the literature of 1.5 g cm^{-3} and 1.6 g cm^{-3} taken from *Luna et al.* [2009] and *Wood* [1999] [*Listowski et al.*, 2013; *Listowski et al.*, 2014; *Maattanen et al.*, 2005]. It is worth noting that the often used literature value of 1.6 g cm^{-3} (highlighted in a red circle in Figure 6.3) was measured at 168 K. This is ≥ 50 K warmer than T_{sat} is observed in the Martian mesosphere.

6.3.1 Sedimentation of CO_2 ice particles

Certain CO_2 ice particle variables relevant to mesospheric clouds are linearly dependent on CO_2 ice density. This is illustrated, for example, by the Stokes sedimentation velocity (v_{sed}) of CO_2 ice particles as shown by *Brasseur and Solomon* [2006] as:

$$v_{sed} = \frac{2\rho g r^2 C_c}{9\eta} \qquad (6.3)$$

where g is the gravitational constant for Mars (3.7 m s^{-2}), r the ice particle radius, η the viscosity of CO_2 gas and ρ the density of the CO_2 ice. C_c is the Cunningham slip factor, which corrects for the low atmospheric densities on Mars and therefore the transition to the free molecular regime. Taken from *Listowski et al.* [2014] C_c is determined as $1 + Kn[1.246 + 0.42 \exp(-0.87/Kn)]$, where Kn is the Knudsen number, defined as the ratio of the mean free path over r. Using Equation 6.3 the sedimentation velocities of particles with a range of CO_2 ice densities (where

1.684 g cm^{-3} valid at 80 K is taken from Equation 6.1) were calculated as a function of particle radius. An extreme atmospheric temperature profile was used, consistent with the negative temperature perturbation that would be caused by a large amplitude gravity wave at approximately 80 km altitude ($2x10^{-4}$ mbar and 80 K) [*Kleinbohl et al.*, 2009; *Listowski et al.*, 2014; *Montmessin et al.*, 2006]. Higher sedimentation velocities result from the higher density value found in this study, with the linear dependence of density on sedimentation causing a 5 % increase in sedimentation velocity (1.6 g cm^{-3} compared to 1.684 g cm^{-3}). For example, under these conditions a 500 nm radius CO_2 ice particle falls an extra 1.6 km h^{-1} when the CO_2 ice density is increased from 1.6 to 1.684 g cm^{-3}. Extrapolating this to a population of CO_2 ice particles within a mesospheric cloud inside a cold pocket, unperturbed sedimentation would lead to a more rapid decrease in altitude of a detached CO_2 ice layer. This could result in shorter cloud lifetimes as the crystals fall into a warmer region below the cold pocket, causing rapid evaporation of the CO_2 ice particles [*Listowski et al.*, 2014]. In the case of tropospheric CO_2 clouds (10 – 100 µm particle radii) forming at temperatures ≤ 145 K, a density value higher than the current literature (1.6 g cm^{-3}) would also be required. Compared to current predictions, this would increase the precipitation rates of CO_2 ice particles from the cloud and hence affect the accumulation rate of CO_2 ice at the polar caps [*Hayne et al.*, 2014].

6.3.2 Nucleation of CO_2 ice particles

Certain CO_2 ice parameters related to mesospheric Martian cloud microphysics have a greater complexity in terms of the effect of changing density values when compared to the linear effect on sedimentation. An example is the mechanism through which cloud ice particles are formed. As discussed in section 1.2 and chapter 5, heterogeneous ice nucleation *via* deposition of CO_2, in which the energy barrier to nucleation is reduced by the presence of an INP, is thought to be the likely nucleation pathway. Heterogeneous nucleation is therefore applied here and is described using the same CNT and conditions as Chapter 5 (see section 1.3).

Heterogeneous nucleation rates of CO_2 on small INP analogous to meteoric material at high altitudes (1 – 30 nm radius particles) are shown in Figure 6.5. This was determined using the same parameters as the nucleation rates in chapter 5 but with a range of CO_2 ice densities. Changes in CO_2 density alter the calculated values of the critical cluster, the number of molecules in the critical cluster and ΔF_{het}, which then impacts on the overall determined nucleation rates. The effect of shifting density is highlighted by the steep temperature dependence of the nucleation rates. Using the new temperature-dependent fit determined in this study (Equation 6.1) instead of the fixed value of 1.6 g cm^{-3} causes an approximately three-orders of magnitude increase in nucleation rate (at 85 K for a 1 nm radius INP). The impact of this density change reduces with increasing particle size but nucleation rates on 30 nm radius INP still increase by 1 – 2 orders of magnitude. This increased nucleation rate reduces the extent of negative temperature perturbations below T_{sat} that would be required to initiate CO_2

cloud formation (shown in chapter 5). However, it should be noted that this effects modelling using the previous measurements of [*Glandorf et al.*, 2002] as well. The conclusions of Chapter 5 are therefore still valid, and combining the new m, ΔF_{des} and ice density still gives lower NATs than previously thought.

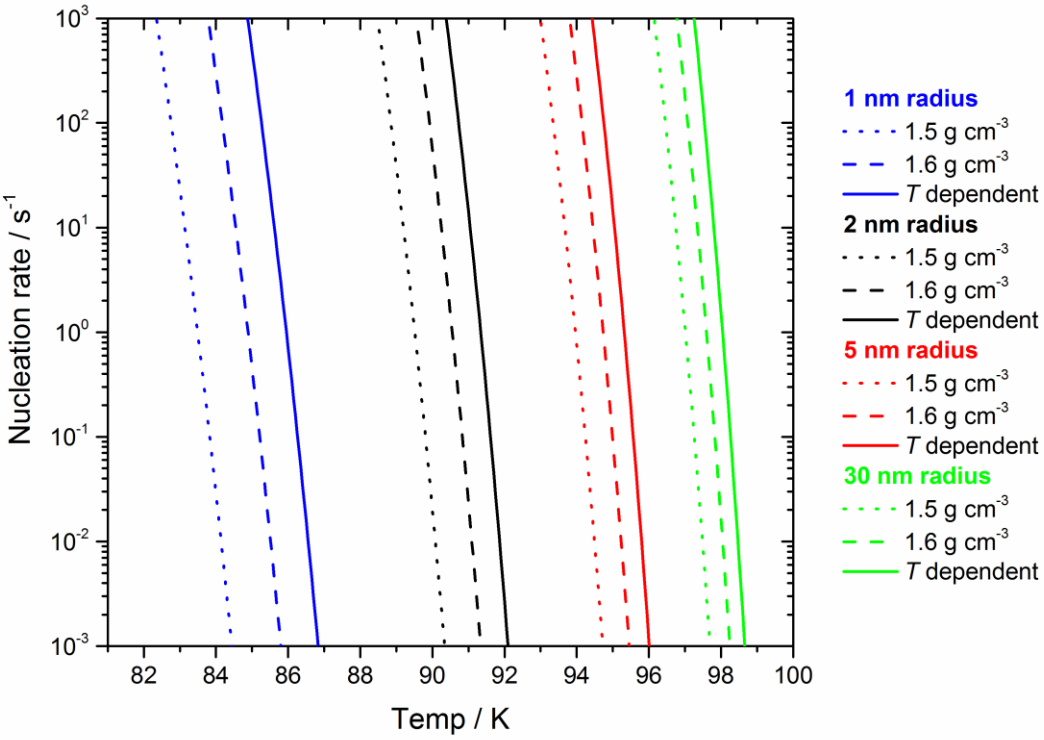

Figure 6.5: Heterogeneous ice nucleation rates at variable CO_2 ice density (where "*T* dependent" indicates the temperature dependent-density fit produced in this study) for INP of selected radii between 1 and 30 nm. CO_2 concentrations were fixed at 10^{14} cm^{-3}, representative of an altitude of 70 km in the Martian atmosphere [*Forget et al.*, 2009]. This figure is calculated using the same variables as Figure 5.3 including the reported m and ΔF_{des}.

6.4 CO_2 ice crystal shape in the mesosphere of Mars

The calculated crystal structure of CO_2-I determined in section 6.2 is used to predict possible crystal shapes of Martian CO_2 ice crystals. A range of crystal shapes have been suggested for the Martian atmosphere based on the crystal structure of CO_2-I ice. Theoretical predictions for the shape of CO_2 crystals on Mars include octahedra, cubes and truncated octahedra [*Wood*, 1999]. Experimentally, CO_2 crystals grown on substrates were found to be dominantly octahedral, some examples of which are shown in Figure 6.6 [*Foster et al.*, 1998; *Wergin et al.*, 1997].

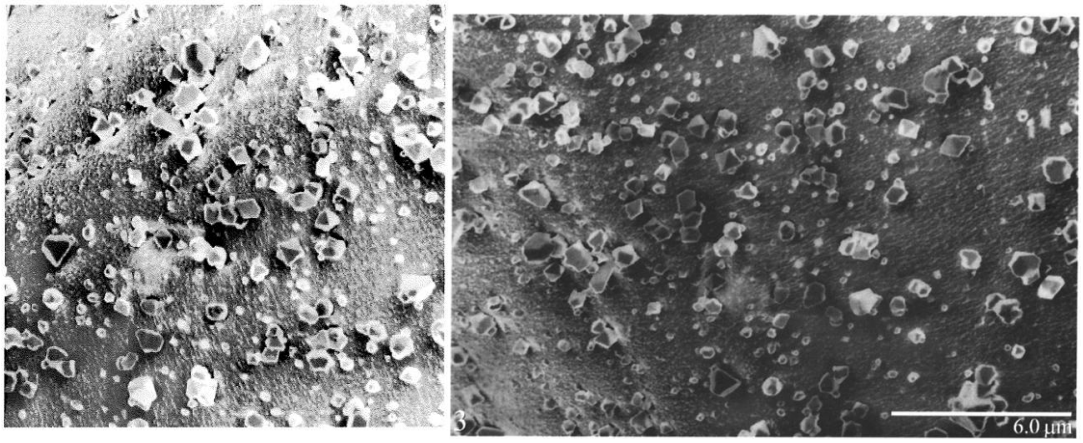

Figure 6.6: SEM images of octahedral CO_2 crystals grown on copper substrates (left) taken from *Wergin et al.* [1997] and regrown CO_2 on a dry ice substrate (right) taken from *Foster et al.* [1998].

The Bravais-Friedel-Donnay-Harker (BFDH) approach is used here to predict the crystal shape of CO_2 ice crystals from the crystallographic symmetry and lattice parameters. The BFDH approach assumes that the linear growth rate of a crystal face is inversely proportional to the corresponding interplanar distance [*Donnay and Harker*, 1937]. Consequently, faces with the smallest Miller indices, which have the largest interplanar distances, will grow the slowest. Faces with higher Miller indices

will expose more dangling bonds and be less stable, grow faster and therefore grow out quickly leaving crystals only expressing the lower energy, lower Miller index faces. The BFDH approach predicts that the {200} and the {111} families of faces will be expressed in crystals of CO_2 ice and this results in a truncated octahedron shape (see Figure 6.7). In real crystals, significant deviations from the BFDH model can occur. This is due to the exact details of the chemical interactions between molecules which can be highly anisotropic and consequently lead to deviations of the growth rates from the simple relationship used in the BFDH approach. In case of CO_2-I this means that crystal shapes can deviate from the idealised cubo-octahedral shape in Figure 6.7.

Ice crystals in the Earth's atmosphere can take on a wide range of forms, from compact hexagonal plates and columns to the huge array of dendritic snowflakes; the crystal shape depending on temperature and supersaturation. Crystal shape is important because it influences crystal fall speeds, growth rates and their optical properties. *Foster et al.* [1998] demonstrated that extinction, absorption and scattering efficiencies in the IR are sensitive to crystal shape, which has implications for paleoclimate modelling of a warmer early Mars [*Forget and Pierrehumbert*, 1997]. It is thought that CO_2 ice crystals in the Martian atmosphere are unlikely to form dendrites since dendritic structures form when crystal growth becomes diffusion limited. For CO_2 ice crystals in the Martian atmosphere which is dominantly composed of CO_2, diffusion limitation is unlikely [*Wood*, 1999]. Martian CO_2 ice crystals are therefore likely to be compact crystals, that would be more reasonably modelled with a spherical assumption [*Listowski et al.*, 2014]. The BFDH model demonstrates that these crystals may have

two families of faces exposed, the six-sided {111} family of faces and the four-sided {200} family.

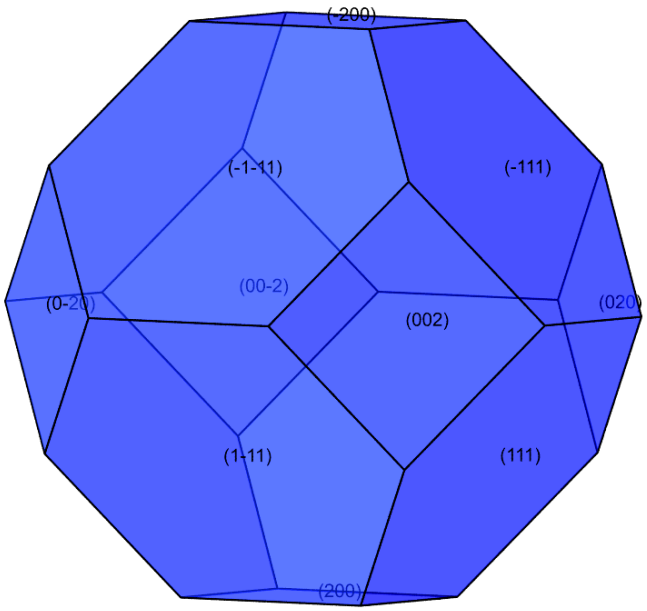

Figure 6.7: Truncated octahedral crystal structure predicted for CO_2-I from BDFH analysis; the different crystallographic planes of the crystal are indicated in the brackets. This indicates that some combination of the two families of faces, {111} and {200}, will be expressed on crystals of CO_2 ice. The potential range of crystal shapes which might be expressed is shown in Figure 6.8. This structure prediction was done using the software package Mercury 3.9 [Cambridge Crystallographic Data Centre].

CO_2 ice may still exhibit a range of crystal shapes if the relative growth rates of the two groups of faces vary. The possible crystal shapes, all with the same O_h point group (derived from the space group of CO_2-I), are shown in Figure 6.8. If the {111} family of faces grows faster than the {200} family then a crystal in the shape of a cube would be expected, whereas if the opposite is the case then an octahedron crystal would form. It is also possible that the

growth rates of the two sets of equivalent faces are competitive, in which case, similarly to that shown in the BFDH morphology in Figure 6.7, a cubo-octahedron would form. Close inspection of the images of CO_2 ice crystals in *Foster et al.* [1998] reveal that while some crystals are clearly octahedral, others are truncated with square faces which are consistent with cubo-octahedra. In the Martian atmosphere CO_2 crystals could have a range of morphologies, from cubic to octahedral. The exact crystal shapes which exist may depend on temperature and supersaturation of the atmosphere from which they grow as well as any effect of latent heat release on the temperature of the growing crystal.

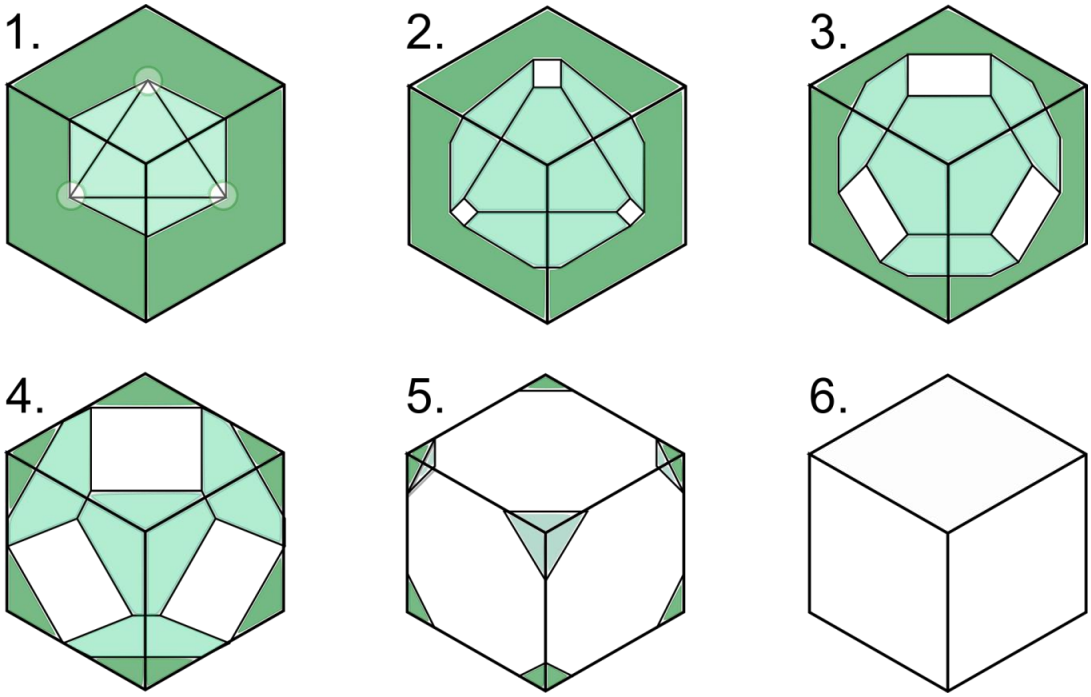

Figure 6.8: Illustration of how an octahedral (bi-pyramidal) crystal shape is related to a cube in which all shapes shown have the same point group (O_h) related to the space group of CO_2-I). A cube results if the growth rate of the {111} family of faces grows more rapidly than the {200} family of faces, whereas an octahedron results if the opposite is true. If the growth rates of the two groups of faces are comparable as is the case in the BFDH analysis, a cubo-octahedral crystal forms.

6.5 Summary and conclusions

In this chapter the first XRD diffraction patterns of CO_2 ice, deposited under temperature and pressure conditions analogous to the Martian mesosphere were presented. A cubic crystal structure consistent with previous literature determinations of CO_2-I with *Pa*-3 space group has been found under all conditions studied. Analysis of the diffraction patterns gave a lattice parameter of 5.578 ± 0.002 Å, a unit cell volume of 173.554 ± 0.19 $Å^3$ and density of 1.684 ± 0.002 g cm^{-3} at 80 K. From the diffraction data, the density was determined from 80 to 130 K and combined with literature data to give a polynomial fit valid from 80 to 195 K (CO_2 density (g cm^{-3}) = 1.72391-2.53x10^{-4} T – 2.87x10^{-6} T^2). This was applied to sedimentation and ice nucleation rates relevant to CO_2 ice clouds in the mesosphere of Mars. Finally, the crystal morphology of solid CO_2 was predicted, suggesting that Martian CO_2 ice crystals could take the shape of a cube, an octahedron or a cubo-octahedron.

7 Conclusions and future work

An understanding of the microphysical processes occurring in PMCs on Earth and mesospheric clouds on Mars is crucial to accurately model and understand larger scale atmospheric processes. Chapter 1 provides the motivation and state of research for these cloud types and identifies specific research questions (section 1.4). These questions were investigated experimentally using the apparatus described in chapter 2, the results of which are detailed in chapters 3 – 6. The overall conclusions of the results chapters are included here along with suggestions of future work. Research relating to the Earth's mesosphere is detailed in section 7.1 and research in the Martian mesosphere is detailed in section 7.2.

7.1 Earth's mesosphere

7.1.1 CO_2 trapping in ASW: applications to PMCs

Chapter 3 addresses the question of whether the high ratio of CO_2:H_2O (>37:1) in the mesosphere could lead to CO_2 trapping in ASW within PMCs [*Emmert et al.*, 2012; *Rong et al.*, 2010]. This trapping process had been experimentally investigated previously but not under deposition conditions analogous to the mesosphere (e.g. *Galvez et al.* [2008]). CO_2 trapping was investigated here using a UHV chamber to produce ASW films at 98 K from gas mixtures of CO_2 and H_2O. These were then analysed using TPD. CO_2 was found to trap effectively within the ASW layer under certain conditions but was limited by the need for sufficient H_2O flux to the sample surface

(> 4.8 x 10^{13} molecules cm^{-2} s^{-1}). CO_2 trapping was evaluated at the molecular level in terms of a need to adsorb sufficient H_2O molecules onto a CO_2 molecule to trap it before the CO_2 desorbed from the ice surface. The experimental limits of CO_2 trapping in ASW were compared to mesospheric fluxes of H_2O and CO_2 for different temperatures. This comparison suggested that the process would only be plausible at temperatures below 100 K, which are rarely reached in the mesosphere.

7.1.2 Metal deposition on PMC particles

Chapter 4 addresses another question regarding the interaction of gas-phase species with PMC particles and how this might affect connected mesospheric processes. Specifically, the deposition of metals onto PMCs was investigated using the same UHV chamber as the results of chapter 3. Depletion of Fe, Na and K layers in the presence of PMCs has been observed [*Gardner et al.*, 2005; *Plane et al.*, 2004; *Raizada et al.*, 2007] while it has been suggested that Mg could also be depleted by PMCs [*Langowski et al.*, 2015]. Experiments on ice films within the UHV chamber were used to investigate the deposition and reactivity of Mg and K on ice at temperatures of 110 – 140 K for the first time. Both metals were readily adsorbed under these conditions and Energetic sputtering by 500 eV Ar^+ and Kr^+ showed that Mg was unreactive on the ice surface, while K formed KOH. These observations were supported by electronic structure calculations, with a Mg atom being shown to be unreactive due to binding on a lone H_2O molecule at a surface irregularity (or surface defect on the ice), while an adsorbed K atom requires relatively little energy to insert into a surface H_2O to produce KOH and a dangling H atom.

TPD experiments showed that Mg and K did not co-desorb with the ice layer upon sublimation. Sputtering experiments after the TPD showed that the metals were instead left as residuals after the ice sublimes. This provided an interesting conclusion that will impact the coagulation of MSPs in the mesosphere during PMC cloud season. Coagulation of MSPs is currently evaluated only in terms of self-polymerization and on already formed MSPs. Due to the significant surface area available for uptake during a PMC event it is hypothesised here that the clouds could act as a second competitive coagulation mechanism for MSPs. Calculations suggest that the depletion of metal during a PMC event would lead to the formation of a population of large (≥ 1 nm radius) MSPs in the region of the cloud. Additionally, due to the differing reactions of the metals with the ice surface compared to metal gas phase reactions, the MSPs produced may be of different composition.

7.1.3 Future work for the Earth's mesosphere

The mesosphere of Earth is subject to trends of decreasing temperature and increasing CO_2 and H_2O concentrations. These trends all move towards making the process of CO_2 trapping more plausible in the future, as the extreme atmospheric conditions required are reached more frequently. Although this study of the CO_2 trapping process is finite and doesn't require significant further investigation, the increasing plausibility of this process should be revisited in the future if current mesospheric trends persist.

The ability to accurately model the effect of metal uptake and subsequent MSP formation in PMCs, accounting for transport of the metals as well as competing coagulation mechanisms, was beyond the scope of the study in chapter 4 but is recommended for future investigation. This would be

achieved by a coupled model that accounts for both the cloud microphysics (and therefore the available surface area for metal uptake with altitude) and the competing MSP formation on existing MSPs. In general, the overall surface area available for MSP formation will be increased in the presence of PMCs and so this model (like the calculations in chapter 4) should lead to predictions of larger populations of increased radius MSPs. This will then have an impact on the gas phase chemistry of the mesosphere and sedimentation of MSPs into the stratosphere and beyond.

7.2 The Martian mesosphere

7.2.1 CO_2 nucleation on nanoparticles in the mesosphere

Chapter 5 address a need for improved understanding of the kinetics of CO_2 cloud formation by investigating heterogeneous nucleation of CO_2 on representative particles for the first time. Mesospheric CO_2 clouds are poorly understood with large uncertainties in the cloud microphysics. This knowledge is necessary in order to better model their occurrence in the Martian mesosphere and improve understanding of the atmosphere as a whole. This aim was achieved using the novel TRAPS instrument based at KIT using MSP analogues nanoparticles of SiO_2 and Fe_xO_y. CO_2 was deposited on these nanoparticles under conditions similar to the mesosphere of Mars produced in the MICE. A desorption energy of CO_2 on the nanoparticles was determined as ΔF_{des} = (18.5 ± 0.2 kJ mol^{-1}), while m was determined using CNT as 0.78 ± 0.02. Applying these CNT parameters to CO_2 clouds in the Martian mesosphere gave nucleation activation temperatures 8 – 18 K (dependent on particle size) below the CO_2 saturation

temperature. This suggests that lower temperatures are required to initiate cloud formation than has been previously predicted.

7.2.2 CO_2 ice structure under Martian atmospheric conditions

Chapter 6 addresses another question that relates to an improved understanding of the microphysical processes of CO_2 clouds on Mars. Specifically, the crystal structure of CO_2 ice and its temperature dependent properties were experimentally investigated for the first time here under temperature and pressure conditions analogous to the Martian mesosphere. XRD patterns of CO_2 ice were presented and a cubic crystal structure of CO_2-I with *Pa*-3 space group was determined. From the diffraction data, the CO_2 ice density was determined from 80 - 130 K and combined with literature data to give a polynomial fit valid from 80 to 195 K (CO_2 density (g cm^{-3}) = $1.72391-2.53\times10^{-4}\ T - 2.87\times10^{-6}\ T^2$). This was applied to sedimentation and ice nucleation rates relevant to CO_2 ice clouds in the mesosphere of Mars. The CO_2 crystal morphology was also predicted, suggesting that Martian CO_2 ice crystals could take the shape of a cube, an octahedron or a cubo-octahedron.

7.2.3 Future work for the Martian mesosphere

In terms of future experimental work regarding the microphysics of CO_2 clouds, it would be advantageous to study CO_2 nucleation on a wider range of nanoparticles to evaluate the effect of changing particle composition on ΔF_{des} and m. It is expected in the future that the NPS on the TRAPS instrument could be used to produce olivine nanoparticles that could be representative of MSPs on Mars. Investigating the nucleating efficiency of a range of particles, would also enable a better understanding of the possible

efficient sources of INP available on Mars. This is a similar idea as to how nucleation of H_2O ice has been investigated in the troposphere of Earth. The overall aim is to achieve a fundamental understanding of the nucleation process and determine the key INP sources.

MDPs are considered in chapter 5 as another possible INP source for CO_2 clouds. JSC MARS-1 and the more recently developed Mojave Mars Simulant (MMS) are two terrestrial simulants of Martian surface dust that could be used as MDP analogues for CO_2 nucleation studies relevant to clouds forming at altitudes below 65 km [*Peters et al.*, 2008; *Pommerol et al.*, 2013]. The TRAPS instrument is not capable of simulating the higher temperature conditions necessary for these clouds. However, a small expansion chamber experiment is currently in development at KIT that was designed to study H_2O ice nucleation [pers. comms., Michael Adams, 2016]. This chamber could be adapted using a liquid N_2 cooling jacket to achieve temperature and pressure conditions analogous to the lower Martian atmosphere.

The nucleation parameters presented in chapter 5 are presently the best available for modelling mesospheric CO_2 clouds. Inclusion of these CO_2 nucleation parameters along with the temperature dependent density determined in chapter 6 is recommended for future modelling of the Martian mesosphere. Currently the first ever 3D model of the Martian atmosphere that incorporates mesospheric CO_2 clouds is in development and will include the parameters presented here [pers. comms., Anni Maattanen, 2016]. The temperature dependent density reported in chapter 6 is not only applicable to the mesosphere but is also useful for modelling of ice processes

throughout the Martian atmosphere including the seasonal CO_2 polar caps. This parameterization will be incorporated into models that predict CO_2 snowfall from tropospheric CO_2 clouds at the Martian poles [pers. comms., Paul Hayne, 2017].

List of References

Arnold, F. (1980), Ion-induced nucleation of atmospheric water vapor at the mesopause, *Planetary and Space Science*, *28*(10), 1003-1009.

Aronson, J. R., and A. G. Emslie (1975), Composition of Martian Dust as Derived by Infrared Spectroscopy from Mariner-9, *Journal of Geophysical Research*, *80*(35), 4925-4931.

Asmus, H., H. Wilms, B. Strelnikov, and M. Rapp (2014), On the heterogeneous nucleation of mesospheric ice on meteoric smoke particles: Microphysical modeling, *Journal of Atmospheric and Solar-Terrestrial Physics*, *118, Part B*, 180-189.

Atkins, P. W., and J. De Paula (2009), *Elements of physical chemistry*, Oxford University Press, Oxford; New York.

Attard, G. B. C. (1998), *Surfaces*, Oxford University Press, Oxford; New York.

Backus, E. H. G., M. L. Grecea, A. W. Kleyn, and M. Bonn (2004), Surface crystallization of amorphous solid water, *Physical Review Letters*, *92*(23).

Bailey, S. M., G. E. Thomas, M. E. Hervig, J. D. Lumpe, C. E. Randall, J. N. Carstens, B. Thurairajah, D. W. Rusch, J. M. Russell, III, and L. L. Gordley (2015), Comparing nadir and limb observations of polar mesospheric clouds: The effect of the assumed particle size distribution, *Journal of Atmospheric and Solar-Terrestrial Physics*, *127*, 51-65.

Bar-Nun, A., G. Notesco, and T. Owen (2007), Trapping of N_2, CO and Ar in amorphous ice—Application to comets, *Icarus*, *190*(2), 655-659.

Bar-nun, A., G. Herman, D. Laufer, and M. L. Rappaport (1985), Trapping and release of gases by water ice and implications for icy bodies, *Icarus*, *63*(3), 317-332.

Bell, J. F., W. M. Calvin, M. E. OckertBell, D. Crisp, J. B. Pollack, and J. Spencer (1996), Detection and monitoring of H_2O and CO_2 ice clouds on Mars, *Journal of Geophysical Research-Planets*, *101*(E4), 9227-9237.

Benna, M., P. R. Mahaffy, J. M. Grebowsky, J. M. C. Plane, R. V. Yelle, and B. M. Jakosky (2015), Metallic ions in the upper atmosphere of Mars from the passage of comet C/2013 A1 (Siding Spring), *Geophysical Research Letters*, *42*(12), 4670-4675.

Berger, U., and F. J. Lübken (2015), Trends in mesospheric ice layers in the Northern Hemisphere during 1961–2013, *Journal of Geophysical Research: Atmospheres*, *120*(21), 11277-11298.

Bish, D. L., et al. (2013), X-ray Diffraction Results from Mars Science Laboratory: Mineralogy of Rocknest at Gale Crater, *Science*, *341*(6153).

Bragg, W. L. (1947), The conversion factor for kX units to ångström units, *Journal of Scientific Instruments*, *24*(1), 27.

Brasseur, G. P., and S. Solomon (2006), *Aeronomy of the middle atmosphere: Chemistry and physics of the stratosphere and mesosphere*, Springer Science & Business Media.

Brown, D. E., S. M. George, C. Huang, E. K. L. Wong, K. B. Rider, R. S. Smith, and B. D. Kay (1996), H_2O condensation coefficient and refractive index for vapor-deposited ice from molecular beam and optical interference measurements, *Journal of Physical Chemistry*, *100*(12), 4988-4995.

Carrillo-Sánchez, J. D., D. Nesvorný, P. Pokorný, D. Janches, and J. M. C. Plane (2016), Sources of cosmic dust in the Earth's atmosphere, *Geophysical Research Letters*, *43*(23), 11979-11986.

Chandran, A., D. W. Rusch, G. E. Thomas, S. E. Palo, G. Baumgarten, E. J. Jensen, and A. W. Merkel (2012), Atmospheric gravity wave effects on polar mesospheric clouds: A comparison of numerical simulations from CARMA 2D with AIM observations, *Journal of Geophysical Research-Atmospheres*, *117*.

Clancy, R. T., and B. J. Sandor (1998), CO_2 ice clouds in the upper atmosphere of Mars, *Geophysical Research Letters*, *25*(4), 489-492.

Clancy, R. T., M. J. Wolff, B. A. Whitney, B. A. Cantor, and M. D. Smith (2007), Mars equatorial mesospheric clouds: Global occurrence and physical properties from Mars Global Surveyor Thermal Emission Spectrometer and Mars Orbiter Camera limb observations, *Journal of Geophysical Research-Planets*, *112*(E4).

Clancy, R. T., M. J. Wolff, B. A. Whitney, B. A. Cantor, M. D. Smith, and T. H. McConnochie (2010), Extension of atmospheric dust loading to high altitudes during the 2001 Mars dust storm: MGS TES limb observations, *Icarus*, *207*(1), 98-109.

Clark, B. C., A. K. Baird, R. J. Weldon, D. M. Tsusaki, L. Schnabel, and M. P. Candelaria (1982), Chemical-Composition of Martian Fines, *Journal of Geophysical Research*, *87*(Nb12), 59-67.

Colaprete, A., and O. B. Toon (2003), Carbon dioxide clouds in an early dense Martian atmosphere, *Journal of Geophysical Research-Planets*, *108*(E4).

Colaprete, A., J. R. Barnes, R. M. Haberle, and F. Montmessin (2008), CO_2 clouds, CAPE and convection on Mars: Observations and general circulation modeling, *Planetary and Space Science*, *56*(2), 150-180.

Curzon, A. E. (1972), A comment on the lattice parameter of solid carbon dioxide at -190°C, *Physica*, *59*(4), 733.

Dawkins, E. C. M., J. M. C. Plane, M. P. Chipperfield, and W. Feng (2015), The near-global mesospheric potassium layer: Observations and modeling, *Journal of Geophysical Research: Atmospheres*, *120*(15), 7975-7987.

de Smedt, J., and W. H. Keesom (1924), The structure of solid nitrous oxide and carbon dioxide., *Proceedings of the Koninklijke Akademie Van Wetenschappen Te Amsterdam*, *27*(1/10), 839-846.

Donnay, J. D. H., and D. Harker (1937), A new law of crystal morphology extending the law of bravais, *Journal of Mineralogical Society of American*, *22*, 446-467.

Duft, D., M. Nachbar, M. Eritt, and T. Leisner (2015), A Linear Trap for Studying the Interaction of Nanoparticles with Supersaturated Vapors, *Aerosol Science and Technology*, *49*(9), 683-691.

Elteto, A., and O. B. Toon (2010), The effects and characteristics of atmospheric dust during martian global dust storm 2001A, *Icarus*, *210*(2), 589-611.

Emmert, J. T., M. H. Stevens, P. F. Bernath, D. P. Drob, and C. D. Boone (2012), Observations of increasing carbon dioxide concentration in Earth's thermosphere, *Nature Geoscience*, *5*(12), 868-871.

Ernst, K. H., D. Schlatterbeck, and K. Christmann (1999), Adsorption of carbon dioxide on Cu(110) and on hydrogen and oxygen covered Cu(110) surfaces, *Physical Chemistry Chemical Physics*, *1*(17), 4105-4112.

Escribano, R. M., G. M. Munoz Caro, G. A. Cruz-Diaz, Y. Rodriguez-Lazcano, and B. Mate (2013), Crystallization of CO_2 ice and the absence of amorphous CO_2 ice in space, *Proceedings of the National Academy of Sciences of the United States of America*, *110*(32), 12899-12904.

Famá, M., J. Shi, and R. A. Baragiola (2008), Sputtering of ice by low-energy ions, *Surface Science*, *602*(1), 156-161.

Feng, W., D. R. Marsh, M. P. Chipperfield, D. Janches, J. Höffner, F. Yi, and J. M. C. Plane (2013), A global atmospheric model of meteoric iron, *Journal of Geophysical Research: Atmospheres*, *118*(16), 9456-9474.

Fletcher, N. H. (1958), Size effect in heterogeneous nucleation, *The Journal of Chemical Physics*, *29*(3), 572-576.

Foresman, J. B., and A. Frisch (1996), *Exploring chemistry with electronic structure methods*, Gaussian, Inc., Pittsburgh PA.

Forget, F., and R. T. Pierrehumbert (1997), Warming early Mars with carbon dioxide clouds that scatter infrared radiation, *Science*, *278*(5341), 1273-1276.

Forget, F., F. Hourdin, and O. Talagrand (1998), CO_2 snowfall on Mars: Simulation with a general circulation model, *Icarus*, *131*(2), 302-316.

Forget, F., R. Wordsworth, E. Millour, J. B. Madeleine, L. Kerber, J. Leconte, E. Marcq, and R. M. Haberle (2013), 3D modelling of the early martian climate under a denser CO_2 atmosphere: Temperatures and CO_2 ice clouds, *Icarus*, *222*(1), 81-99.

Forget, F., F. Hourdin, R. Fournier, C. Hourdin, O. Talagrand, M. Collins, S. R. Lewis, P. L. Read, and J.-P. Huot (1999), Improved general circulation models of the Martian atmosphere from the surface to above 80 km, *Journal of Geophysical Research: Planets*, *104*(E10), 24155-24175.

Forget, F., F. Montmessin, J. L. Bertaux, F. Gonzalez-Galindo, S. Lebonnois, E. Quemerais, A. Reberac, E. Dimarellis, and M. A. Lopez-Valverde (2009), Density and temperatures of the upper Martian atmosphere measured by stellar occultations with Mars Express SPICAM, *Journal of Geophysical Research-Planets*, *114*.

Foster, J. L., A. T. C. Chang, D. K. Hall, W. P. Wergin, E. F. Erbe, and J. Barton (1998), Carbon dioxide crystals: An examination of their size, shape, and scattering properties at 37 GHz and comparisons with water ice (snow) measurements, *Journal of Geophysical Research-Planets*, *103*(E11), 25839-25850.

Frankland, V. L. (2011), Ph.D. Thesis, *Heriot-Watt University*.

Frankland, V. L., and J. M. C. Plane (2015), Fe embedded in ice: the impacts of sublimation and energetic particle bombardment, *Journal of Atmospheric and Solar-Terrestrial Physics*, *127*, 103-110.

Frankland, V. L., A. D. James, W. Feng, and J. M. C. Plane (2015), The uptake of HNO_3 on meteoric smoke analogues, *Journal of Atmospheric and Solar-Terrestrial Physics*, *127*, 150-160.

Fraser, H. J., M. P. Collings, M. R. S. McCoustra, and D. A. Williams (2001), Thermal desorption of water ice in the interstellar medium, *Monthly Notices of the Royal Astronomical Society*, *327*(4), 1165-1172.

Frisch, M. J., et al. (2009), Gaussian 09, edited, Gaussian, Inc., Wallingford, CT, USA.

Gadsden, M. (1982), Noctilucent clouds, *Space Science Reviews*, *33*(3), 279-334.

Gadsden, M., and W. Schroder (1989), *Noctilucent Clouds*, Springer-Verlag, Berlin.

Galli, A., A. Vorburger, A. Pommerol, P. Wurz, B. Jost, O. Poch, Y. Brouet, M. Tulej, and N. Thomas (2016), Surface charging of thick porous water ice layers relevant for ion sputtering experiments, *Planetary and Space Science*, *126*, 63-71.

Galvez, O., B. Mate, V. J. Herrero, and R. Escribano (2008), Trapping and adsorption of CO_2 in amorphous ice: A FTIR study, *Icarus*, *197*(2), 599-605.

Galvez, O., I. K. Ortega, B. Mate, M. A. Moreno, B. Martin-Llorente, V. J. Herrero, R. Escribano, and P. J. Gutierrez (2007), A study of the interaction of CO_2 with water ice, *Astronomy & Astrophysics*, *472*(2), 691-698.

Garcia, R. R., M. López-Puertas, B. Funke, D. R. Marsh, D. E. Kinnison, A. K. Smith, and F. González-Galindo (2014), On the distribution of CO_2 and CO in the mesosphere and lower thermosphere, *Journal of Geophysical Research: Atmospheres*, *119*(9), 5700-5718.

Gardner, C. S., J. M. C. Plane, W. Pan, T. Vondrak, B. J. Murray, and X. Chu (2005), Seasonal variations of the Na and Fe layers at the South Pole and their implications for the chemistry and general circulation of the polar mesosphere, *Journal of Geophysical Research: Atmospheres*, *110*(D10).

Giesen, B., H. Wiggers, A. Kowalik, and P. Roth (2005), Formation of Si-nanoparticles in a microwave reactor: Comparison between experiments and modelling, *Journal of Nanoparticle Research*, *7*(1), 29-41.

Glandorf, D. L., A. Colaprete, M. A. Tolbert, and O. B. Toon (2002), CO_2 snow on Mars and early Earth: Experimental constraints, *Icarus*, *160*(1), 66-72.

Gonzalez-Galindo, F., A. Maattanen, F. Forget, and A. Spiga (2011), The martian mesosphere as revealed by CO_2 cloud observations and General Circulation Modeling, *Icarus*, *216*(1), 10-22.

Greenler, R. G. (1966), Infrared study of adsorbed molecules on metal surfaces by reflection techniques, *The Journal of Chemical Physics*, *44*(1), 310.

Gumbel, J., D. E. Siskind, G. Witt, K. M. Torkar, and M. Friedrich (2003), Influences of ice particles on the ion chemistry of the polar summer mesosphere, *Journal of Geophysical Research: Atmospheres*, *108*(D8).

Guzewich, S. D., E. R. Talaat, A. D. Toigo, D. W. Waugh, and T. H. McConnochie (2013), High-altitude dust layers on Mars: Observations with the Thermal Emission Spectrometer, *Journal of Geophysical Research: Planets*, *118*(6), 1177-1194.

Havnes, O., J. Gumbel, T. Antonsen, J. Hedin, and C. La Hoz (2014), On the size distribution of collision fragments of NLC dust particles and their relevance to meteoric smoke particles, *Journal of Atmospheric and Solar-Terrestrial Physics*, *118, Part B*, 190-198.

Hayne, P. O., D. A. Paige, and N. G. Heavens (2014), The role of snowfall in forming the seasonal ice caps of Mars: Models and constraints from the Mars Climate Sounder, *Icarus*, *231*, 122-130.

Hayne, P. O., D. A. Paige, J. T. Schofield, D. M. Kass, A. Kleinbohl, N. G. Heavens, and D. J. McCleese (2012), Carbon dioxide snow clouds on Mars: South polar winter observations by the Mars Climate Sounder, *Journal of Geophysical Research-Planets*, *117*.

Heavens, N. G., M. I. Richardson, A. Kleinböhl, D. M. Kass, D. J. McCleese, W. Abdou, J. L. Benson, J. T. Schofield, J. H. Shirley, and P. M. Wolkenberg (2011), Vertical distribution of dust in the Martian atmosphere during northern spring and summer: High-altitude tropical dust maximum at northern summer solstice, *Journal of Geophysical Research: Planets*, *116*(E1).

Herr, K. C., and G. C. Pimentel (1970), Evidence for solid carbon dioxide in upper atmosphere of Mars, *Science*, *167*(3914), 47-49.

Hervig, M. E., and L. L. Gordley (2010), Temperature, shape, and phase of mesospheric ice from Solar Occultation for Ice Experiment observations, *Journal of Geophysical Research-Atmospheres*, *115*, D15208.

Hervig, M. E., U. Berger, and D. E. Siskind (2016a), Decadal variability in PMCs and implications for changing temperature and water vapor in the upper mesosphere, *Journal of Geophysical Research: Atmospheres*, *121*(5), 2383-2392.

Hervig, M. E., M. Rapp, R. Latteck, and L. L. Gordley (2011), Observations of mesospheric ice particles from the ALWIN radar and SOFIE, *Journal of Atmospheric and Solar-Terrestrial Physics*, *73*(14–15), 2176-2183.

Hervig, M. E., D. E. Siskind, S. M. Bailey, and J. M. Russell, III (2015), The influence of PMCs on water vapor and drivers behind PMC variability from SOFIE observations, *Journal of Atmospheric and Solar-Terrestrial Physics*, *132*, 124-134.

Hervig, M. E., R. E. Thompson, M. McHugh, L. L. Gordley, J. M. Russell, and M. E. Summers (2001), First confirmation that water ice is the primary component of polar mesospheric clouds, *Geophysical Research Letters*, *28*(6), 971-974.

Hervig, M. E., M. H. Stevens, L. L. Gordley, L. E. Deaver, J. M. Russell, and S. M. Bailey (2009), Relationships between polar mesospheric clouds, temperature, and water vapor from Solar Occultation for Ice Experiment (SOFIE) observations, *Journal of Geophysical Research: Atmospheres*, *114*(D20).

Hervig, M. E., L. E. Deaver, C. G. Bardeen, J. M. Russell, III, S. M. Bailey, and L. L. Gordley (2012), The content and composition of meteoric smoke in mesospheric ice particles from SOFIE observations, *Journal of Atmospheric and Solar-Terrestrial Physics*, *84-85*, 1-6.

Hervig, M. E., M. Gerding, M. H. Stevens, R. Stockwell, S. M. Bailey, J. M. Russell, III, and G. Stober (2016b), Mid-latitude mesospheric clouds and their environment from SOFIE observations, *Journal of Atmospheric and Solar-Terrestrial Physics*, *149*, 1-14.

Hinson, D. P., and R. J. Wilson (2002), Transient eddies in the southern hemisphere of Mars, *Geophysical Research Letters*, *29*(7).

Hobbs, P. V. (1974), *Ice physics*, Clarendon Press, Oxford.

Hodyss, R., J. D. Goguen, P. V. Johnson, C. Campbell, and I. Kanik (2008a), Release of N_2, CH_4, CO_2, and H_2O from surface ices on Enceladus, *Icarus*, *197*(1), 152-156.

Hodyss, R., P. V. Johnson, G. E. Orzechowska, J. D. Goguen, and I. Kanik (2008b), Carbon dioxide segregation in 1:4 and 1:9 CO_2:H_2O ices, *Icarus*, *194*(2), 836-842.

Hourdin, F., P. Levan, F. Forget, and O. Talagrand (1993), Meteorological variability and the annual surface pressure cycle on Mars, *Journal of the Atmospheric Sciences*, *50*(21), 3625-3640.

Hu, R. Y., K. Cahoy, and M. T. Zuber (2012), Mars atmospheric CO_2 condensation above the north and south poles as revealed by radio occultation, climate sounder, and laser ranging observations, *Journal of Geophysical Research-Planets*, *117*, 21.

Iraci, L. T., B. D. Phebus, B. M. Stone, and A. Colaprete (2010), Water ice cloud formation on Mars is more difficult than presumed: Laboratory studies of ice nucleation on surrogate materials, *Icarus*, *210*(2), 985-991.

Isenor, M., R. Escribano, T. C. Preston, and R. Signorell (2013), Predicting the infrared band profiles for CO_2 cloud particles on Mars, *Icarus*, *223*(1), 591-601.

Jenniskens, P., and D. F. Blake (1994), Structural transitions in amorphous water ice and astrophysical implications, *Science*, *265*(5173), 753-756.

Jenniskens, P., and D. F. Blake (1996), Crystallization of amorphous water ice in the solar system, *Astrophysical Journal*, *473*(2), 1104-1113.

Keesom, W. H., and J. W. L. Kohler (1934a), New determination of the lattice constant of carbon dioxide, *Physica*, *1*, 167-174.

Keesom, W. H., and J. W. L. Kohler (1934b), The lattice constant and expansion coefficient of solid carbon dioxide, *Physica*, *1*, 655-658.

Kiliani, J., G. Baumgarten, F. J. Lübken, U. Berger, and P. Hoffmann (2013), Temporal and spatial characteristics of the formation of strong noctilucent clouds, *Journal of Atmospheric and Solar-Terrestrial Physics*, *104*, 151-166.

Kleinbohl, A., et al. (2009), Mars Climate Sounder limb profile retrieval of atmospheric temperature, pressure, and dust and water ice opacity, *Journal of Geophysical Research-Planets*, *114*.

Kohl, I., L. Bachmann, A. Hallbrucker, E. Mayer, and T. Loerting (2005), Liquid-like relaxation in hyperquenched water at <= 140 K, *Physical Chemistry Chemical Physics*, *7*(17), 3210-3220.

Kumi, G., S. Malyk, S. Hawkins, H. Reisler, and C. Wittig (2006), Amorphous solid water films: Transport and guest-host interactions with CO_2 and N_2O dopants, *Journal of Physical Chemistry A*, *110*(6), 2097-2105.

Langowski, M. P., C. von Savigny, J. P. Burrows, W. Feng, J. M. C. Plane, D. R. Marsh, D. Janches, M. Sinnhuber, A. C. Aikin, and P. Liebing (2015), Global investigation of the Mg atom and ion layers using SCIAMACHY/Envisat observations between 70 and 150 km altitude and WACCM-Mg model results, *Atmospheric Chemistry and Physics*, *15*(1), 273-295.

Langsdorf, A. (1939), A continuously sensitive diffusion cloud chamber, *Review of Scientific Instruments*, *10*(3), 91-103.

Laštovička, J., R. A. Akmaev, G. Beig, J. Bremer, J. T. Emmert, C. Jacobi, M. J. Jarvis, G. Nedoluha, Y. I. Portnyagin, and T. Ulich (2008), Emerging pattern of global change in the upper atmosphere and ionosphere, *Annales Geophysicae*, *26*(5), 1255-1268.

Laufer, D., E. Kochavi, and A. Bar-Nun (1987), Structure and dynamics of amorphous water ice, *Physical Review B*, *36*(17), 9219-9227.

Le Bail, A., H. Duroy, and J. L. Fourquet (1988), Ab-initio structure determination of $LiSbWO_6$ by X-ray powder diffraction, *Materials Research Bulletin*, *23*(3), 447-452.

Leovy, C. (2001), Weather and climate on Mars, *Nature*, *412*(6843), 245-249.

Listowski, C., A. Maattanen, I. Riipinen, F. Montmessin, and F. Lefevre (2013), Near-pure vapor condensation in the Martian atmosphere: CO_2 ice crystal growth, *Journal of Geophysical Research-Planets*, *118*(10), 2153-2171.

Listowski, C., A. Maattanen, F. Montmessin, A. Spiga, and F. Lefevre (2014), Modeling the microphysics of CO_2 ice clouds within wave-induced cold pockets in the martian mesosphere, *Icarus*, *237*, 239-261.

Lübken, F. J., and J. Höffner (2004), Experimental evidence for ice particle interaction with metal atoms at the high latitude summer mesopause region, *Geophysical Research Letters*, *31*(8).

Lübken, F. J., J. Lautenbach, J. Hoffner, M. Rapp, and M. Zecha (2009), First continuous temperature measurements within polar mesosphere summer echoes, *Journal of Atmospheric and Solar-Terrestrial Physics*, *71*(3-4), 453-463.

Luna, R., C. Millan, C. Santonja, and M. A. Satorre (2009), Triple test under high vacuum conditions to control the reliability of thin ice film accretion and desorption for astrophysical applications, *Vacuum*, *83*(6), 942-948.

Maass, O., and W. H. Barnes (1926), Some thermal constants of solid and liquid carbon dioxide, *Proceedings of the Royal Society of London Series a-Containing Papers of a Mathematical and Physical Character*, *111*(757), 224-244.

Maattanen, A., H. Vehkamaki, A. Lauri, I. Napari, and M. Kulmala (2007), Two-component heterogeneous nucleation kinetics and an application to Mars, *Journal of Chemical Physics*, *127*(13).

Maattanen, A., H. Vehkamaki, A. Lauri, S. Merikallio, J. Kauhanen, H. Savijarvi, and M. Kulmala (2005), Nucleation studies in the Martian atmosphere, *Journal of Geophysical Research-Planets*, *110*(E2).

Maattanen, A., et al. (2010), Mapping the mesospheric CO_2 clouds on Mars: MEx/OMEGA and MEx/HRSC observations and challenges for atmospheric models, *Icarus*, *209*(2), 452-469.

Magalhães, J. A., J. T. Schofield, and A. Seiff (1999), Results of the Mars Pathfinder atmospheric structure investigation, *Journal of Geophysical Research-Planets*, *104*(E4), 8943-8955.

Mahaffy, P. R., et al. (2013), Abundance and Isotopic Composition of Gases in the Martian Atmosphere from the Curiosity Rover, *Science*, *341*(6143), 263-266.

Malkin, T. L., B. J. Murray, A. V. Brukhno, J. Anwar, and C. G. Salzmann (2012), Structure of ice crystallized from supercooled water, *Proceedings of the National Academy of Sciences of the United States of America*, *109*(10), 4021-4021.

Malkin, T. L., B. J. Murray, C. G. Salzmann, V. Molinero, S. J. Pickering, and T. F. Whale (2015), Stacking disorder in ice I, *Physical Chemistry Chemical Physics*, *17*(1), 60-76.

Maltagliati, L., F. Montmessin, O. Korablev, A. Fedorova, F. Forget, A. Maattanen, F. Lefevre, and J. L. Bertaux (2013), Annual survey of water vapor vertical distribution and water-aerosol coupling in the martian atmosphere observed by SPICAM/MEx solar occultations, *Icarus*, *223*(2), 942-962.

Malyk, S., G. Kumi, H. Reisler, and C. Wittig (2007), Trapping and release of CO_2 guest molecules by amorphous ice, *Journal of Physical Chemistry A*, *111*(51), 13365-13370.

Mate, B., O. Galvez, B. Martin-Llorente, M. A. Moreno, V. J. Herrero, R. Escribano, and E. Artacho (2008), Ices of CO_2/H_2O mixtures. Reflection-absorption IR spectroscopy and theoretical calculations, *Journal of Physical Chemistry A*, *112*(3), 457-465.

May, R. A., R. S. Smith, and B. D. Kay (2011), Probing the interaction of amorphous solid water on a hydrophobic surface: dewetting and crystallization kinetics of ASW on carbon tetrachloride, *Physical Chemistry Chemical Physics*, *13*(44), 19848-19855.

May, R. A., R. S. Smith, and B. D. Kay (2012), The Molecular Volcano Revisited: Determination of Crack Propagation and Distribution During the Crystallization of Nanoscale Amorphous Solid Water Films, *Journal of Physical Chemistry Letters*, *3*(3), 327-331.

May, R. A., R. S. Smith, and B. D. Kay (2013), The release of trapped gases from amorphous solid water films. I. "Top-down" crystallization-induced crack propagation probed using the molecular volcano, *Journal of Chemical Physics*, *138*(10), 104501.

McConnochie, T. H., J. F. Bell, D. Savransky, M. J. Wolff, A. D. Toigo, H. Wang, M. I. Richardson, and P. R. Christensen (2010), THEMIS-VIS observations of clouds in the martian mesosphere: Altitudes, wind speeds, and decameter-scale morphology, *Icarus*, *210*(2), 545-565.

Meinen, J., S. Khasminskaya, E. Rühl, W. Baumann, and T. Leisner (2010), The TRAPS Apparatus: Enhancing Target Density of Nanoparticle Beams in Vacuum for X-ray and Optical Spectroscopy, *Aerosol Science and Technology*, *44*(4), 316-328.

Millour, E., F. Forget, F. González-Galindo, A. Spiga, S. Lebonnois, L. Montabone, S. Lewis, P. Read, M. López-Valverde, and G. Gilli (2008), The latest (version 4.3) Mars climate database, *Mars Atmosphere: Modeling and Observations*, 1-4.

Mischna, M. A., J. F. Kasting, A. Pavlov, and R. Freedman (2000), Influence of carbon dioxide clouds on early martian climate, *Icarus*, *145*(2), 546-554.

Mitterdorfer, C., M. Bauer, and T. Loerting (2011), Clathrate hydrate formation after CO_2-H_2O vapour deposition, *Physical Chemistry Chemical Physics*, *13*(44), 19765-19772.

Montmessin, F., F. Forget, J. L. Bertaux, A. Spiga, and A. Määttänen (2011), Existence of Supercold Atmospheric Layers in the Martian Mesosphere, in *The Fourth International Workshop on the Mars Atmosphere: Modelling and observation*, edited, Paris, France.

Montmessin, F., B. Gondet, J. P. Bibring, Y. Langevin, P. Drossart, F. Forget, and T. Fouchet (2007), Hyperspectral imaging of convective CO_2 ice clouds in the equatorial mesosphere of Mars, *Journal of Geophysical Research-Planets*, *112*(E11).

Montmessin, F., et al. (2006), Subvisible CO_2 ice clouds detected in the mesosphere of Mars, *Icarus*, *183*(2), 403-410.

Murray, B. J., and J. M. C. Plane (2005), Uptake of Fe, Na and K atoms on low-temperature ice: implications for metal atom scavenging in the vicinity of polar mesospheric clouds, *Physical Chemistry Chemical Physics*, *7*(23), 3970-3979.

Murray, B. J., and E. J. Jensen (2010), Homogeneous nucleation of amorphous solid water particles in the upper mesosphere, *Journal of Atmospheric and Solar-Terrestrial Physics*, *72*(1), 51-61.

Murray, B. J., T. L. Malkin, and C. G. Salzmann (2015), The crystal structure of ice under mesospheric conditions, *Journal of Atmospheric and Solar-Terrestrial Physics*, *127*, 78-82.

Mustard, J. F., et al. (2008), Hydrated silicate minerals on mars observed by the Mars reconnaissance orbiter CRISM instrument, *Nature*, *454*(7202), 305-309.

Nachbar, M., D. Duft, and T. Leisner (2016a), Heterogeneous nucleation and growth of water vapor on meteoric smoke particle analogues at mesospheric conditions, paper presented at EGU general assembly 2016, Vienna, Austria.

Nachbar, M., D. Duft, T. P. Mangan, J. C. G. Martin, J. M. C. Plane, and T. Leisner (2016b), Laboratory measurements of heterogeneous CO_2 ice nucleation on nanoparticles under conditions relevant to the Martian mesosphere, *Journal of Geophysical Research: Planets*, *121*, 753–769.

Noguchi, K., S. Ikeda, T. Kuroda, S. Tellmann, and M. Pätzold (2014), Estimation of changes in the composition of the Martian atmosphere caused by CO_2 condensation from GRS Ar measurements and its application to the rederivation of MGS radio occultation measurements, *Journal of Geophysical Research: Planets*, *119*(12), 2510-2521.

Oakes, D. J. (1994), Ph.D. thesis, *University of East Anglia*.

Pätzold, M., S. Tellman, B. Hausler, D. Hinson, R. Schaa, and G. L. Tyler (2005), A sporadic third layer in the ionosphere of Mars, *Science*, *310*(5749), 837-839.

Pawley, G. S. (1981), Unit-cell refinement from powder diffraction scans, *Journal of Applied Crystallography*, *14*(Dec), 357-361.

Peters, G. H., W. Abbey, G. H. Bearman, G. S. Mungas, J. A. Smith, R. C. Anderson, S. Douglas, and L. W. Beegle (2008), Mojave Mars simulant—Characterization of a new geologic Mars analog, *Icarus*, *197*(2), 470-479.

Petrenko, V. F., and R. W. Whitworth (1999), *Physics of ice*, Oxford University Press, Oxford; New York.

Phebus, B. D., A. V. Johnson, B. Mar, B. M. Stone, A. Colaprete, and L. T. Iraci (2011), Water ice nucleation characteristics of JSC Mars-1 regolith simulant under simulated Martian atmospheric conditions, *Journal of Geophysical Research-Planets*, *116*(E04009).

Plane, J. M. C. (2003), Atmospheric Chemistry of Meteoric Metals, *Chemical Reviews*, *103*(12), 4963-4984.

Plane, J. M. C. (2011), On the role of metal silicate molecules as ice nuclei, *Journal of Atmospheric and Solar-Terrestrial Physics*, *73*(14-15), 2192-2200.

Plane, J. M. C. (2012), Cosmic dust in the earth's atmosphere, *Chemical Society Reviews*, *41*(19), 6507-6518.

Plane, J. M. C., B. J. Murray, X. Z. Chu, and C. S. Gardner (2004), Removal of meteoric iron on polar mesospheric clouds, *Science*, *304*(5669), 426-428.

Plane, J. M. C., et al. (2014), A combined rocket-borne and ground-based study of the sodium layer and charged dust in the upper mesosphere, *Journal of Atmospheric and Solar-Terrestrial Physics*, *118, Part B*, 151-160.

Poling, G. (1970), Infrared reflection studies of metal surfaces, *Journal of Colloid and Interface Science*, *34*(3), 365-374.

Pollack, J. B., Colburn, D., Kahn, R., Hunter, J., Van Camp, W., Carlston, C. E., Wolf, M. R. (1977), Properties of aerosols in the Martian atmosphere, as inferred from Viking Lander imaging data, *Journal of Geophysical Research*, *82*, 4479-4496.

Pommerol, A., N. Thomas, B. Jost, P. Beck, C. Okubo, and A. S. McEwen (2013), Photometric properties of Mars soils analogs, *Journal of Geophysical Research: Planets*, *118*(10), 2045-2072.

Prinn, R. G., and B. Fegley (1987), The Atmospheres of Venus, Earth and Mars - A critical comparison, *Annual Review of Earth and Planetary Sciences*, *15*, 171-212.

Raizada, S., M. Rapp, F. J. Lübken, J. Höffner, M. Zecha, and J. M. C. Plane (2007), Effect of ice particles on the mesospheric potassium layer at Spitsbergen (78°N), *Journal of Geophysical Research: Atmospheres*, *112*(D8).

Ramirez, R. M., and J. F. Kasting (2017), Could cirrus clouds have warmed early Mars?, *Icarus*, *281*, 248-261.

Rapp, M., and F. J. Lübken (2004), Polar mesosphere summer echoes (PMSE): review of observations and current understanding, *Atmospheric Chemistry and Physics*, *4*, 2601-2633.

Rapp, M., and G. E. Thomas (2006), Modeling the microphysics of mesospheric ice particles: Assessment of current capabilities and basic sensitivities, *Journal of Atmospheric and Solar-Terrestrial Physics*, *68*(7), 715-744.

Rietveld, H. M. (1969), A profile refinement method for nuclear and magnetic structures, *Journal of Applied Crystallography*, *2*, 65-71.

Robert, C. E., C. von Savigny, J. P. Burrows, and G. Baumgarten (2009), Climatology of noctilucent cloud radii and occurrence frequency using SCIAMACHY, *Journal of Atmospheric and Solar-Terrestrial Physics*, *71*(3–4), 408-423.

Rogers, D. C., P. J. DeMott, S. M. Kreidenweis, and Y. Chen (2001), A Continuous-Flow Diffusion Chamber for Airborne Measurements of Ice Nuclei, *Journal of Atmospheric and Oceanic Technology*, *18*(5), 725-741.

Rong, P. P., J. M. Russell, III, M. E. Hervig, and S. M. Bailey (2012), The roles of temperature and water vapor at different stages of the polar mesospheric cloud season, *Journal of Geophysical Research-Atmospheres*, *117*(D04208).

Rong, P. P., J. M. Russell, III, L. L. Gordley, M. E. Hervig, L. Deaver, P. F. Bernath, and K. A. Walker (2010), Validation of v1.022 mesospheric water vapor observed by the Solar Occultation for Ice Experiment instrument on the Aeronomy of Ice in the Mesosphere satellite, *Journal of Geophysical Research-Atmospheres*, *115*, D24314.

Röttger, K., A. Endriss, J. Ihringer, S. Doyle, and W. F. Kuhs (1994), Lattice-Constants and Thermal-Expansion of H_2O and D_2O Ice Ih between 10 and 265 K, *Acta Crystallographica Section B-Structural Science*, *50*, 644-648.

Ruff, S. W. (2004), Spectral evidence for zeolite in the dust on Mars, *Icarus*, *168*(1), 131-143.

Ruiterkamp, R., Z. Peeters, M. H. Moore, R. L. H. on, and P. Ehrenfreund (2005), A quantitative study of proton irradiation and UV photolysis of benzene in interstellar environments, *A&A*, *440*(1), 391-402.

Sack, N. J., and R. A. Baragiola (1993), Sublimation of vapor-deposited water ice below 170 K, and its dependence on growth conditions, *Physical Review B*, *48*(14), 9973-9978.

Safarik, D. J., and C. B. Mullins (2004), The nucleation rate of crystalline ice in amorphous solid water, *The Journal of Chemical Physics*, *121*(12), 6003-6010.

Salam, A., U. Lohmann, B. Crenna, G. Lesins, P. Klages, D. Rogers, R. Irani, A. MacGillivray, and M. Coffin (2006), Ice Nucleation Studies of Mineral Dust Particles with a New Continuous Flow Diffusion Chamber, *Aerosol Science and Technology*, *40*(2), 134-143.

Salzmann, C. G., P. G. Radaelli, B. Slater, and J. L. Finney (2011), The polymorphism of ice: five unresolved questions, *Physical Chemistry Chemical Physics*, *13*(41), 18468-18480.

Sandford, S. A., and L. J. Allamandola (1990), The physical and infrared spectral properties of CO_2 in astrophysical ice analogs, *Astrophysical Journal*, *355*(1), 357-372.

Saunders, R. W., and J. M. C. Plane (2006), A laboratory study of meteor smoke analogues: Composition, optical properties and growth kinetics, *Journal of Atmospheric and Solar-Terrestrial Physics*, *68*(18), 2182-2202.

Saunders, R. W., et al. (2010), An aerosol chamber investigation of the heterogeneous ice nucleating potential of refractory nanoparticles, *Atmospheric Chemistry and Physics*, *10*(3), 1227-1247.

Schneider, N., J. Deighan, A. Stewart, W. McClintock, S. Jain, M. Chaffin, A. Stiepen, M. Crismani, J. Plane, and J. Carrillo-Sánchez (2015), MAVEN IUVS observations of the aftermath of the Comet Siding Spring meteor shower on Mars, *Geophysical Research Letters*, *42*(12), 4755-4761.

Selsis, F., J. F. Kasting, B. Levrard, J. Paillet, I. Ribas, and X. Delfosse (2007), Habitable planets around the star Gliese 581?, *Astronomy & Astrophysics*, *476*(3), 1373-1387.

Simon, A., and K. Peters (1980), Single-crystal refinement of the structure of carbon-dioxide, *Acta Crystallographica Section B-Structural Science*, *36*(Nov), 2750-2751.

Smith, M. D. (2002), The annual cycle of water vapor on Mars as observed by the Thermal Emission Spectrometer, *Journal of Geophysical Research-Planets*, *107*(E11).

Smith, M. D., R. J. Conrath, J. C. Pearl, and P. R. Christensen (2002), Thermal Emission Spectrometer observations of Martian planet-encircling dust storm 2001A, *Icarus*, *157*(1), 259-263.

Smith, P. H., et al. (1997a), Results from the Mars Pathfinder camera, *Science*, *278*(5344), 1758-1765.

Smith, R. S., C. Huang, E. K. L. Wong, and B. D. Kay (1997b), The molecular volcano: Abrupt CCl_4 desorption driven by the crystallization of amorphous solid water, *Physical Review Letters*, *79*(5), 909-912.

Souda, R. (2006), Glass-liquid transition of carbon dioxide and its effect on water segregation, *Journal of Physical Chemistry B*, *110*(36), 17884-17888.

Spiga, A., F. Gonzalez-Galindo, M. A. Lopez-Valverde, and F. Forget (2012), Gravity waves, cold pockets and CO_2 clouds in the Martian mesosphere, *Geophysical Research Letters*, *39*.

Strazzulla, G., G. Leto, G. A. Baratta, and F. Spinella (1991), Ion irradiation experiments relevant to cometary physics, *Journal of Geophysical Research: Planets*, *96*(E2), 17547-17552.

Thomas, G. E. (1991), Mesospheric clouds and the physics of the mesopause region, *Reviews of Geophysics*, *29*(4), 553-575.

Thomas, G. E., and J. Olivero (2001), Noctilucent clouds as possible indicators of global change in the mesosphere, in *Greenhouse Gases, Aerosols and Dust*, edited by D. K. Chakrabarty, H. K. Roscoe and T. A. Blix, pp. 937-946.

Thrower, J. D. (2009), Laboratory investigations of the thermal and non-thermal processing of condensed aromatic hydrocarbons in the interstellar medium, Heriot-Watt University.

Tian, L., G. Heymsfield, L. Li, A. Heymsfield, A. Bansemer, C. Twohy, and R. Srivastava (2010), A Study of Cirrus Ice Particle Size Distribution Using TC4 Observations, *Journal of the Atmospheric Sciences*, *67*(1), 195-216.

Trainer, M. G., O. B. Toon, and M. A. Tolbert (2009), Measurements of Depositional Ice Nucleation on Insoluble Substrates at Low Temperatures: Implications for Earth and Mars, *Journal of Physical Chemistry C*, *113*(6), 2036-2040.

Trainer, M. G., M. A. Tolbert, C. P. McKay, and O. B. Toon (2010), Enhanced CO_2 trapping in water ice via atmospheric deposition with relevance to Mars, *Icarus*, *206*(2), 707-715.

Vincendon, M., C. Pilorget, B. Gondet, S. Murchie, and J.-P. Bibring (2011), New near-IR observations of mesospheric CO_2 and H_2O clouds on Mars, *Journal of Geophysical Research-Planets*, *116*.

von Cossart, G., J. Fiedler, and U. von Zahn (1999), Size distributions of NLC particles as determined from 3-color observations of NLC by ground-based lidar, *Geophysical Research Letters*, *26*(11), 1513-1516.

von Savigny, C., and J. P. Burrows (2007), Latitudinal variation of NLC particle radii derived from northern hemisphere SCIAMACHY/Envisat limb measurements, *Advances in Space Research*, *40*(6), 765-771.

Vondrak, T., J. M. C. Plane, and S. R. Meech (2006), Influence of submonolayer sodium adsorption on the photoemission of the Cu(111)/water ice surface, *Journal of Chemical Physics*, *125*(22).

Vondrak, T., S. R. Meech, and J. M. C. Plane (2009), Photoelectric emission from the alkali metal doped vacuum-ice interface, *J Chem Phys*, *130*(5).

Vondrak, T., J. M. C. Plane, S. Broadley, and D. Janches (2008), A chemical model of meteoric ablation, *Atmos. Chem. Phys.*, *8*(23), 7015-7031.

Wegener, A. (1912), Die Erforschung der obersten Atmosphärenschichten, *Z. Anorg. Chem.*, *75*, 107–131.

Wergin, W. P., J. L. Foster, A. T. C. Chang, D. K. Hall, A. Rango, and E. F. Erbe (1997), Structure of carbon dioxide crystals (Martian snow) as observed in TEM replicas and low temperature SEM images, *Microscopy and microanalysis*, *3*, 1235-1236.

Whalley, C. L., and J. M. C. Plane (2010), Meteoric ion layers in the Martian atmosphere, *Faraday Discussions*, *147*(0), 349-368.

Wilms, H., M. Rapp, and A. Kirsch (2016), Nucleation of mesospheric cloud particles: Sensitivities and limits, *Journal of Geophysical Research: Space Physics*, *121*(3), 2621-2644.

Wood, S. E. (1999), Nucleation and growth of carbon dioxide ice crystals in the Martian atmosphere, Ph.D. thesis, University of California, Los Angeles.

Wordsworth, R., F. Forget, E. Millour, J. W. Head, J. B. Madeleine, and B. Charnay (2013), Global modelling of the early martian climate under a denser CO_2 atmosphere: Water cycle and ice evolution, *Icarus*, *222*(1), 1-19.

Yen, A. S., et al. (2005), An integrated view of the chemistry and mineralogy of martian soils, *Nature*, *436*(7047), 49-54.

Yiğit, E., A. S. Medvedev, and P. Hartogh (2015), Gravity waves and high-altitude CO_2 ice cloud formation in the Martian atmosphere, *Geophysical Research Letters*, *42*(11), 4294-4300.

Yue, J., J. Russell, Y. Jian, L. Rezac, R. Garcia, M. López-Puertas, and M. G. Mlynczak (2015), Increasing carbon dioxide concentration in the upper atmosphere observed by SABER, *Geophysical Research Letters*, *42*(17), 7194-7199.

Yue, J., B. Thurairajah, L. Hoffmann, J. Alexander, A. Chandran, M. J. Taylor, J. M. Russell, III, C. E. Randall, and S. M. Bailey (2014), Concentric gravity waves in polar mesospheric clouds from the Cloud Imaging and Particle Size experiment, *Journal of Geophysical Research: Atmospheres*, *119*(9), 5115-5127.

Zent, A. P., and R. C. Quinn (1995), Simultaneous adsorption of CO_2 and H_2O under Mars-like conditions and application to the evolution of the Martian climate, *Journal of Geophysical Research: Planets*, *100*(E3), 5341-5349.

Zurek, R. W., and L. J. Martin (1993), Interannual variability of planet-encircling dust storms on Mars, *Journal of Geophysical Research: Planets*, *98*(E2), 3247-3259.